ORNL/TM-2022/2813
S07030100-TRT10000

Second Target Station Project: LANSCE WNR Target 2 (Blue Room) Experiment 2022

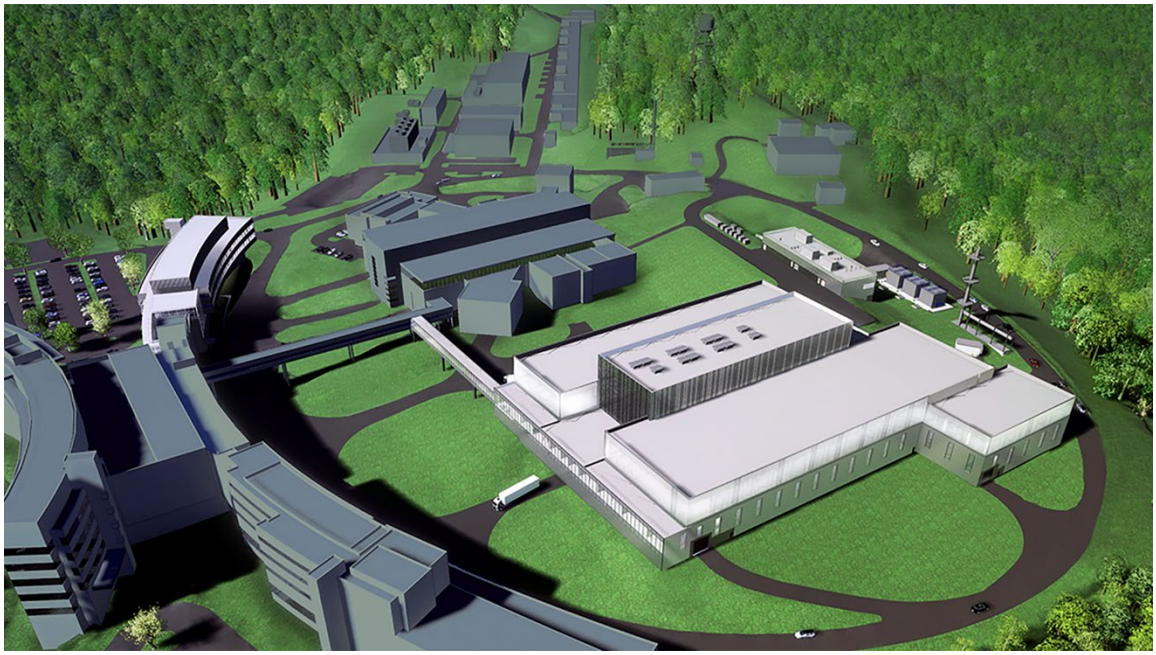

Justin Mach
Joseph B. Tipton Jr.
Willem Blokland
Ken Gawne
Kristel Ghoos
Kranti Gunthoti (LANL)
Kimberly Isbell
Aaron Jacques
Adam Kubik
Doug Kyle
Matt Kyte
Yongjoong Lee
Yun Liu
Cary Long
Thomas McManamy
Sydney Murray III
Thomas Muth
Jessica Osborne
Robert Sangrey
Scott Schwahn
Richard Schwartz
Steve Wender (LANL)
Wouter de Wet
Lukas Zavorka
Alexander Zhukov

July 2023

OAK RIDGE National Laboratory

ORNL IS MANAGED BY UT-BATTELLE LLC FOR THE US DEPARTMENT OF ENERGY

S07030100-TRT10000

Second Target Station Project

LANSCE WNR TARGET 2 (BLUE ROOM) EXPERIMENT 2022

Justin Mach Joseph Tipton Jr.

Willem Blokland
Ken Gawne
Kristel Ghoos
Kranti Gunthoti (LANL)
Kimberly Isbell
Aaron Jacques
Adam Kubik
Doug Kyle
Matt Kyte
Yongjoong Lee
Yun Liu
Cary Long
Thomas McManamy
Sydney Murray III
Thomas Muth
Jessica Osborne
Robert Sangrey
Scott Schwahn
Richard Schwartz
Steve Wender (LANL)
Wouter de Wet
Lukas Zavorka
Alexander Zhukov

July 2023

Prepared by
OAK RIDGE NATIONAL LABORATORY
Oak Ridge, TN 37831
managed by
UT-BATTELLE LLC
for the
US DEPARTMENT OF ENERGY
under contract DE-AC05-00OR22725

Approvals

LANSCE WNR TARGET 2 (BLUE ROOM) EXPERIMENT		ISSUE DATE: July 2023
PREPARED BY Justin Mach	PROJECT Second Target Station	DOCUMENT NUMBER: **S07030100-TRT10000**

	Signature / Date					
	Rev. 00	Date	Rev. 01	Date	Rev. 02	Date
L2 Manager	Peter Rosenblad Digitally signed by Peter Rosenblad Date: 2024.05.16 15:23:19 -04'00'					
L3 Manager	Lyngh, Daniel Digitally signed by Lyngh, Daniel Date: 2024.05.16 15:56:34 -04'00'					
L3 Lead Engineer	Aaron Jacques Digitally signed by Aaron Jacques Date: 2024.05.17 10:55:01 -04'00'					

Revision	Description
00	Initial Release

CONTENTS

ABSTRACT

The Second Target Station (STS) at SNS will address emerging scientific challenges by providing a source of intense, cold neutrons to instruments optimized for this source, using rotating, tungsten target blocks. The STS target will receive 1.3 GeV proton beam pulses from the SNS accelerator at a repetition rate of 15 Hz. The facility life is planned for 40 years, and each target assembly life is expected to be approximately 10 years. An accurate strain prediction is then critical for fatigue life assessment of STS target blocks because they will be subject to approximately 10^8 beam pulses per lifetime.

As an R&D activity, the LANSCE WNR Target 2 (blue room) facility was used to test the strain response of prototypical target blocks to the thermal shock of a proton pulse. The blue room was well suited for a pulsed proton beam impact test of subscale STS target blocks; the 800 MeV proton energy is approximately 60% of the 1.3 GeV proton energy expected from the SNS accelerator to the STS. Both the LANSCE Proton Storage Ring (PSR) and SNS are short-pulse proton beam sources with nominal pulse widths of 250 ns and 661 ns, respectively, so the energy deposition in the target occurs in < 1 microsecond pulse duration.

Strain measurements on the outer surface of 3 target blocks (bare tungsten, tantalum-clad tungsten, niobium-clad tungsten) were recorded for comparison against neutronics and structural simulations. This experiment and the supporting simulations satisfied the following primary research goals for the STS target:

- Validation of analysis predictions of the dynamic strain response in STS test target blocks subject to high-energy pulsed proton beam impacts
    - Result: In general, excellent agreement occurs with data scatter falling within a constant ±10 [με] for peak strains and ±6 [με] for mean strains and strain amplitudes. The error does not appear to be proportional to strain magnitude or beam charge. For the largest beam charge pulses (~ 3 [μC]), the relative error approaches ±10%.
- An assessment of the damping of the strain response between pulse impacts
    - Result: In general, damping was under-predicted on the bare tungsten target block and over-predicted on the clad target blocks. The important factor is that it did not seem to affect the ability to capture the peak strain amplitude and mean strain that control the fatigue life predictions.
- An assessment of the effect of cladding on the dynamic strain response
    - Result: The accuracy of the strain predictions described above was consistent across the bare tungsten, Ta-clad and Nb-clad target blocks, again providing confidence in the simulation predictions, regardless of the design employed.

In summary, the FEA captures the magnitude and frequency content of the strain response, and the error was constant across beam charge. Extrapolating to STS-relevant beam charges, we should see errors in the range of 1%. A 1% increase in strain corresponds to a 1% increase in stress and a <1% reduction in the factor of safety (FOS) for fatigue life predictions in the tungsten.

1. INTRODUCTION

The Spallation Neutron Source (SNS) at Oak Ridge National Laboratory (ORNL) is currently the world's highest-power pulsed neutron source. The First Target Station (FTS) at SNS uses a liquid-mercury target to supply neutrons to nearly 20 state-of-the-art scientific instruments. Complementary to the FTS, the Second Target Station (STS) at SNS will address emerging scientific challenges by providing a source of intense, cold neutrons to instruments optimized for this source, using rotating, tungsten target blocks.

The segmented rotating-wheel concept design is shown in Figure 1, where item #7 indicates where the 21 target block segments reside.

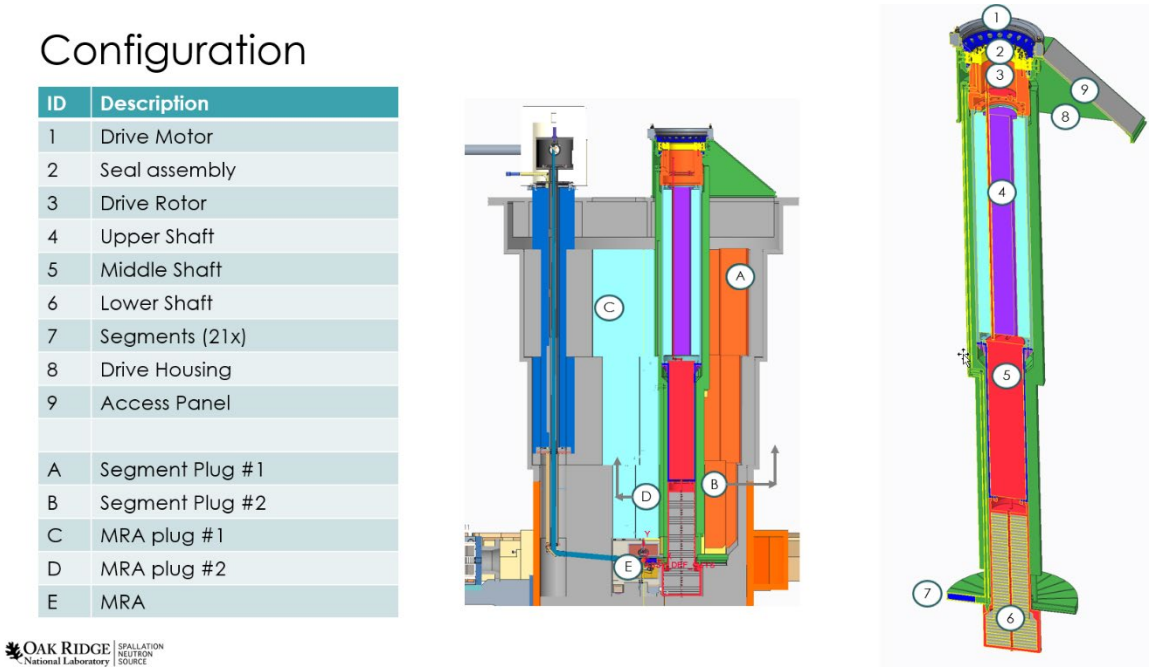

Figure 1. Conceptual design of target assembly showing 21 target block segments (#7).

The original design of a target block within the segment consists of a 1 mm pure tantalum cladding that is bonded (through hot isostatic pressing) to a forged pure tungsten block. The structural integrity of the tantalum (or other candidate cladding material) is critical to the performance and safety of the target system because the target blocks are direct water-cooled. The tungsten must be protected from the cooling water to eliminate low-temperature corrosion and subsequent contamination of the water with activated tungsten.

The STS target will receive 1.3 GeV proton beam pulses from the SNS accelerator at a repetition rate of 15 Hz. The target assembly could operate synchronously or asynchronously with the proton beam, i.e. impact the same location on a block each rotation, or a shifted position with each rotation, respectively. Synchronous operation is easier to analyze while asynchronous operation spreads out energy deposition and radiation damage. Also, the two extremes of impact location must be well understood for either mode of operation: the beam impacts the center of the block face, or between the gap in block segments. Faces of the block contain edges, corners, and cladding welds that may be more susceptible to early-life failures. The STS facility life is

planned for 40 years and each target assembly life is expected to be approximately 10 years. Like the FTS target before it, it is not possible to test the STS target in an operational environment, and R&D is needed to reduce the risk of unplanned replacement.

The complex stress history of a centrally impacted STS target block segment is shown in Figure 2.

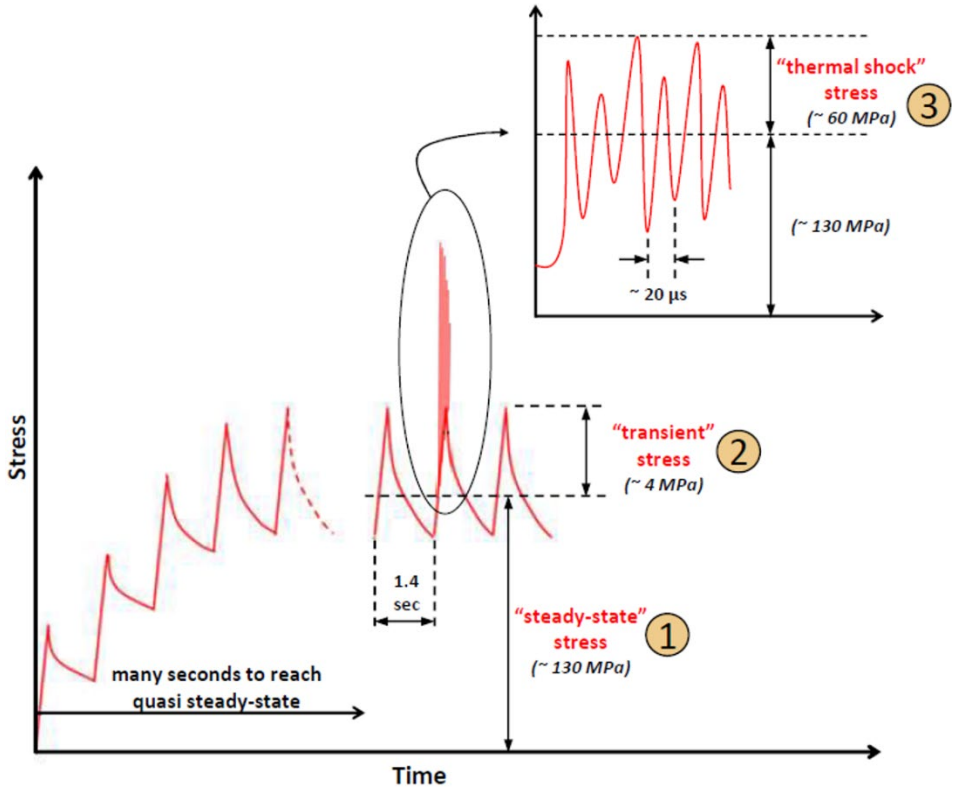

Figure 2. Stress-time history of a centrally impacted target block segment showing: 1. "steady-state" thermal stress after warm-up, 2. "transient" stress from cool-down between beam impacts (1.4 sec.), and 3. "thermal shock" stress due to rapid energy deposition from beam impact (Image adapted from original by Peter Loveridge, High Power Targets Group, ISIS Spallation Source).

The "thermal shock" stress is the dynamic stress due to the rapid energy deposition and subsequent temperature rise in the block, immediately following a beam pulse impact. The stress response of the target block to the thermal shock is the least understood part of the stress history. This is the response that was studied at the LANSCE WNR Target 2 (blue room) facility through strain measurements on the outer surface of the blocks. There is considerable precedent for the fabrication, operation, and analysis of clad tungsten spallation targets [1-6] but premature failures still occur [7]. The STS target block segments are unique compared to these targets with respect to their larger dimensions/mass (~36 kg), larger clad surface area and weld length, motion relative to the beam, and more complex geometry—other targets are mostly cylindrically shaped. The experiment at the blue room provides validation of the predicted strain response due to proton beam impact. An accurate strain prediction is critical for fatigue life assessment of STS target blocks because they will be subject to approximately 10^8 beam pulses per lifetime.

The strain measurement system used is a novel, high-radiation-tolerant fiber-optic sensor system developed at SNS that is used to measure dynamic strains in the FTS mercury target [8-11]. The sensors have demonstrated high dynamic range (45 dB) and megahertz measurement bandwidth—critically important for measuring the thermal shock strain response of a spallation target, as depicted in Figure 2. Fiber Bragg Grating (FBG) sensors have been used at accelerators [12, 13], but there is no existing FBG processor that can achieve the high bandwidth needed for the strain signals. A higher bandwidth alternative is the laser doppler vibrometer (LDV) [13-15], however it only measures the normal/radial vibration at a single point (per LDV device). The SNS system can measure the high-bandwidth, in-plane (surface) strains at any number (limited to available hardware) of locations and directions needed to validate and improve the analysis predictions.

This experiment and supporting simulations support the following primary research goals for the STS target:

1. Validation of analysis predictions of the dynamic strain response in STS test target blocks subject to high-energy pulsed proton beam impacts
2. An assessment of the damping of the strain response between pulse impacts
3. An assessment of the effect of cladding on the dynamic strain response

2. MATERIALS AND MANUFACTURING

The nominal geometry for the conceptual STS target block design is included in the TARGET drawing attached to this document. The length/depth dimension relative to the beam travel direction is approximately 250 mm from the beam impact location to the opposite face of the target block. Drawing 106010402-M8U-8700-A002 (attached) shows the nominal geometry of a forged and machined, 48 mm thick tungsten development block, which has a similar length as the target block. The development block was machined from an open die forged tungsten disc made by Plansee. Three experiment target blocks, 220 mm in length, were machined from this development block, as shown in the photograph in Figure 3.

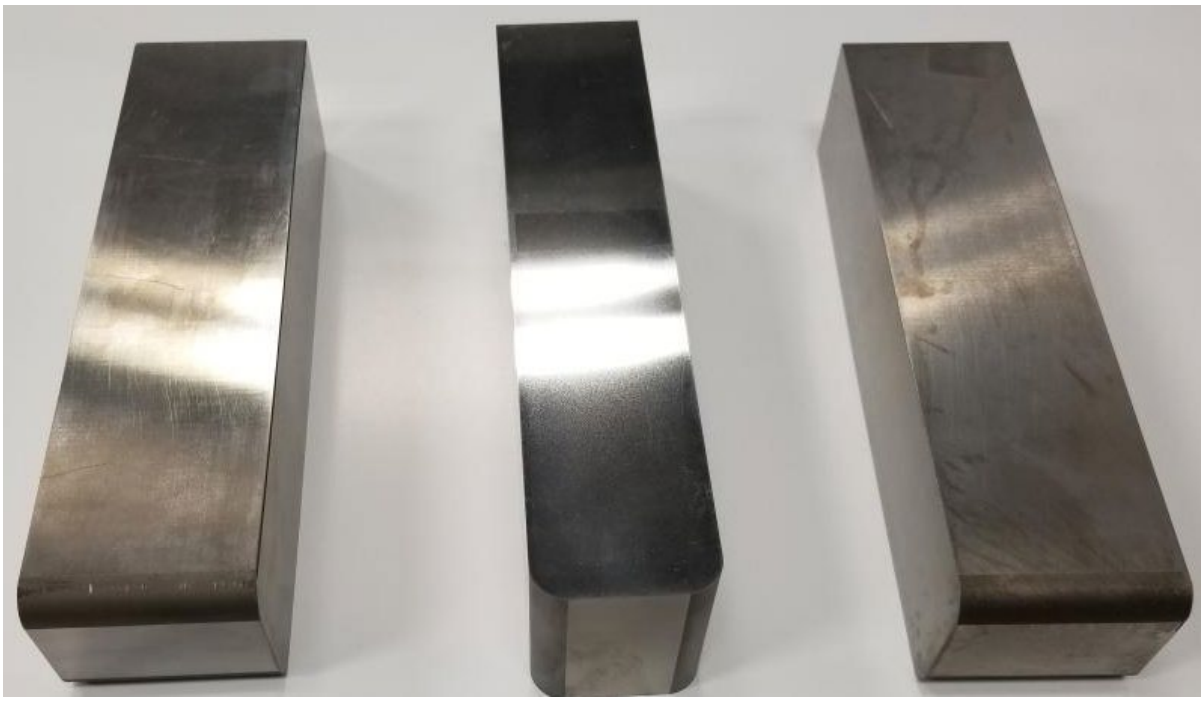

Figure 3. Bare tungsten target blocks

Two target blocks were clad using a hot isostatic press (HIP): one in pure tantalum and one in pure niobium. The material certification including the chemistry and mechanical properties for the tantalum sheet is attached as "Tantalum.pdf". Due to the long lead time for procurement of 1 mm thick niobium sheet, it was decided to roll a plate of 0.5 inch thick commercially pure niobium plate to 0.04±0.002 inches, using rolling mills available at ORNL in the building 4508 high bay. The process outline is described in the attached document "Rolling Niobium for STS.pdf", and an interim process image showing the rolled 1 mm thick niobium sheet (prior to straightening) is shown in Figure 4.

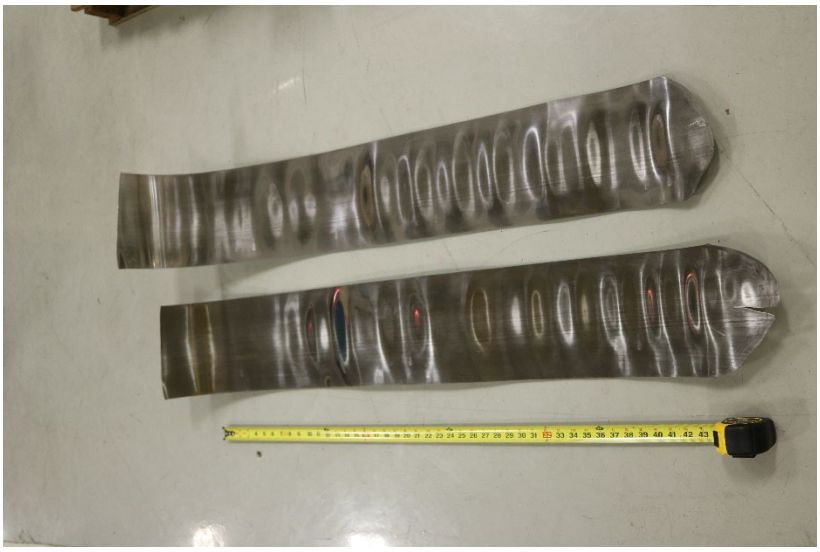

Figure 4. The 1 mm thick rolled niobium sheet prior to straightening.

The manufacturing drawings are attached as S07030100-M8U-8800-A10003 and S07030100-M8U-8800-A10004. The piece parts are shown in Figure 5, where the 1 mm thick tantalum cladding is on the left and the 1 mm thick niobium cladding is on the right.

Figure 5. Piece parts for manufacturing the Ta-clad (left) and Nb-clad (right) experiment target blocks.

The nose pieces of the target blocks were formed using a marforming process, and the tooling is described in detail in the attached drawing TRMTRDRGASP-1281. The process is depicted for the tantalum nose piece in three images shown in Figure 6.

Figure 6. The marforming process of the tantalum nose piece as shown in three stages: beginning (left), middle of machine stroke (middle) and end of machine stroke (right).

The marforming process produced a good fit of the tantalum nose piece to the tungsten block and to the adjoining piece parts, as shown in the images in Figure 7.

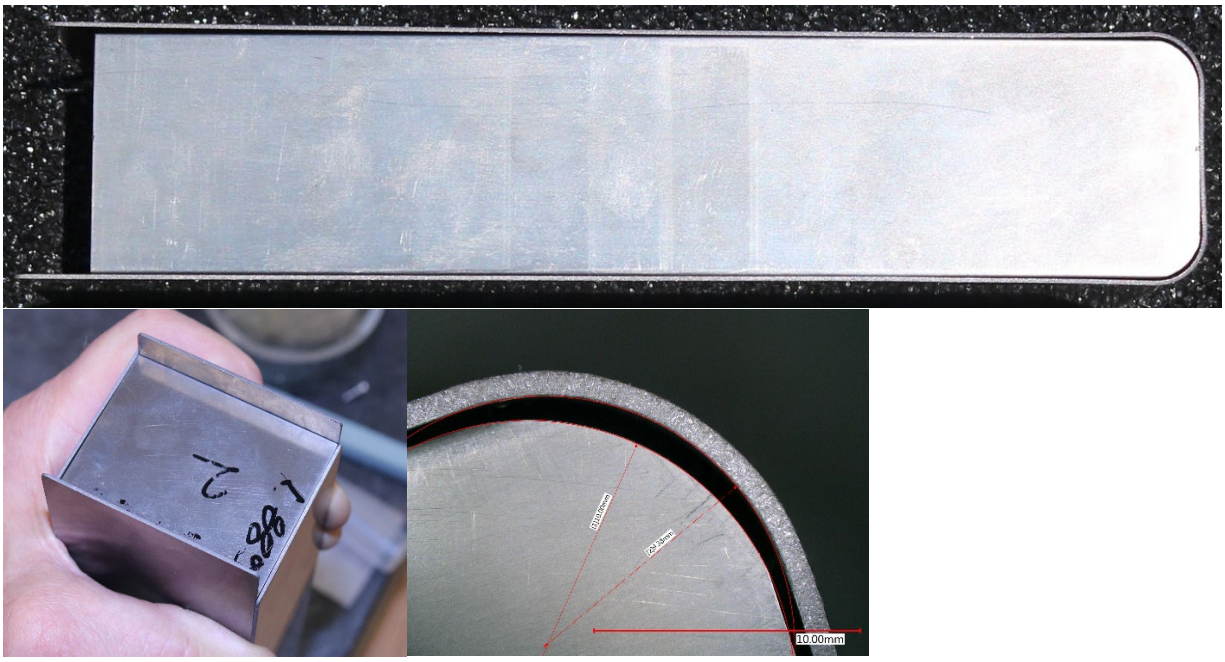

Figure 7. Images showing the fit up achieved between the tantalum nose piece and the tungsten block and side piece parts.

The niobium nose piece was processed the same as the tantalum nose piece and good fit up was achieved for this target block as well. Prior to welding, all cladding piece parts were scrubbed with a 65 µm diamond and alcohol slurry. The tungsten was ground to 120 grit (140 µm diamond) followed by the 65 µm diamond and alcohol slurry scrubbing (using a leather pad). The tungsten grinding ensured the removal of any wire electrical discharge machining (EDM) case layer, and the diamond scrub ensured the removal of any remaining oxide layer from all piece parts.

The following describes the welding process, which consists of two steps using gas tungsten arc welding (GTAW) to create the cladding enclosure followed by electron beam (EB) welding to seal the enclosure under vacuum.

GTAW

The welding glovebox was evacuated to less than 10 mTorr and backfilled with ultra-high purity argon for welding. A color check of a weld bead performed on a titanium block inside the glovebox is used to confirm glovebox atmospheric purity below 10 µmol / mol oxygem (10 ppm). The Ta / Nb sheets were tack welded at approximately every 2 inches to prevent distortion during seam welding. The travel speed and technique vary depending on the location on the part. The size of the welding puddle is monitored, and the speed is adjusted depending on the length of the weld, which will dictate the temperature rise in the block ahead of the weld. Typically, the welds are no more than about 2 inches long and completed in a skip and backstep pattern, alternating between different seams on the block to spread out the heat. The start of a weld is slower with higher welding current to produce the proper size weld pool, then as the base metal

temperature increases, the travel speed increases, and the current is decreased via the variable foot pedal. A long taper or downslope is used at the end of each weld. Welds overlap at each backstepped weld and at the corners to ensure good tie-ins everywhere (as the weldment must be leak-tight for EB-weld closure). The small radius on the tungsten edges required more welding current than previously welded blocks with larger tungsten radii. The following parameters were used on a Miller Dynasty 350 welder:

- Current/polarity: DCEN pulsed
    - Peak current – 150-170 amps
    - Background current – 33% peak
    - Peak time – 33%
    - Pulses per second – 3.3
- Voltage: 11-13 volts average
- Travel speed: 1-2 inches per minute
- Tungsten electrode type/size: 1/8-inch EWLa-2
- Welding chamber gas: UHP argon
- Torch gas: N/A – chamber gas only
- Single pass welding

<u>EB</u>

The electron beam circles the hole several times (1-2 times for niobium, 3-4 times for tantalum) and the metal starts to melt. Once the hole is filled, a downslope is started, and the beam is moved away from the hole. The following parameters were used on a PRT 150kV, 100 mA, SN:643 machine:

- Voltage: 125 kV
- 24 filament amp
- 4 mA beam current
- Lens current 661 mA (sharp focus +15 mA)
- 1 second upslope, 1 second downslope
- 2 Hz, circle pattern (5), X-deflection 3.5, Y-deflection 3.5 – the circle is slight larger than the 0.5 mm hole
- 1.33E-05 millibar chamber vacuum level at start of welding

Between GTAW and EB welding, the blocks were leak tested to ensure a vacuum tight enclosure seal, as shown in Figure 8.

Figure 8. Leak testing was performed between GTAW and EB welding to ensure a vacuum tight enclosure before HIP-ing.

Prior to sending the clad target blocks out for HIP, they were cleaned and packaged with the following process (as adapted from the space power program for cleaning iridium):

- 10 minutes ultrasonic cleaning at 70 °C in 1L DI water + approximately 6 mL of Microcleen detergent
- Rinse with running DI water for approximately 2 minutes to remove all detergent
- 15 minutes ultrasonic cleaning at 70 C in 2L DI water (clean Pyrex jar)
- Air dry
- Package with white cotton gloves

The Ta-clad and Nb-clad target blocks were HIP-ed by Bodycote in St. Andover, Massachusetts. The HIP specifications provided to Bodycote are attached as S03020200-TSP10000 and S03020100-TS0002 for niobium and tantalum, respectively. The nominal HIP parameters for the Ta/W were 1200°C ±10°C for 180 ±30 minutes at 150 MPa minimum pressure, and the parameters for the Nb/W were the same except the temperature was 1150°C ±10°C. One modification to the process specifications is that molybdenum sheet was used as an outer "retort" vessel in which the zirconium foil wrapped parts were placed, and it was not used as an interlayer between the foil and parts. The supplier said that this was not necessary to prevent the foil from bonding to the cladding and it was found that although the foil "stuck" to the cladding in some places, it was easily removed as they said it would be. Furthermore, the molybdenum outer vessel was necessary to separate the Zr foil from the tooling platform inside the HIP furnace and provided a secondary oxygen getter material inside the HIP furnace, which is the primary role of the zirconium foil (see Figure 9).

Figure 9. The tantalum and niobium clad target blocks post-HIP and still wrapped in the zirconium (oxygen-getter) foil.

After unwrapping the target blocks from the Zr foil, the target blocks appeared to have minimal discoloration from the HIP process (as shown in Figure 10 and Figure 11), which indicated that a sufficiently inert gas environment was maintained throughout the HIP cycle.

Figure 10. The Ta-clad tungsten target block after the HIP process.

Figure 11. The Nb-clad tungsten target block after the HIP process.

After the visual inspection, the clad target blocks were sent for ultrasonic testing (UT) inspection. No interface gaps were detected, and the surfaces all appeared uniform with a tight mechanical and/or diffusion bond. Complementary UT work on a similar tantalum-clad tungsten sample revealed that an interface gap less than ~1/2 the wavelength of the transducer input frequency is not detectable via UT inspection. For a standard 22.7 MHz transducer this amounts to a gap < 74 μm. The UT reports are attached in the archived file "LANSCE blocks Aug

2022.7z". Following the inspection, all three blocks were packaged in individual crates and shipped to LANSCE for strain sensor installation prior to the experiment beamtime start.

3. EXPERIMENT METHOD

3.1 OVERVIEW

The blue room is well suited for a pulsed proton beam impact test of subscale STS target blocks; it has previously hosted SNS experiments for mercury-filled [16-18] and solid targets. The 800 MeV proton energy is approximately 60% of the 1.3 GeV proton energy expected from the SNS accelerator to the STS. This requires the use of a long test target block to stop most of the protons in the sample. Both the LANSCE Proton Storage Ring (PSR) and SNS are short-pulse proton beam sources with nominal pulse widths of 250 ns and 661 ns, respectively, so the energy deposition in the target occurs in < 1 microsecond pulse duration. Using typical beam characteristics coming from the PSR (3×10^{13} protons per pulse, Gaussian, $\sigma = 10$ mm), the peak intensity is calculated to be approximately 4.8×10^{10} protons / mm^2, which is roughly 1.5 times the peak intensity of the proposed STS beam. However, the STS beam impact footprint is much larger at ~ 188 mm wide x 48 mm tall (95% of the estimated 2.24×10^{14} protons per pulse). The energy per pulse (47 kJ) is approximately 12 times greater than the PSR pulse. Therefore, the test blocks have been scaled down relative to the STS production target blocks. Without exceeding the time-averaged 80 nA limit in the blue room, it is possible to receive a beam pulse from the PSR approximately every one minute. Repeat and varying parameter measurements can be performed in the same day with adequate contingency for accelerator, measurement equipment, or other unforeseen problems.

The STS experiment team utilized the blue room Bergoz coil as a backup for beam current monitoring, with the primary measurement coming from a Pearson Current Monitor Model 8586. The beam position and intensity monitoring system used a Chromox / AF995R Fluorescent Screen, mirrors, and cameras with zoom lenses. The beam charge, position, and intensity data were recorded with each beam pulse test as part of the overall data acquisition strategy. The target strain measurement system is a modular portion of the SNS FTS system that allows for up to 15 strain sensors to be used for the experiment. The single-mode fiber optic sensors are purchased from Luna and installed by ORNL technicians, the optical cable connections fabricated at ORNL, and the custom-made optical processors are assembled at ORNL. The corresponding data acquisition units and electronic chassis (power/modulation signals) were brought as part of two measurement system electronic racks: one for strain measurement and one for the beam current, position, and intensity measurements. The strain sensors and data acquisition system have sufficient range, resolution, and sensitivity (with low noise) to measure very high frequency strain signals as low as a few microstrain in magnitude. Details of the strain sensors and data collection system are shown in Table 1.

Table 1. Strain sensor and data collection details.

Type	Noise	Sensitivity	Resolution	Linear	Drift	Range	Repeatability	Sampling rate
single-mode fiber, low-coherence interferometry	< 1 micro-strain @ 1 MHz, Order (mV) for 0-1 volt range	1 micro-strain@1 MHz	0.1 micro-strain, 100 ns (time)	Yes	No drift within measurement time	±1500 micro-strain	< 2%	10^7 samples/sec

LabVIEW programs like those used at the SNS accelerator and FTS were used for data acquisition of beam parameters and strain data for each beam pulse test. The planned test conditions included:

- Samples:
  - Unclad tungsten block
  - Tantalum-clad tungsten block
  - Niobium-clad tungsten block
- Beam conditions:
  - Beam position: centered on target block impact face
  - Beam charge: full/half/quarter intensity pulses to check linearity of signals and increase confidence in data at full intensity
  - Beam impact footprint: nominal, Gaussian, σ = 10 mm or smaller

A detailed pulse-by-pulse test plan with the actual beam charges received is attached as "MASTER_LOG.pdf". The LANSCE accelerator was unable to deliver requested beam charges; the beam charge varied significantly from shot to shot while they tuned the beam to produce increasingly higher charges. The nominal beam positions, centered on each of the blocks' front faces, are labeled 1, 2, 3 in Figure 12.

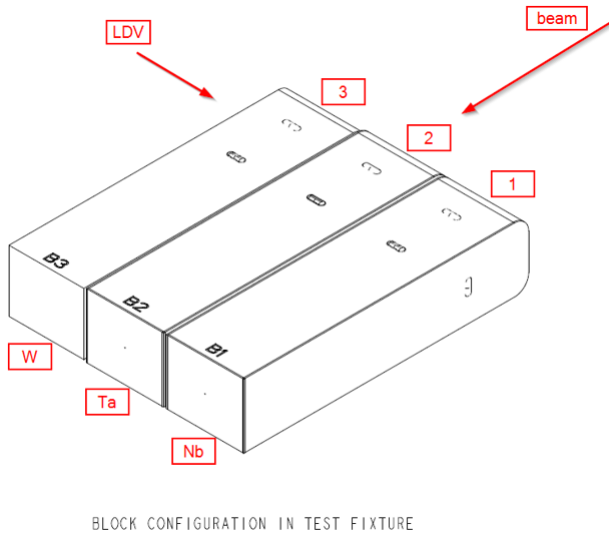

Figure 12. Beam positions 1,2,3 align with the center of the front face of each of the three target blocks B1, B2, B3.

The LDV was aimed through a series of two mirrors at the exposed side surface on the pure tungsten block B3, orthogonal to the beam direction. This data requires further analysis and will be discussed in a future revision of this report.

The original project plan is captured in the appendix of the experiment proposal submitted to LANSCE, which is attached as "9109_LANSCE_STS_proposal_2022.pdf". Detailed planning of the experiment schedule is included in "gantt_chart.pdf". A photographic summary of the experiment is attached in the document "2022-09-16_Group_Meeting_R&D_Update.pdf" and additional photos can be located via the appendix regarding documentation and data locations.

3.2 FIXTURE, MOTION, SURVEY & ALIGNMENT

The complete drawing package for the fixture is included in the attached archived file "fixture_drawing_pkg.7z". The full drawing package includes additional shield blocks that were not needed, but some of them were manufactured due to the lead time and original scheduling of the experiment (December 2021). The December 2021 experiment was scheduled with a maintenance outage preceding the experiment but not after the experiment. Therefore, it was predicted that additional shielding would be required after the experiment to expedite the experiment takedown and the setup of the blue room for Target 4 neutron production (where the beam passes through the blue room on its way to Target 4). The rescheduling of the experiment to 2022 provided an opportunity to request a maintenance outage after the experiment, so that the experiment setup could cool down for 24-48 hours before takedown. The fixture shield blocks were not necessary in this scenario and the final configuration of the fixture is shown in the left image of Figure 13. The right image in Figure 13 shows the blocks in the fixture from the perspective of the beam direction with the beam fluorescing on the pink image plate, where the beam is focused on the center of the tantalum-clad tungsten target block, B2.

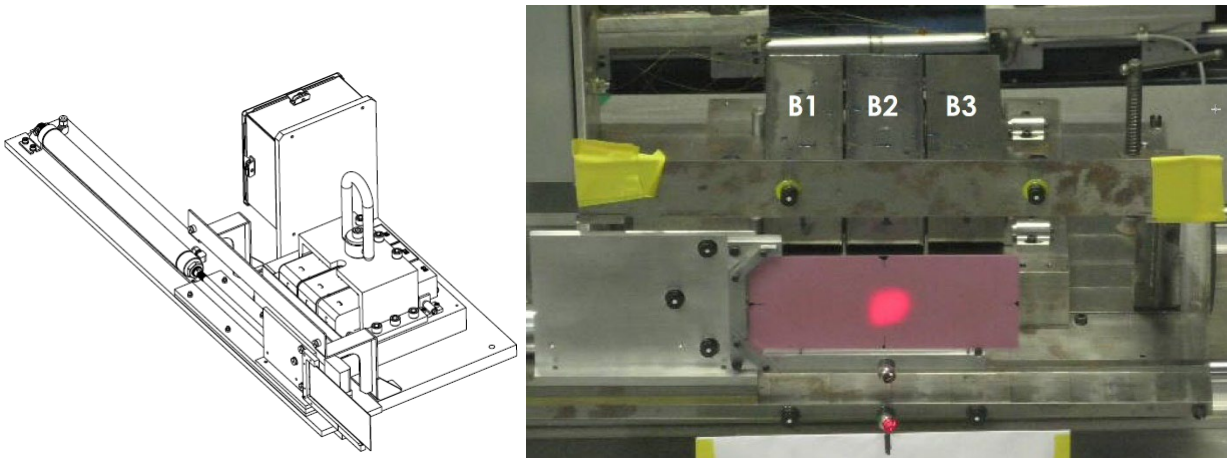

Figure 13. Final fixture configuration (left) and a view in the direction of the beam of the target blocks in the fixture with the beam fluorescing on the pink image plate (right).

Key features of the fixture include:

- A base plate that was clamped to a horizontal stage (attached in drawing "BR_stage.pdf). The horizontal stage was provided by LANSCE with remotely controlled horizontal motion to move the blocks to programmed positions where the expected beam center was

centered on each block. This was tracked and verified through a laser tracker and corresponding software from the survey and alignment team.

- A remotely controlled air cylinder to retract the image plate so that it is centered on the blocks and to extend the image plate so that it is not in front of the blocks (for beam tuning without irradiating the blocks). A picture of the air controller is shown in Figure 14.
- Surfaces aligned with the beam-facing surface of the image plate where fiducials were placed to measure the position of the beam relative to the fixture and blocks.
- A lifting bracket, hook, and block constraints for safely transporting the assembled fixture with blocks (total ~300 lbs.) from a cart onto the horizontal motion stage, which was mounted on an experiment table that has manual vertical adjustments at its four corners.
- An electrical box mounted on the side of the fixture and out of the beam path for collecting the fragile sensor cables and attaching them to the well-protected fiber bundle that was routed to the DAQ (data acquisition) cabinets in the control room.

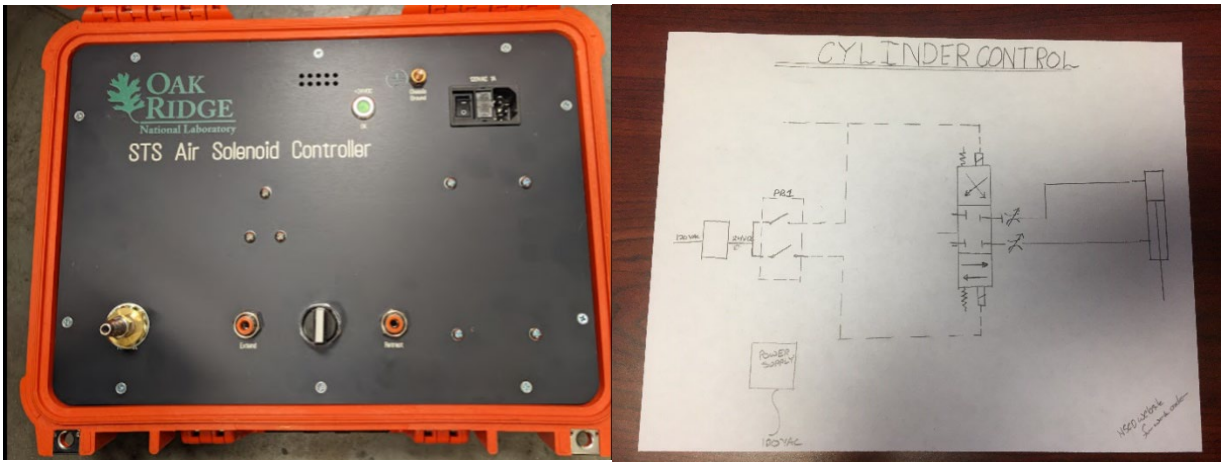

Figure 14. The air controller allowed for remote control of the air cylinder that extended and retracted the image plate beyond and in front of the blocks, respectively.

Key points associated with the survey & alignment include:

Individual tungsten blocks were measured at the ORNL SNS metrology lab using a Faro PCMM to ensure the final dimensions met the design intent geometry. The ideal sensor locations were marked on each block during the measurement process, center point and a second point defining the sensor direction, as shown in Figure 15.

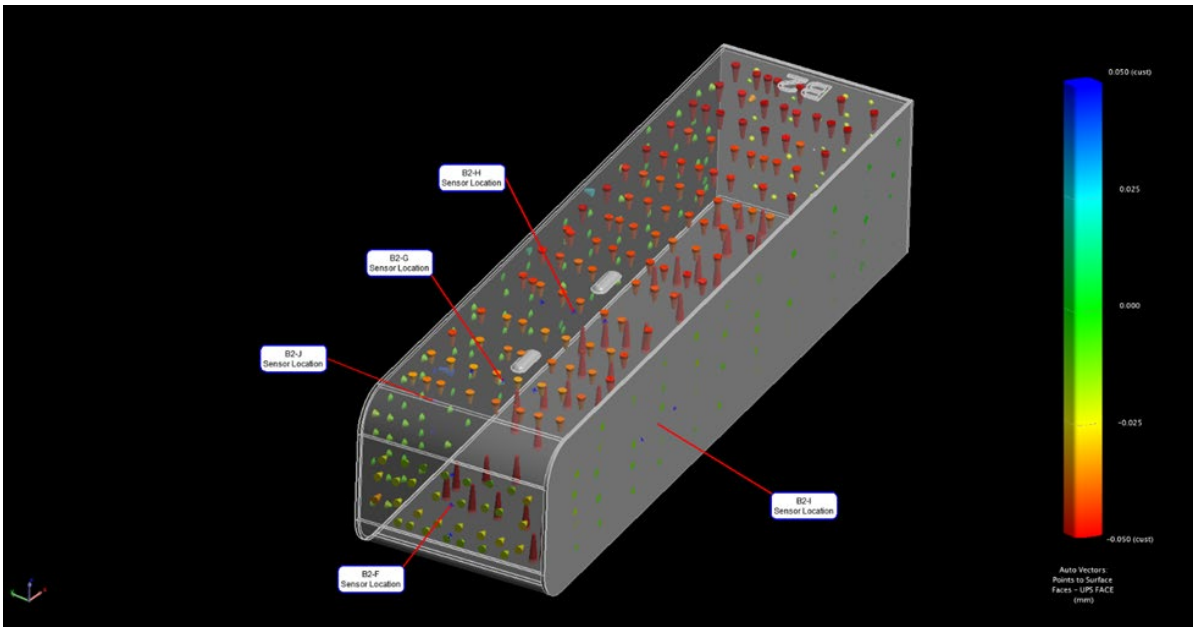

Figure 15. Inspection and sensor layout data for the tungsten blocks.

The original intent was to map each block as installed on the fixture to determine the center of each block relative to the fixture. The blocks are separated by 2.0 mm pins. The cladding process resulted in edges that were not square and the gaps between the blocks were not accessible with an edge nest. The final position of each block was determined by measuring the upstream planes, top planes, the beam left plane of Block B1, and beam right plane of Block B3.

The accessible planes of the tungsten blocks were measured as installed on the test fixture using a Leica AT401 laser tracker to determine the position and orientation of the blocks. Magnetic fiducial nests were epoxied on the test fixture and mapped relative to the blocks for locating the fixture assembly in the Blue Room network.

Additional fiducial nests were also epoxied on the fixture in the field of view of the camera system. After the fixture was installed and aligned the position of the nests were measured relative to the center of each block. The 0.5” reflectors used with the laser tracker were replaced with 0.5” reflective spherical targets visible to the camera system installed in the Blue Room.

The actual beam position relative to the sample positioning table in the room was initially unknown. Flanges on the upstream and downstream beam vacuum pipes were measured and a line was constructed between the two centers points as an approximation of the beam position. The test fixture was installed such that the center of each target block could be placed on the beam centerline and aligned such that the lateral translation was perpendicular to the beam. Position calibration and verification of the sample positioning table was also conducted using the laser tracker. The positions were recorded in the motion software (ref. Figure 16) and repeatability was confirmed.

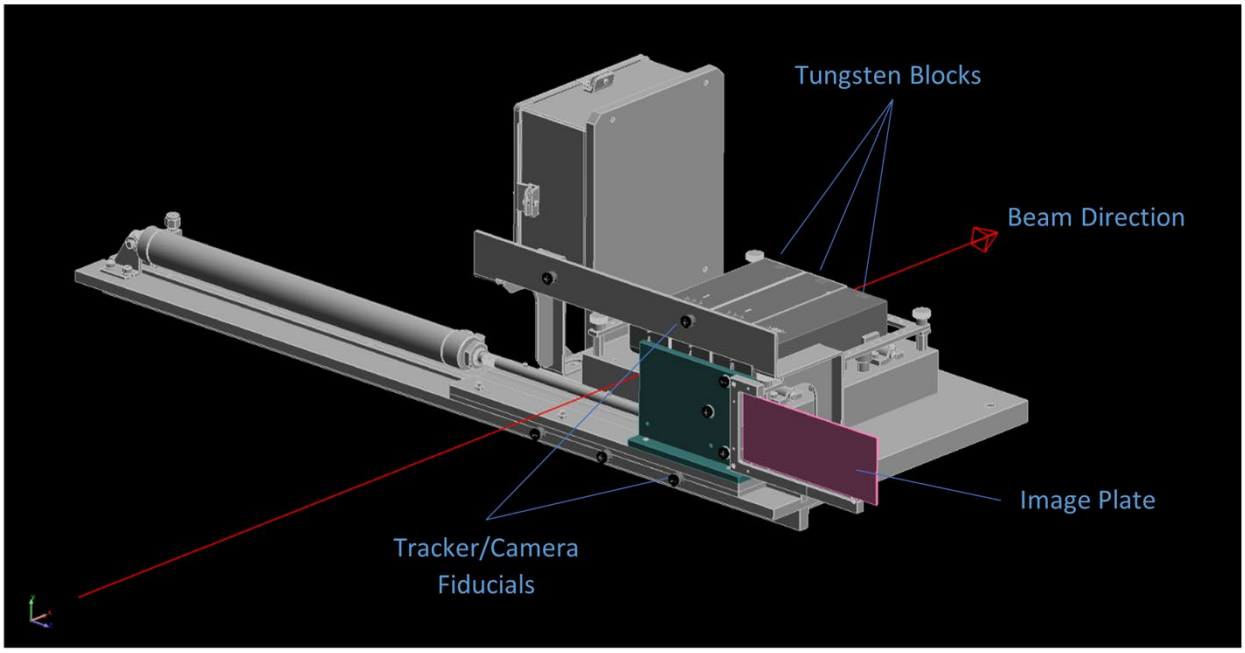

Figure 16. Fiducial monuments were attached to the test fixture and mapped using a laser tracker to accurately position each block in the path of the beam.

The fixture position was adjusted vertically after initial beam was delivered to the image plate and it was determined that the beam could not be steered into the center of the target blocks. Precise vertical adjustments were made to the translation stage using the laser tracker based on the room network measured during the initial installation and alignment.

3.3 STRAIN MEASUREMENT

3.3.1 Background & Measurement Method

Fiber-optic sensors are considered the most suitable sensor candidate for strain measurement in the spallation target because of their compact size and immunity to electromagnetic interference. At SNS, we have developed a high radiation tolerance, high measurement bandwidth fiber-optic sensor system. The sensor head consists of a low-finesse Fabry-Perot interferometer (FPI) formed by cleaved end surfaces of two pieces of fibers assembled inside a glass capillary tube. Figure 17 shows a schematic and a microscope image of the sensor head. The glass tube has an outer diameter of 209 µm and an inner diameter of 127 µm. The fluorine-doped single-mode fiber (Fujikura RRSMFB) is used as the lead-in fiber while the reflecting fiber is coated with a thin film of gold where a typical power reflectivity is 5–10%. The designed gap between the two fiber end surfaces is approximately d = 65 µm and the sensor length is around L = 4 mm.

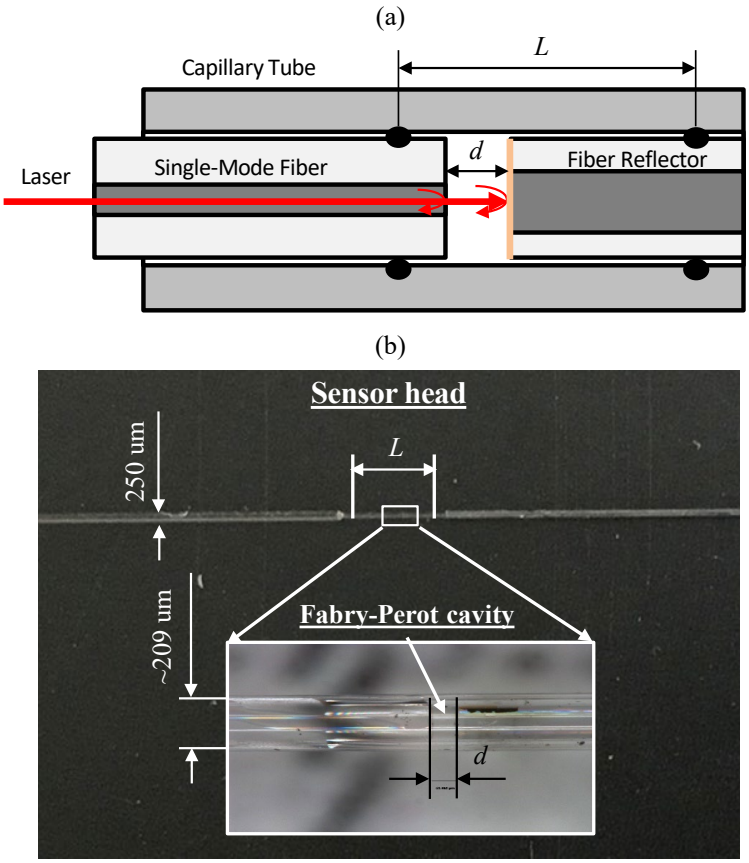

Figure 17. (a) Schematic and (b) microscope image of a Fiber-optic strain sensor made from a Fabry-Perot interferometer. L: sensor length, d: gap of the Fabray-Perot interferometer.

The signal interrogation scheme was based on the low-coherence interferometry technique, which has a high tolerance for light intensity fluctuations. Figure 18 shows an all-fiber-based Faraday Michelson interferometer developed at SNS for demodulation of the strain waveform from the sensor.

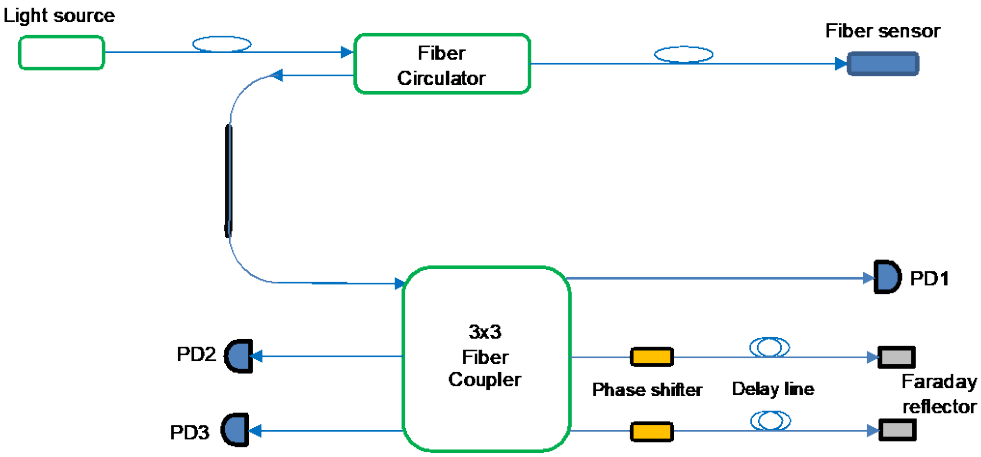

Figure 18. Schematic of signal demodulator used in the strain measurement. The light source is a supercontinuum laser diode with a center wavelength of 1.32 μm and coherence length of ~ 30 μm.

When a low-coherence light source is used, the normalized outputs from 3 photo-detectors (PDs) can be expressed by

$$P_1 = A_1 I_0, \tag{1}$$

$$P_2(x) = A_2 P_1[1 + k\cos(4\pi x/L + 2\pi/3)], \tag{2}$$

$$P_3(x) = A_3 P_1[1 + k\cos(4\pi x/L - 2\pi/3)]. \tag{3}$$

Here I_0 and λ are the intensity and center wavelength of the light source, respectively, $A_1 - A_3$ are constants determined by laser power and light transmission coefficients in fiber components, k represents the visibility of the interference signal and is also a constant for a pair of sensing and demodulation interferometers, and $x = \Delta d$, denotes the gap variation in the sensor head. The first detector output is proportional to the optical power reflected from the sensor, while the second and third detectors provide phase-shifted interference signals which explicitly contain the information of the sensor gap. As the values of A_2, A_3 and k can be obtained from the calibration process, Equations (2) and (3) can be simplified to

$$f_2(x) = \cos(4\pi x/L + 2\pi/3), \tag{4}$$

$$f_3(x) = \cos(4\pi x/L - 2\pi/3). \tag{5}$$

From Equations (4) and (5) one can obtain a continuous phase recovery, i.e., obtain the value of $x(t)$, without ambiguity over a large measurement range. It is also noted that the variation of laser intensity due to the light source or measurement environment can be compensated by using the PD1 output in the current demodulation scheme. This is particularly important for the strain measurement in the spallation target as the proton pulse will induce a sharp attenuation of the light transmission in the optical fiber.

The strain is calculated from the variation of sensor gap as

$$\varepsilon(t) = \frac{x(t)}{L}. \tag{6}$$

Details of the signal demodulation and data processing can be found in references [11, 19, 20]. With the support from the STS project, we have assembled an additional 16 all-fiber based signal demodulation modules, which makes it possible to simultaneously measure strain waveforms at up to 16 different locations from the target blocks. Fig. 3 shows a photo of the equipment rack that houses 16 modules. All modules were tuned and tested before shipping to LANSCE for the experiment.

Figure 19. Photo of the equipment rack containing 16 all-fiber based signal demodulation modules for the strain sensors.

Strain measurement on a tungsten plate has been conducted to verify both the signal demodulation modules and sensor attachment to the tungsten material. The 0.6-mm thick tungsten plate has dimensions of 62 mm (L) x 40 mm (W). A fiber sensor is attached on the sensor surface using a stycast epoxy. For static strain generation, the tungsten plate is clamped at one end to form a cantilever structure while its other end was pressed to bend the plate. The

fiber sensor is located at 26 mm away from the free end. During the measurement, the far end of the test plate is pressed up to 2.5 mm at a step size of 0.5 mm. At each step, the induced strain is measured by the sensor while a theoretical prediction of the strain at the sensor location is calculated based on the displacement at the far end of the test plate using a standard formula for a cantilever beam. Both the measurement and calculation results are shown in Figure 20. An excellent agreement between the measurement and theoretical results has been obtained.

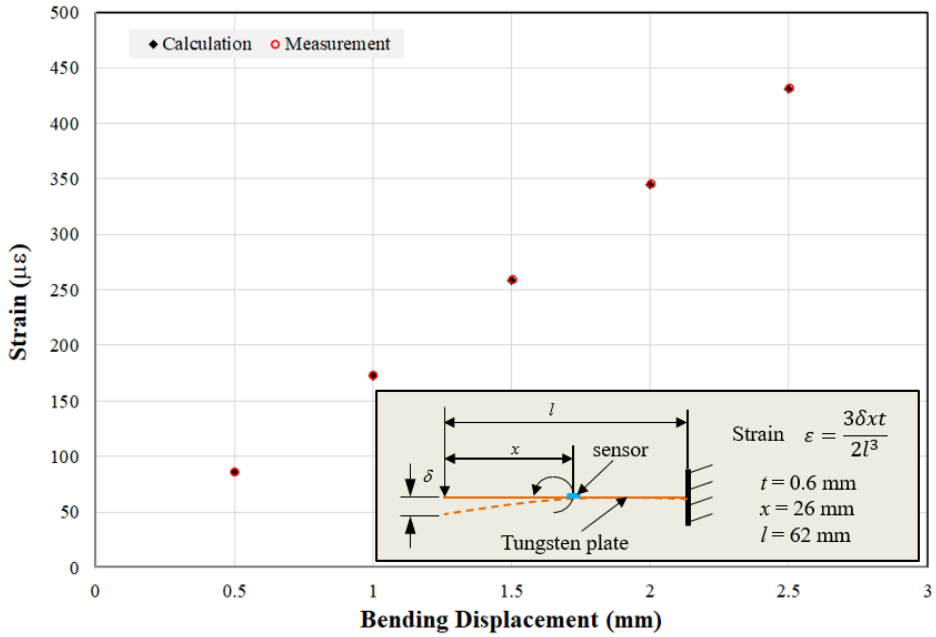

Figure 20. Static strain measurement results on a tungsten test plate. Inset box: diagram of the test plate mounted in a cantilever configuration.

3.3.2 Signal Processing

During the strain measurement at LANSCE, the outputs from all 15 fiber-optic strain sensors are simultaneously processed by our integrated demodulator system. Each measurement event is prompted by a trigger pulse which is about 7 ms prior to the arrival of the proton pulse. The analog outputs from three photo-detectors (PDs) of each demodulation module are digitized using a 14-bit National Instrument (NI) data acquisition (DAQ) module (Model PXIe-5170R) at a sampling rate of 10 MHz. The DAQ continues for a certain time (30 ms in the current case) and a self-calibration process follows each measurement. During the self-calibration process, one of the phase shifters in the demodulation module (Figure 18) is scanned over a range larger than 2π at a frequency of 100 kHz. The self-calibration at the end of each measurement event enables an in-situ verification of the values of coefficients A2, A3 and k in Equations (2) and (3). The PD outputs are then renormalized using those coefficients and the phase demodulation is conducted from the normalized signals, i.e., Equations (4) and (5).

Figure 21 shows a typical example of the measured data. Figure 21(a) shows the normalized outputs from PD2 and PD3. The waveforms after 23 ms correspond to the self-calibration process. Figure 21(b) is the strain signal calculated from PD2&3 outputs. Again, the waveform after 23 ms is the modulation signal applied to the phase shifter. The cut-off at the bottom was likely caused by the saturation in the driving circuit of the phase shifter. The PD1 output is

plotted in Figure 21(c). We observe a sharp reduction at the beginning of the waveform. This is caused by the radiation-induced absorption (RIA) in the optical fiber when the proton pulse strikes the target. The RIA normally recovers within about 1 ms after the proton pulse.

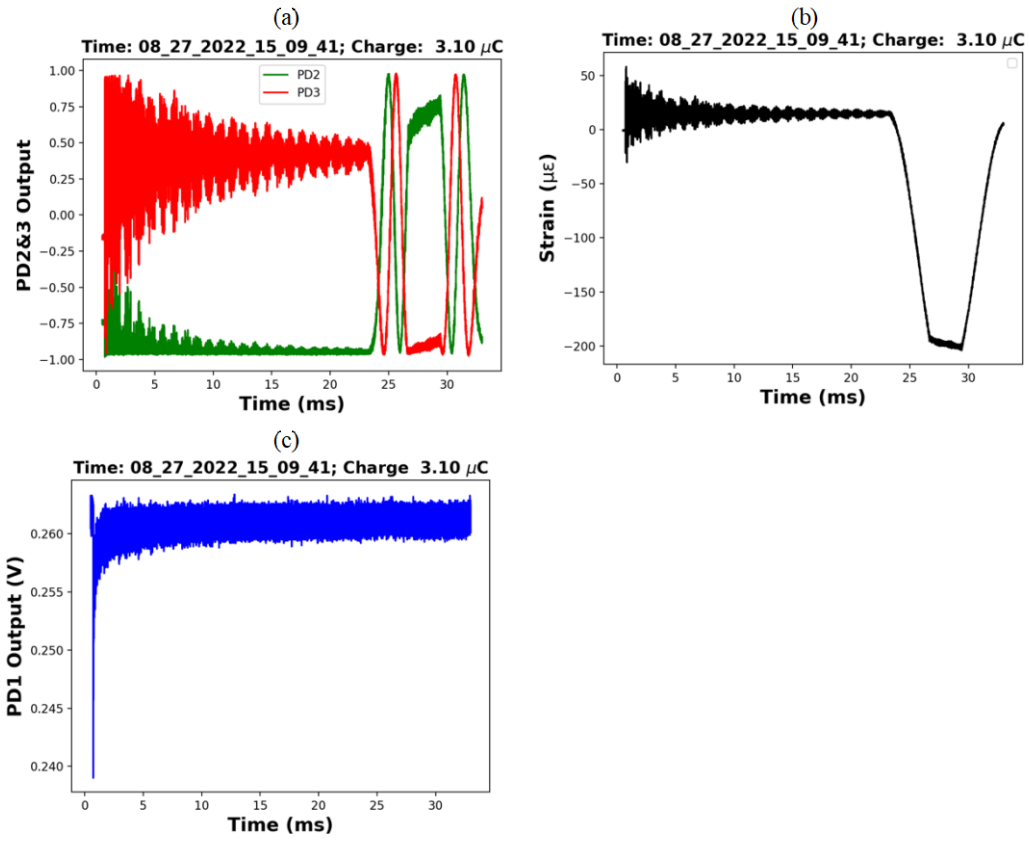

Figure 21. Measurement results from sensor B3O on proton pulse #58. (a) Normalized outputs from PD2 and PD3 in the demodulation module, (b) calculated strain waveform, and (c) PD1 output. Self-calibration process starts after 23 ms.

The strain response right after the proton pulse is shown in Figure 22. Comparison between the strain waveform and PD1 output indicates that the strain starts to show up at ~ 2 μs after the proton pulse. The corresponding interference signal shows very fast variation with bandwidth beyond 100 kHz. The sharp falling edge of the RIA curve agrees with the proton pulse width (< 1 μs).

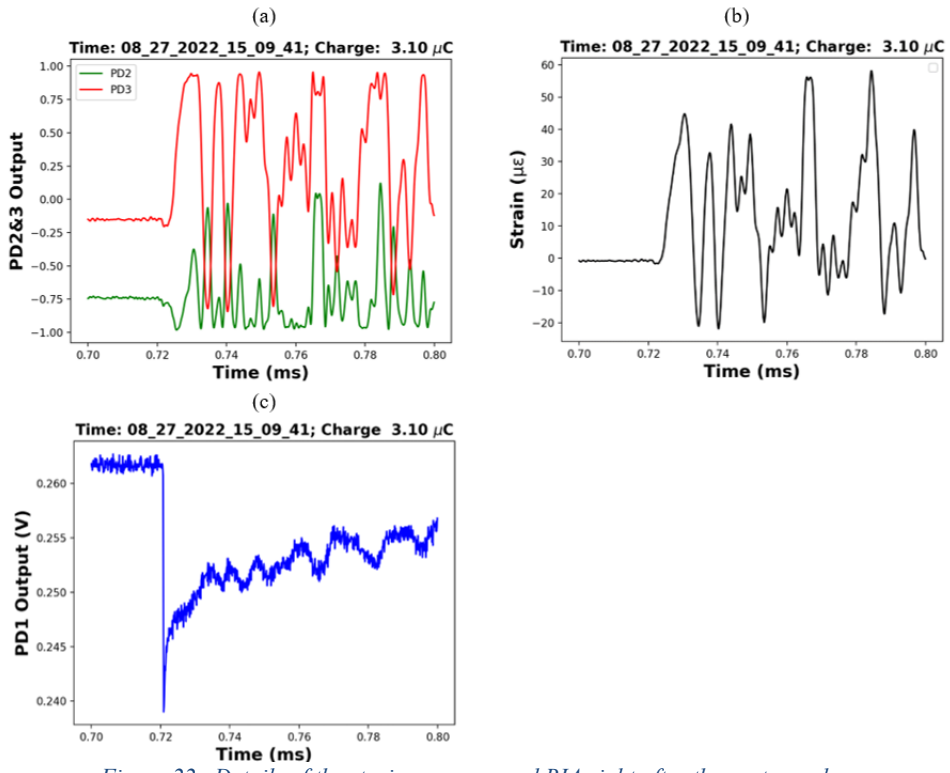

Figure 22. Details of the strain response and RIA right after the proton pulse.

3.3.3 Sensor Layout & Installation

The sensor layout of each block is captured in the attached drawings S07030100-M8U-003-R00, S07030100-M8U-004-R01, and S07030100-M8U-005-R00 for blocks B1, B2, and B3, respectively. Each block has five sensors:

- 1 - front face, vertical strain
- 1 - right face (beam direction), horizontal strain (beam direction)
- 1 - left face (beam direction), vertical strain
- 2 - top face, horizontal strain (transverse to beam direction)

The sensor locations and strain directions were determined with neutronics and structural analysis with the expected nominal beam parameters. The objective was to place sensors at the highest peak strain amplitude locations and directions.

Beam target surfaces were prepared using the following steps in preparation for sensor installation:

- Sanded using 220 grit sandpaper with isopropanol wetting.
- Isopropanol wetted wipes are used to remove residual residue.
- Sanded using 320 grit sandpaper with DI water wetting
- Finished surface preparation with water wetted wipes to remove residual residue.

Strain sensor installation:

- Survey and alignment marked targets for sensor locations.
- Using laser visual fault locator, installed sensor gaps at marked locations on targets.
- Taped sensors to target using Kapton tape at multiple locations for fiber routing.
- Taped tips of sensors.
- Installed thermocouples on targets.
- Preheated targets to 85C using a heat lamp.
- Mixed 2850FT Blue epoxy with catalyst 11 at recommended 100:4.5 ratio by weight using hotplate and stirred to remove bubbles.
- Utilized a wooden pointed applicator to coat strain sensor full length.
- Once 85C was achieved for 4 hours, removed tape from tips of sensors and applied epoxy to tips.
- Once 16 hours had elapsed at 85C, heat lamp was turned off and targets were allowed to cool to 45C to remove tape.
- Sensor signals were checked to verify sensor response.

3.3.4 Data Analysis Method

Strain measurement analysis is automated with a series of Python Jupyter Notebooks. "LANSCE_Experiment_Shot_Key" creates a merged database of shot number, timestamp, and filenames for the strain, radhard camera, and toroid data. "LANSCE_Experiment_Get_Strain" uses the custom module "sns_rad-0.0.1" to read the binary files containing strain measurement data, organize the strain data as a Pandas dataframe, create a time array based on the sample rate of 1MHz, and save the data in Python pickle format.

"LANSCE_Experiment_Strain_Analysis" then reads an individual pickle file to load a dataframe for analysis. First, the strain channels are selected relevant to the target block in question. Figure 23 shows an example of the raw strain signal for a beam pulse. Data past 30 [ms] elapsed time is discarded as it is related to the self-calibration process previously described.

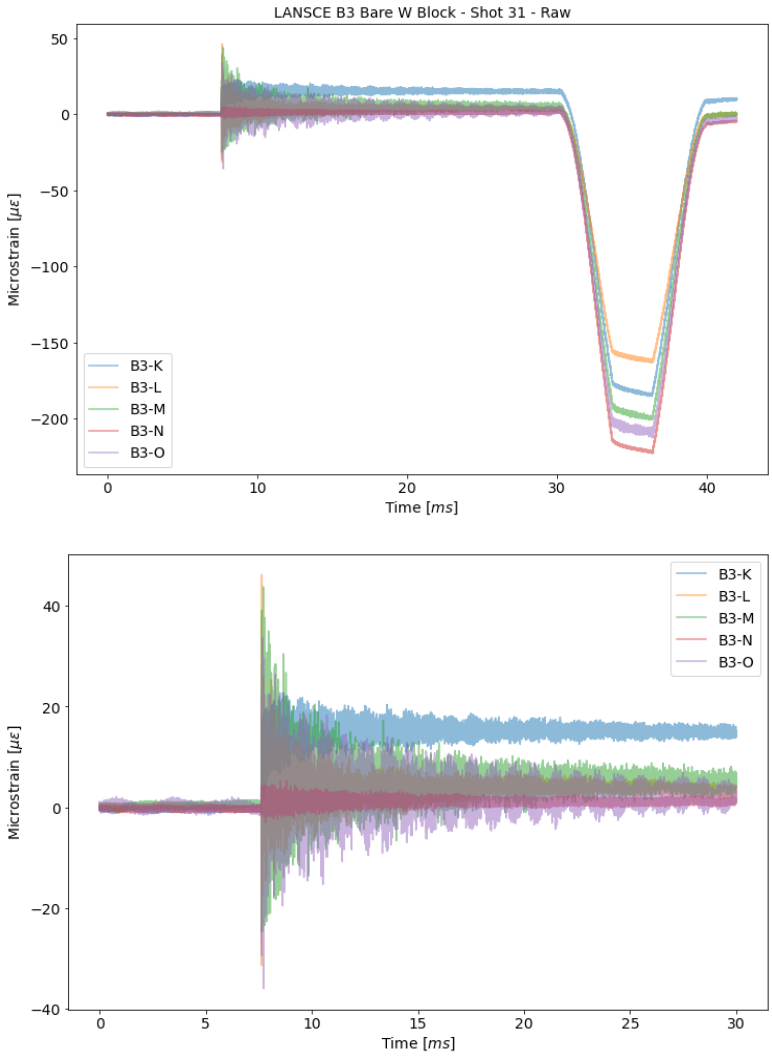

Figure 23: Example strain sensor data from Shot#31 on block B3. Top image is raw data and bottom image is the data with self-calibration process removed.

The next major task is to identify the start of the beam pulse and remove the preceding data. Figure 24 shows a graphical example of the process. The top and front-most sensor (i.e. B, G, or L) is used as it produced consistent and clear signals across all 3 blocks. A running average filter is used to filter the noise and produce a sharp slope discontinuity when the pulse begins. A first-order differentiation of the running average data is then used to isolate the slope discontinuity. The pulse start time is chosen to occur when the derivative (in between the time window of 7 to 8 [ms]) reaches 500 [με/ms]. Five microseconds are subtracted from this value to account for signal rise. This algorithm is found to yield consistent results across all beam pulses. The elapsed time array is then shifted such that the beam pulse begins at $t = 0$ seconds. Figure 25 shows an example of the resulting beam pulse and response signal. The data for negative times then represents the signal noise level for each strain channel.

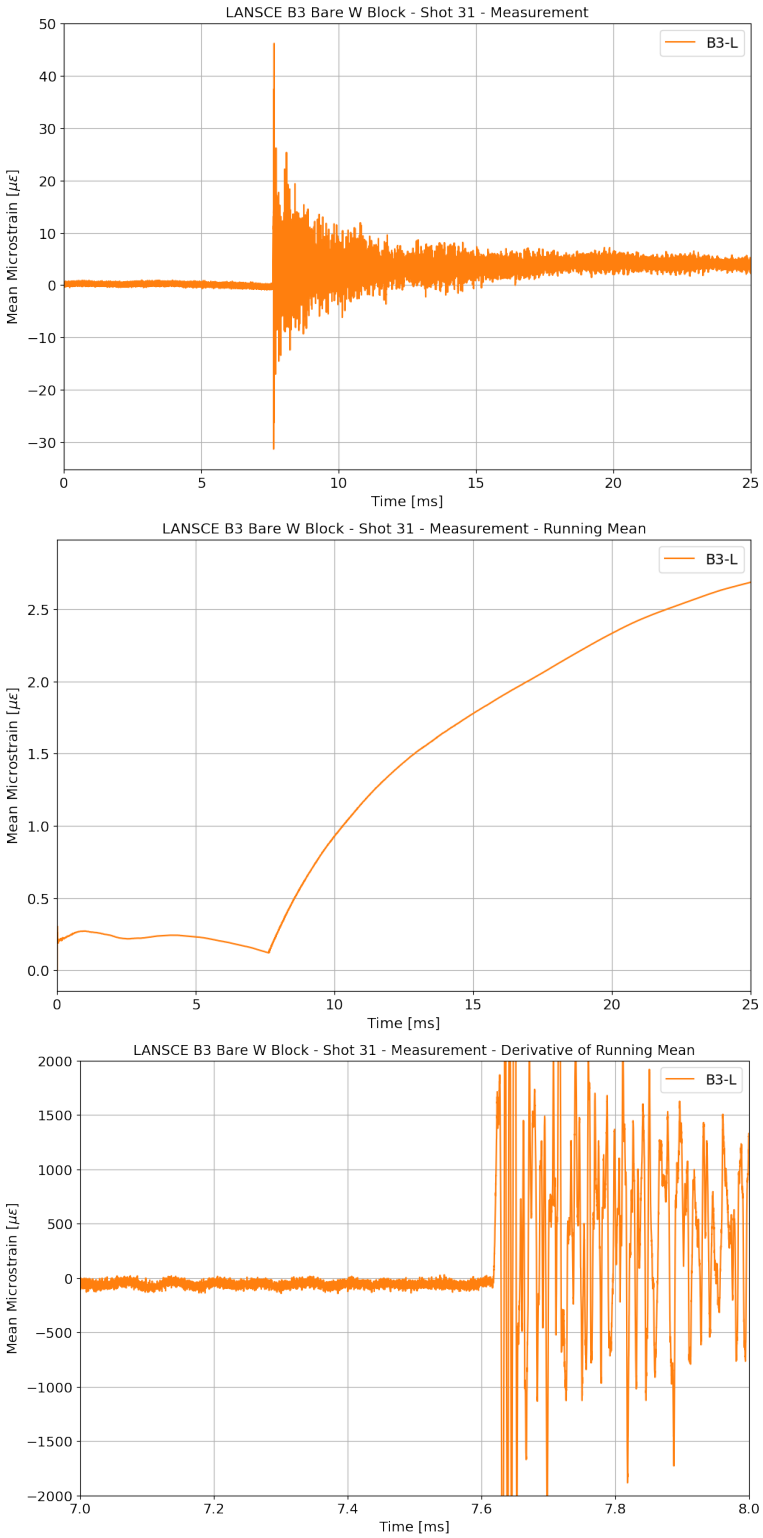

Figure 24: Example beam pulse time identification for Shot#31 on block B3. The algorithm applies to sensors B, G, or L and searches for a jump above threshold for the numerical derivative of the running mean.

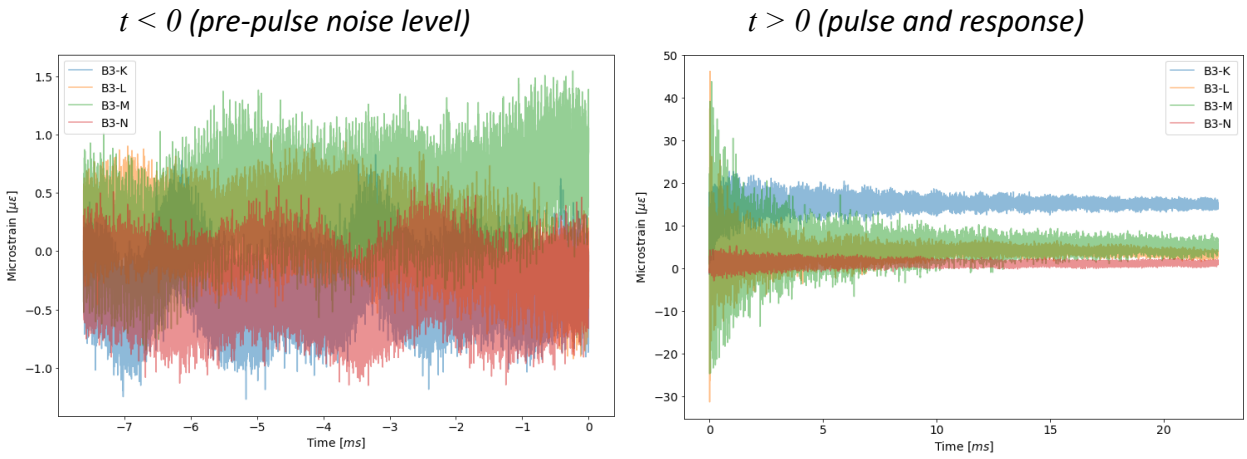

Figure 25: Example beam pulse identification from Shot#31 on block B3. The time array is shifted to place the beam pulse start at t=0. Negative times then show the pre-pulse signal noise and positive times give the beam pulse and associated strain response.

Fourier transforms (FFT) have been used to compare signal frequency content between finite-element simulations and strain measurements. As discussed in Section 5.1 "Pre-Experiment Structural dynamic Simulations", the strain signals' expected frequency content is below 200 [kHz]. Figure 27 gives FFT plots for each sensor in example beam pulses. Several sensors have significant – if not dominant – signal content in the 300-500 [kHz] band. This is most likely due to vibration of the free-end fiber optic cable in the sensor head, behaving as a cantilever. As shown in Figure 26, the sensor head consists of two pieces of fibers assembled inside a capillary tube. Their lengths are not symmetric, and one piece (not sure which one) is much longer than the other. Based on the dimensions, those fibers should be tightly fitting inside the tube and should not have much room to vibrate. Probably due to the fabrication error, some sensors had a loose fit. In such cases, the longer fiber might vibrate in a similar way as a cantilever upon receiving a mechanical shock caused by the proton pulse. One evidence to check this scenario is that the frequency of such vibrations is inversely proportional to the square root of the fiber length inside the tube and should have no dependence on the proton beam power. A second order, digital, Butterworth, low-pass filter is applied to the strain signals to remove this unwanted high-frequency content. The filter is applied forward and backward to give a zero-phase shift to the signal.

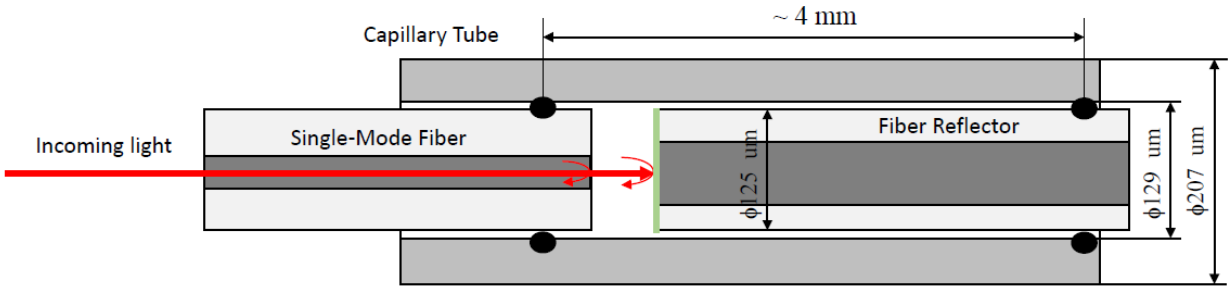

Figure 26: Schematic of the fiber optic strain gage showing the potential of the fiber reflector to act as a cantilever with a higher order vibration mode.

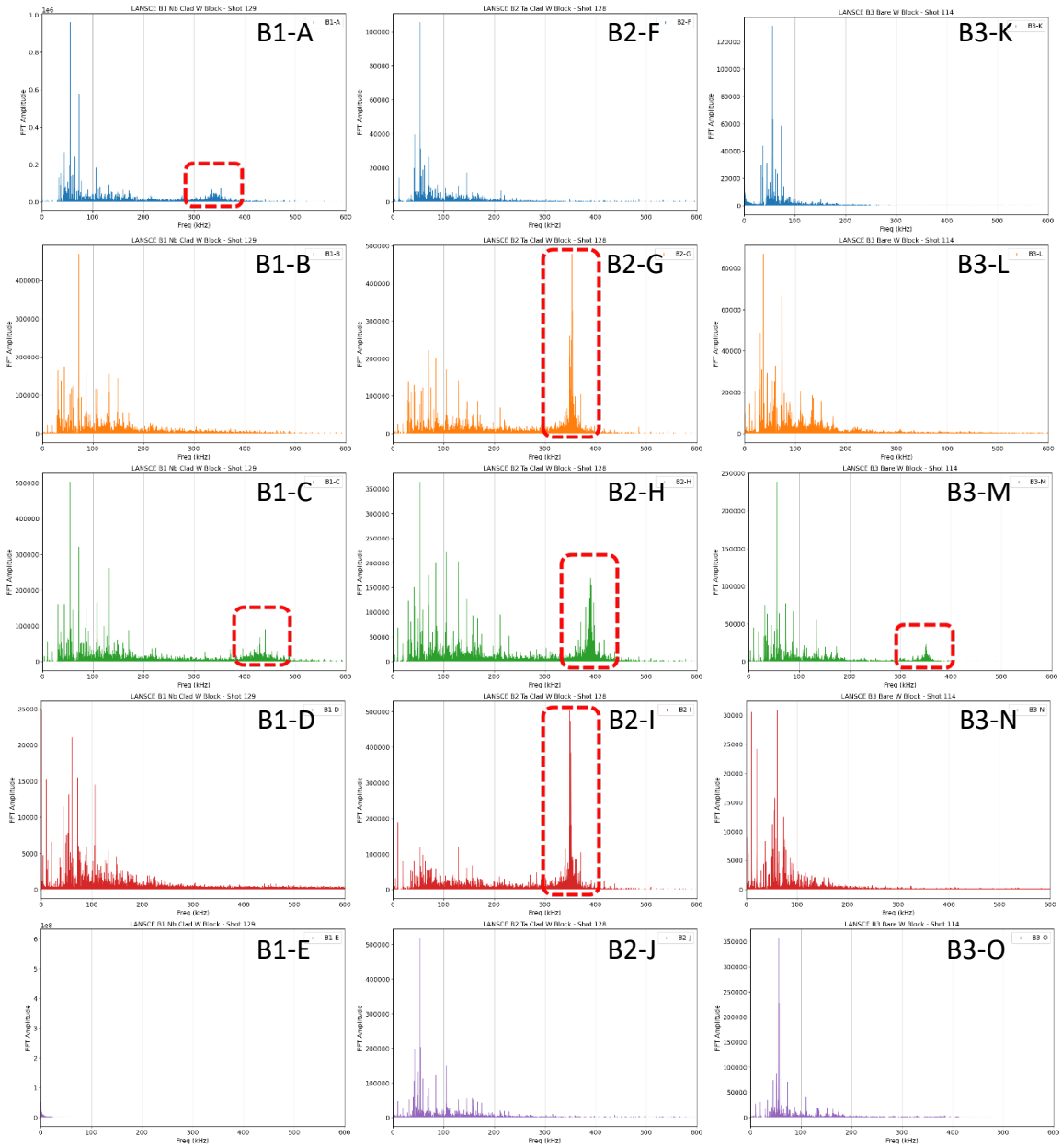

Figure 27: Fourier transforms on example beam pulses for each block. Highlighted regions show high frequency content due to suspected vibration modes of the optical fiber mounted as a cantilever. A 200 [kHz] low-pass digital filter is used to recover the true strain signal.

The final step is to extract strain pulse response characteristics from the filtered data. The peak strain of the filtered signal is recorded along with the timestamp. Also, a Python implementation of the ASTM E1049-85 rainflow cycle counting algorithm [21, 22] is used to record the peak strain amplitude, the number of cycles associated with this amplitude, the start time of this cycle, and the end time of this cycle.

3.4 BEAM CURRENT, POSITION, AND INTENSITY MEASUREMENT

3.4.1 Measurement Methods

The beam pulse intensity and shape on the target samples is measured by two types of devices:

1. A toroid with a 30 MHz bandwidth to measure the longitudinal profile of the proton beam current. This toroid has been calibrated with the installed cable. The charge and thus the number of particles is calculated by summing the beam current waveform after subtracting the baseline. A backup measurement was taken from a LANL installed toroid with an estimated calibration value.

2. An imaging system consisting of a luminescent screen and cameras with zoom lenses captures the transverse 2D profile of the proton beam.

3.4.1.1 Beam Current Measurement

The toroid from Pearson Electronics is model 8586 with a diameter of 5 inches, see Appendix C. The bandwidth is 30 MHz, and the droop rate is 2%/μs. The toroid's 1 V/A sensitivity (unterminated) has been verified with a calibration procedure performed in the 8600 SB-05 STS Lab. The procedure uses a pulser with its signal, a short pulse of 300 ns, going through a calibrated resistor and the voltage over the resistor measured with a calibrated scope to calculate the current. The wire with the current is routed through the toroid. We then measured the toroid's output voltage terminated at 50 Ohms and using the same cable used at the LANSCE experiment to account for DC resistance of the long cable to obtain the V/A, 0.486, for the experiment. The installed toroid is shown in Figure 28. During the experiment, to prevent saturation of the digitizer, attenuators have been placed inline and the calibration values properly adjusted.

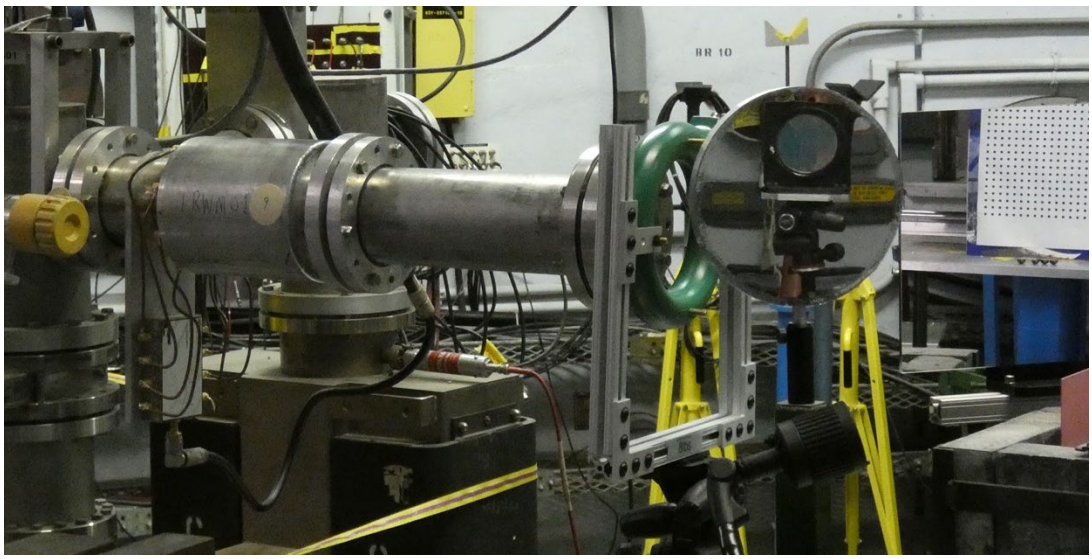

Figure 28: The toroid (green) installed in air.

3.4.1.2 Imaging System

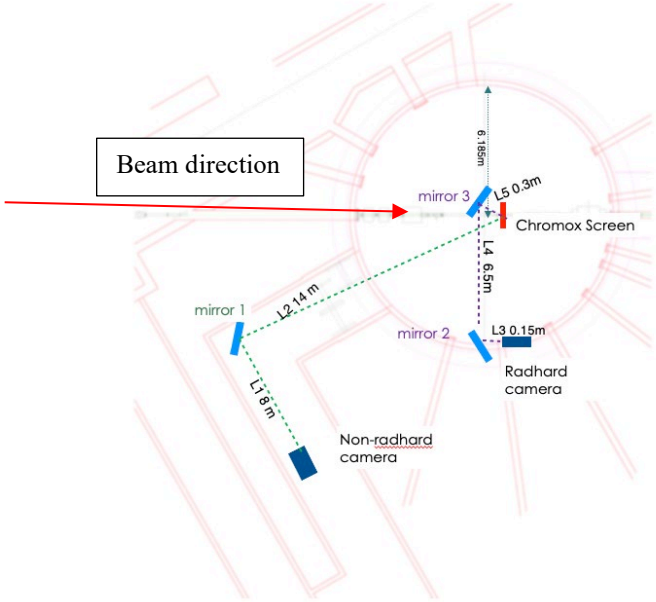

Figure 29: The locations of the non-radhard and radhard cameras.

To view the location and transverse size of the proton beam, a chromox screen was placed right in front of the target samples, see Figure 13. The protons hitting the screen cause scintillation with a wavelength of 690 nm thus visualizing the transverse profile of the beam. The imaging system consists of two cameras:

- non-radhard: Allied Vision G235B with a Sony IMX174 sensor with 1936 x 1216 pixels of 5.86 x 5.86 µm size,
- radhard: Spectral Instruments RVT100 Radiation Hard Camera with a CMOSIS/ams CMV2000 image sensor with 2048 x 1088 pixels and 5.5 by 5.5 µm size pixel.

The non-radhard camera was placed in the walkway into the room to protect it from direct radiation. To simplify the setup a single mirror was used to view the screen. Shield walls were in place to minimize radiation going into the walkway. Other configurations, with more mirrors and more shielding are possible but were rejected as unnecessarily complicating the optical setup, given that a second camera is available. The non-radhard camera had no issues at this location and did not have to be restarted due to instant radiation. The longer distance did lower the image quality versus the radiation hardened camera.

The radhard camera was placed in the blue room behind a shield of steel bricks and out of the direct shine of the beam. The closer location to the screen allowed it to give better images than the camera placed further away given similar quality zoom lenses. Its camera head was separated from most of the processing electronics by a 100 m optical cable to minimize the impact of the radiation on the camera. The mirrors used were type 8-λ flat mirrors of different sizes.
The zoom lenses used were:

- Nikon AF 80-200mm f/2.8D ED (77mm) for the radhard camera
- Nikon AF-S NIKKOR 200-500mm f/5.6E ED VR for the non-radhard camera

3.4.2 Data Acquisition System and software

The rack mounted data acquisition system, see figure Figure 30, consists of a NI PXIe-1092 PXI Chassis with:

- NI PXIe-8881 (Computer, Xeon W-2245 CPU @ 3.90GHz with 32 Gb RAM)
- NI PXIe-5122 (2-Channel, 100MS/s 14-bit digitizer)
- NI PXIe-8245 (4-port Ethernet)
- NI PXI-5114 (Backup 2-Channel, 250 MS/s, 8-Bit digitizer)
- NI PXIe-5122 (Spare 2-Channel 100MS/s 14-bit digitizer)

Other equipment in the rack includes:

- Two pulse delay Generators (DG235) to trigger the digitizers, cameras, and laser vibrometers
- Laser vibrometer and rack-mounted PC
- Power supplies for the two cameras
- Spare rack-mounted PC

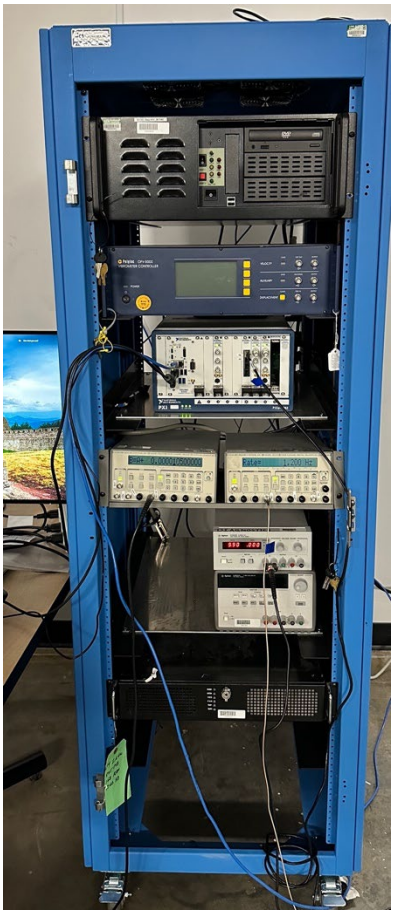

Figure 30: Photo of the data-acquisition rack.

The PXI computer runs MS Windows 10 and LabVIEW 2017 and runs the data acquisition software.

3.4.3 Data Acquisition Software

The software acquiring, displaying, and saving the measurements consists of several parts. The parts are communicating with each other to each's other measurements. For example, the current monitor program shares the total charge with the image acquisition so the peak density can be calculated. The programs are based on earlier software used at previous First Target Station experiments at LANSCE and on code used in the SNS accelerator. Image acquisition for radhard camera, see Figure 31. The code repository is at https://code.ornl.gov/bl9/sts-lanl.

- Image acquisition for non-radhard camera, see Figure 32.
- Beam current acquisition and analysis, see Figure 32.
- Console program collecting and displaying all data, see
- Figure 33.
- Data inspector: inspect the saved data after acquisition, Figure 34.
- Calibration programs for beam current monitor, see Figure 35.
- Calibration for cameras, see Figure 36.

Each acquisition program archives its own data. The console program collects all the data and calculations and tags the data with the shot number and again saves the data for redundancy. The toroid was calibrated in the lab while the camera was calibrated in the field. We did an initial calibration with the camera calibration program so that the image acquisition programs can tell us in real-time the beam position and size; however, we found that we can set the cameras exposure and gain such that when the beam luminesces the screen, we can still see the chromox screen edges and markers and that calibration is possible for each image afterwards.

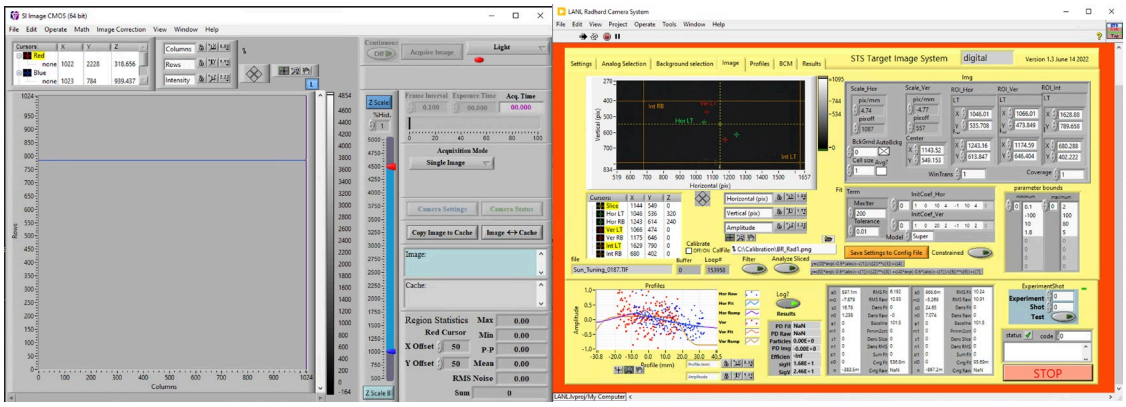

Figure 31: Vendor camera program producing the image (left) and STS LabVIEW program reading the image and calculating beam sizes as well as saving the image and results.

Figure 32: On the left, the image acquisition program for non-radhard camera, setting up the camera parameters, acquiring the image, reading the image, and calculating beam sizes as well as saving the image and results. On the right, the program to acquire the beam current waveform and calculate the charge per pulse.

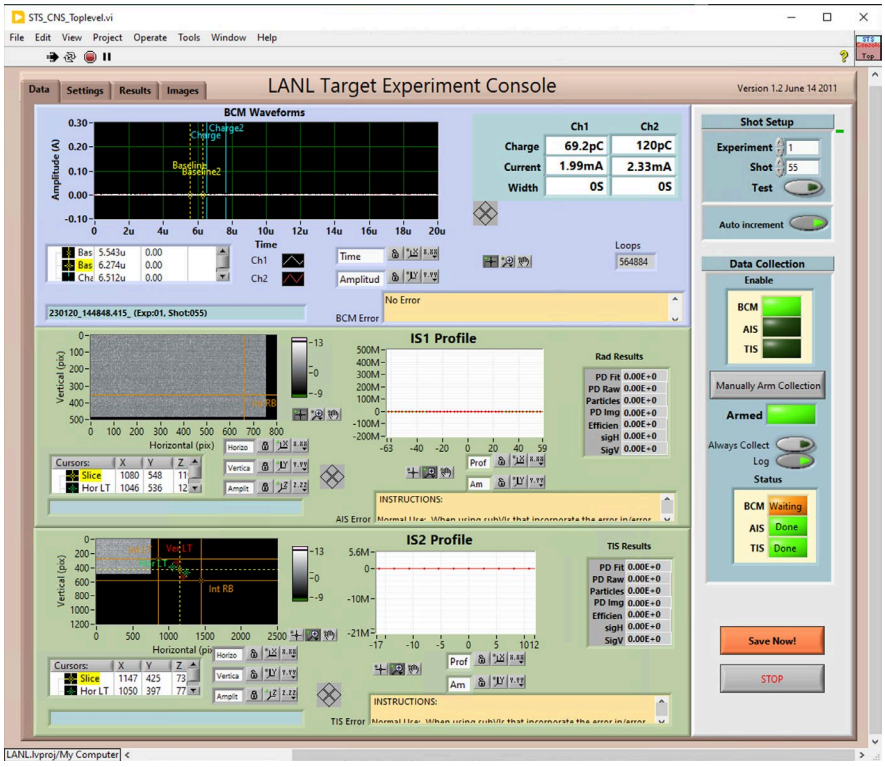

Figure 33: Console program to collect all data.

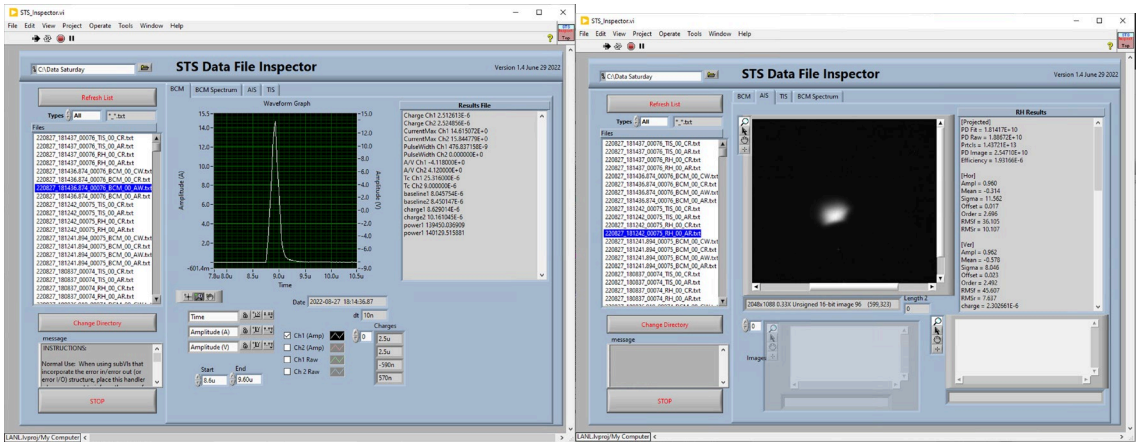

Figure 34: Data Inspector program to view the saved images and beam current waveform. The left shows a current waveform, while on the right an image from the radhard camera.

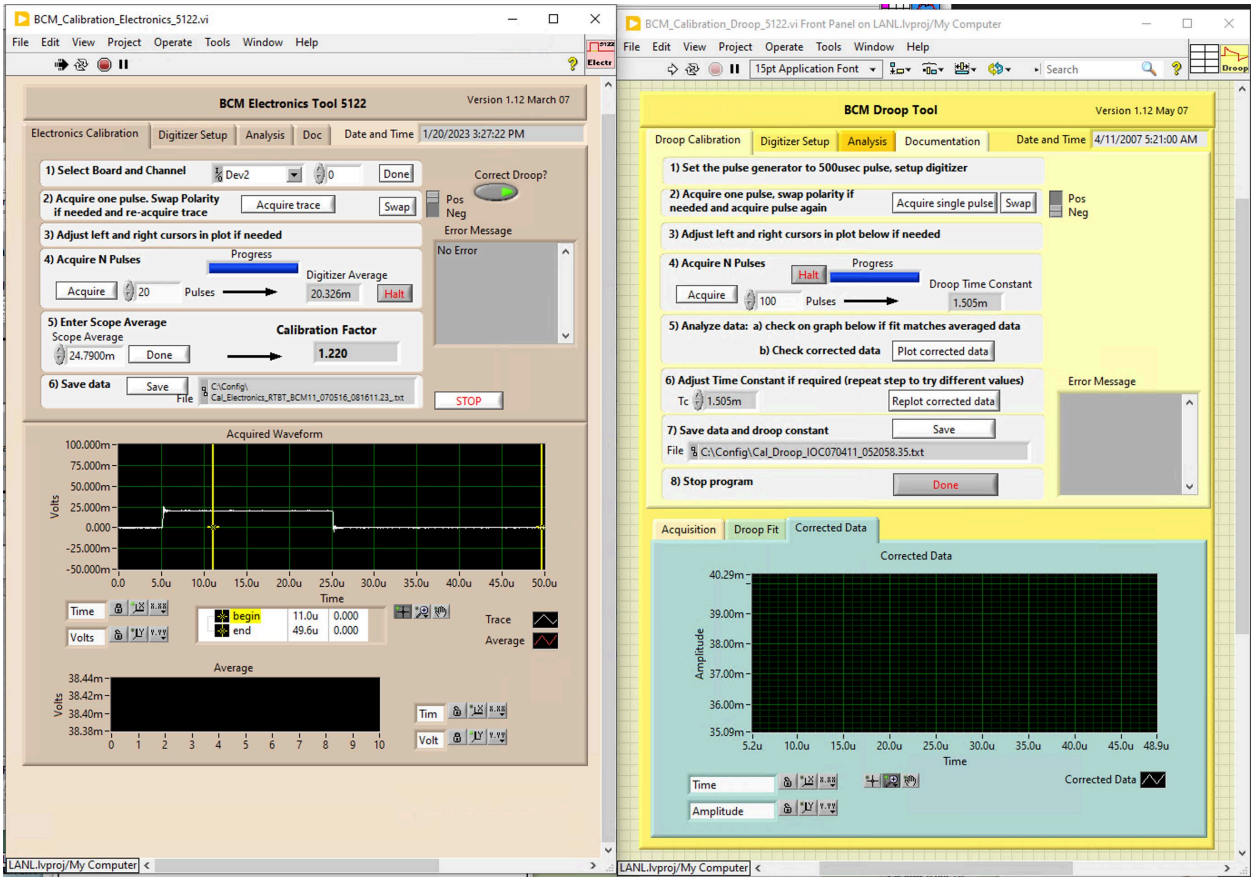

Figure 35: Calibration programs to determine V/A coefficient and droop time of toroid.

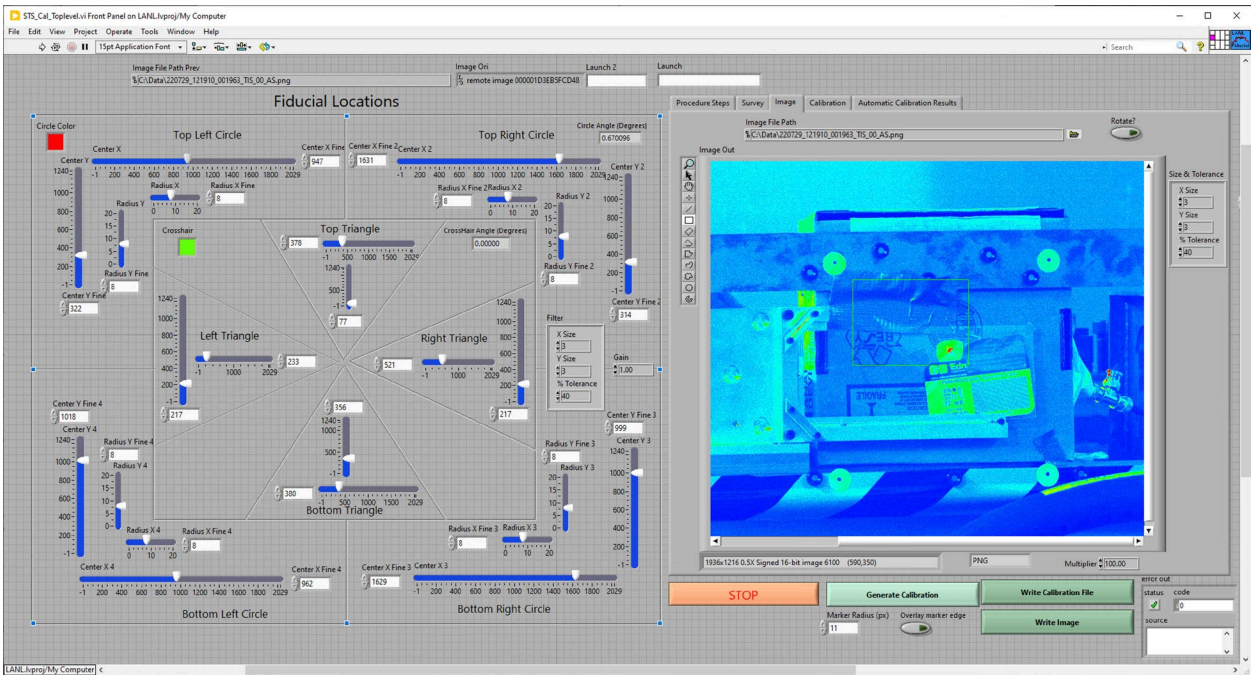

Figure 36: Camera calibration program to determine center and pixels per millimeter.

3.4.4 Cable Plan

We prepared a combined cable to minimize the amount of time spent on cable pulls during installation of the experiment. During previous visits to LANSCE, we measured distances for the different cables, see Figure 37 and Figure 38.

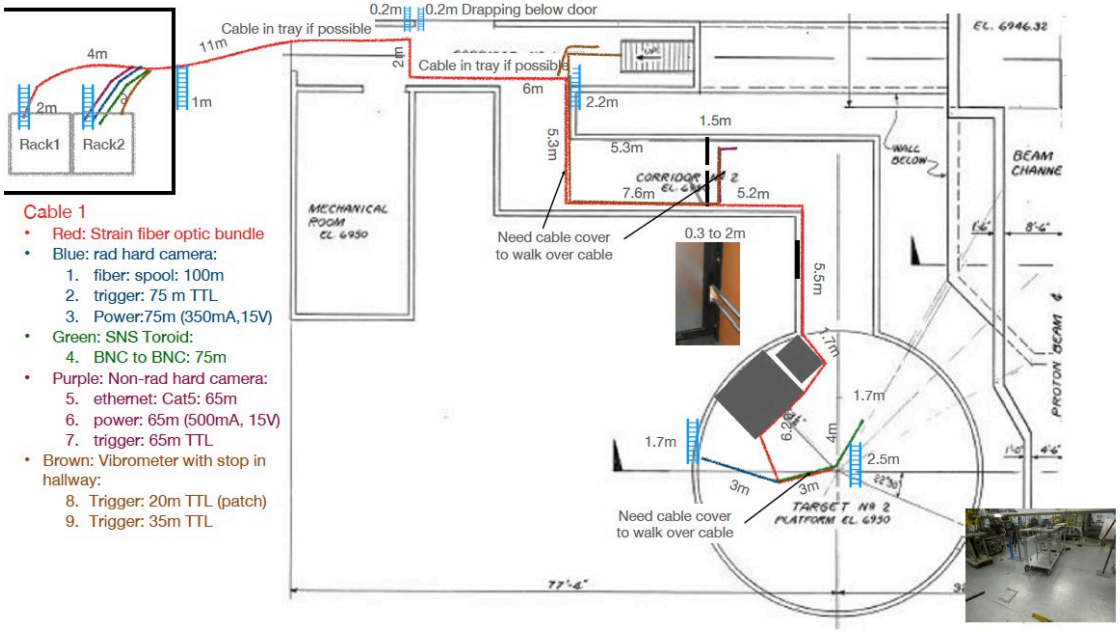

Figure 37: Cable distances and routing.

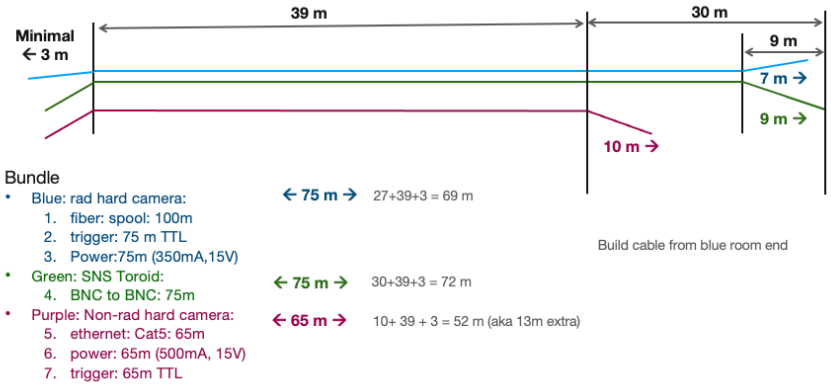

Figure 38: Cable to the blue room.

3.4.5 Data Analysis Methods

Beam measurement analysis is automated with a series of Python Jupyter Notebooks. "LANSCE_Experiment_Shot_Key" creates a merged database of shot number, timestamp, and filenames for the strain, radhard camera, and toroid data. This file runs "LANSCE_Experiment_Image_Analysis" for each beam pulse. Figure 39 shows an example beam pulse image from the radhard camera. The image is read as a 2048 x 1088 pixel PNG format in grayscale with 32-bit signed integer pixels. The image is colorized according to pixel intensity with a pixel grid overlay.

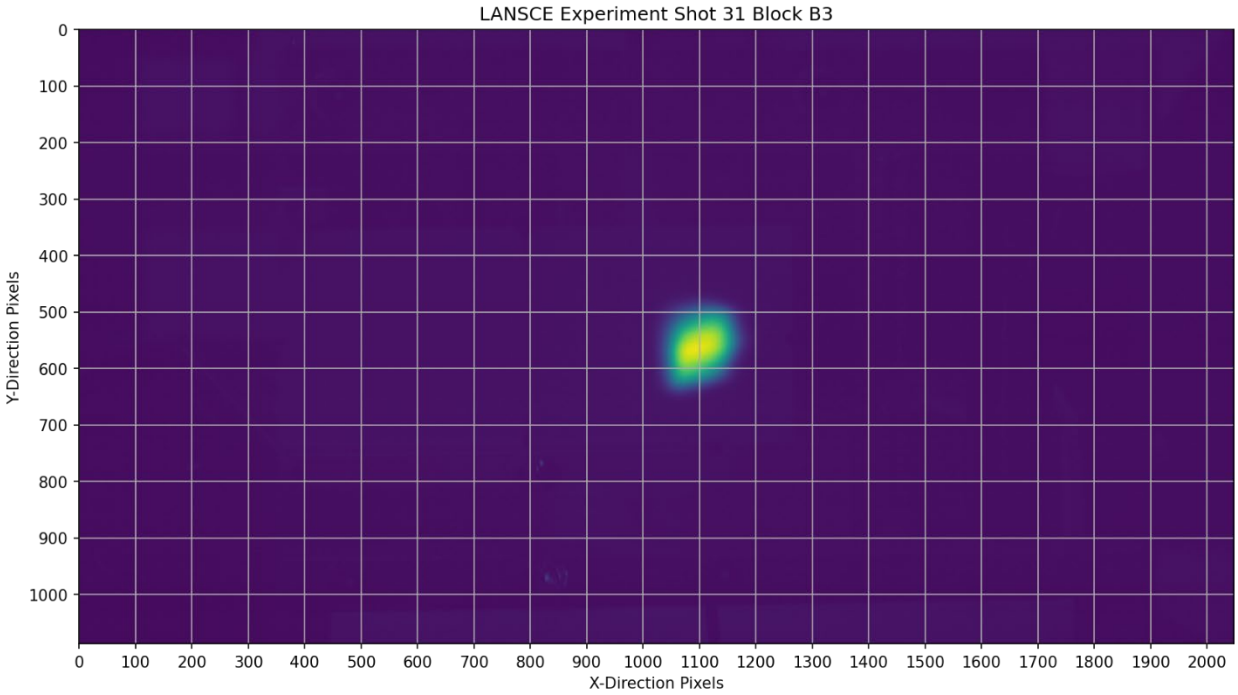

Figure 39: Example radhard camera image from beam Shot#31 on block B3. A viridis color map is applied to the grayscale image with a pixel grid overlay.

The metrology fiducials are located by rescaling the image. First, the pixel intensity values are scaled to 8-bit (0-255). Any pixel with intensity greater than 25 is reset to a value of 0. (This essentially removes the beam.) Any pixel with intensity less than 25 then has 230 added. The new pixel intensities are then linearly rescaled from [230-255] to [0-255] to reveal the image background. Figure 40 (bottom) shows the modified image. The 4 white dots are overlayed against the 4 fiducials used for spatial location. The fiducial pixel coordinates must be manually determined from each file. These were spot-checked and found to be consistent (within the accuracy of finding the center of each fiducial reflection) for shots on each block. In other words, the motorized linear translation stage was reproducible.

The 4 fiducials were not set up to be colinear, however, they are on the same spatial plane. As a first order approximation, we assume the image is rotated only about a vertical axis. Then, the aspect ratio of the image needs to be scaled using the fiducials. The length-to-pixel scaling in the x-direction is calculated for both the top and bottom set of fiducials and is then averaged. Also, the length-to-pixel scaling in the y-direction is calculated for both the left and right set of fiducials and is averaged. Now the metrology origin can be located on the image as well as the block position and outline (see Figure 40). The metrology coordinates that were used for the calculations are given in “Lansce_Experiment_Fiducials.pdf”.

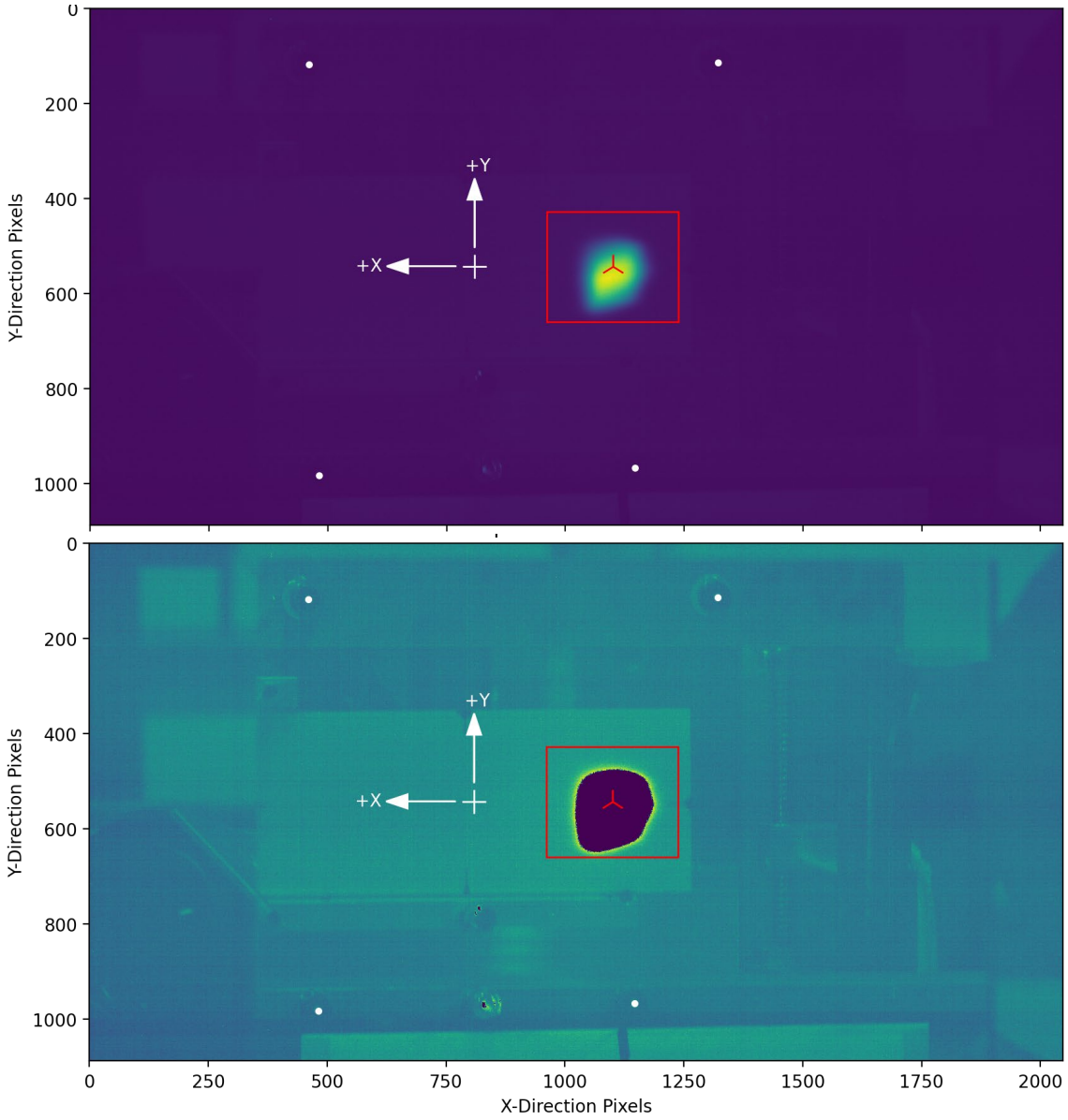

Figure 40: Example fiducial location for beam Shot#31 on block B3. The beam is removed and the image is rescaled to reveal the background (bottom). Fiducials are indicated along with the metrology coordinate system and the block front outline. The same information is shown on the original image (top).

Figure 41 shows an example of the method used to find the image background level. The original image, with the block outline removed, is shown along with a histogram of the pixel intensities. There is clear central tendency to an average value. This is calculated and then subtracted from the beam portion of the image. Figure 42 shows an example of the resulting beam image over a target block. A 3D surface plot and 2D plots of the horizontal and vertical centerlines show additional detail including relatively low noise.

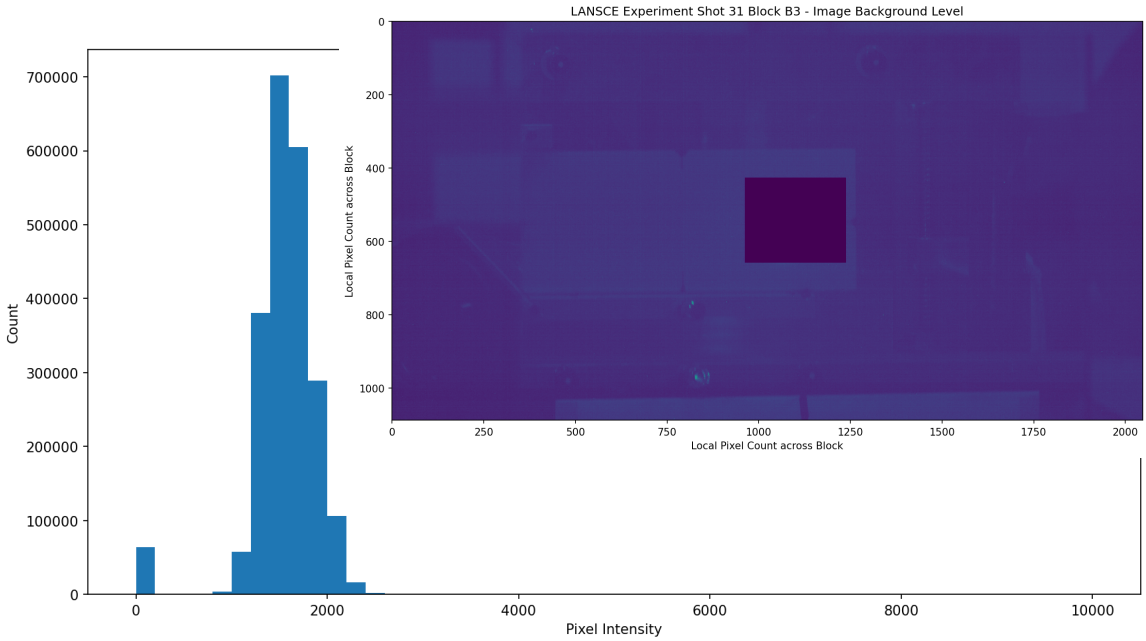

Figure 41: Example image background level for Shot#31 on block B3. The image portion over the block has been removed. The remaining pixel intensity content is well-defined by an average.

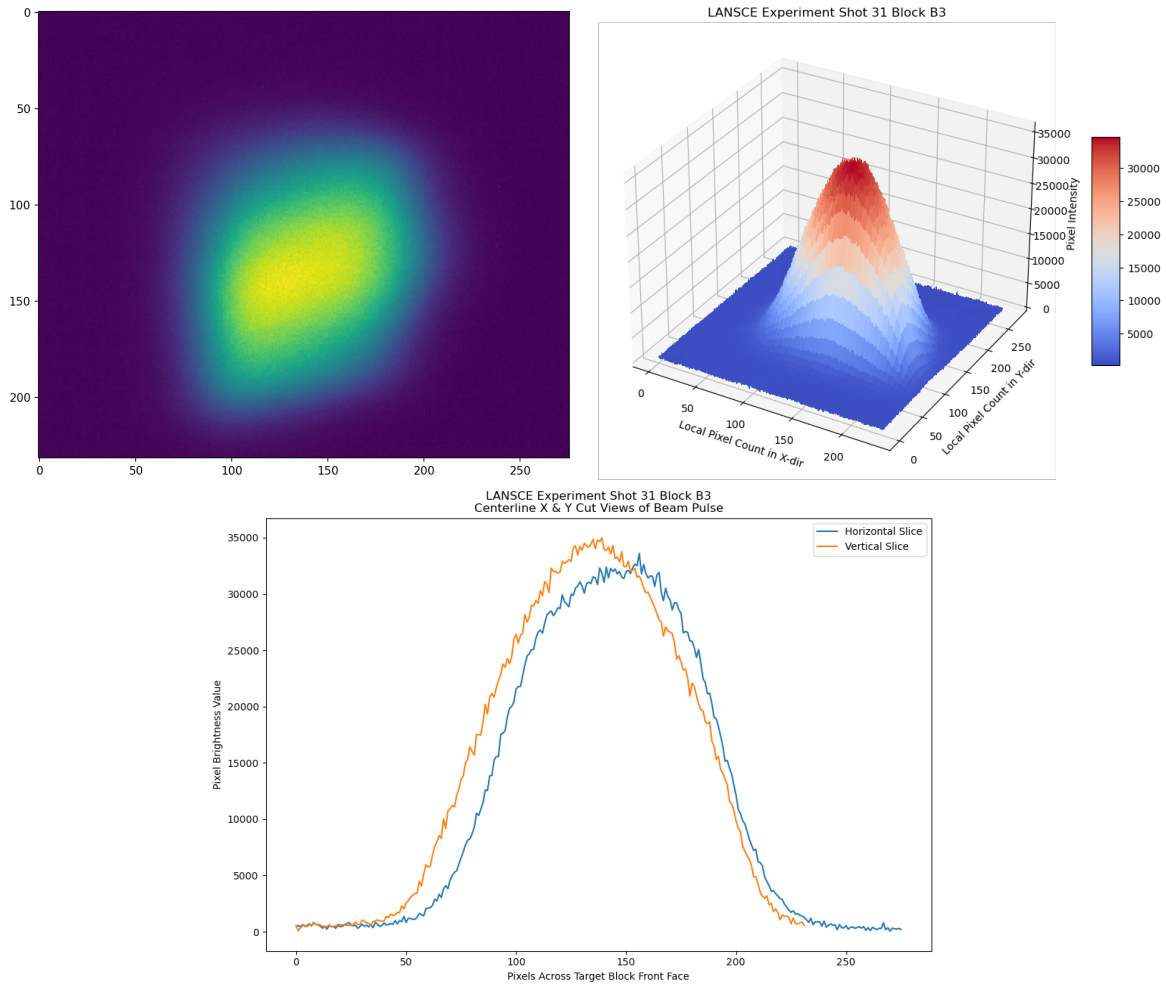

Figure 42: Example beam pulse image over block B3 (with background removed) for Shot#31. A 3D surface plot provides additional visualization. 2D slices of the vertical and horizontal image centerlines show high signal-to-noise.

Figure 43 shows an example toroid beam pulse measurement signal. A trapezoidal numerical integration function is used to integrate the beam current over time and obtain a beam charge in micro-Coulombs.

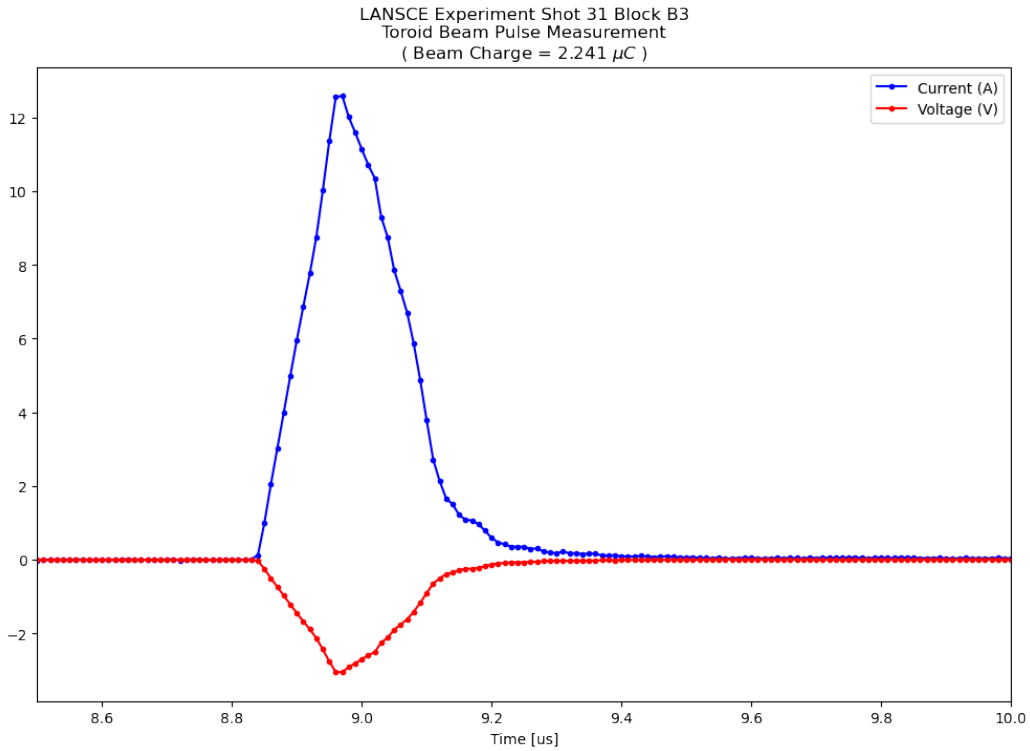

Figure 43: Example toroid beam measurement for Shot#31 on block B3. The beam current signal is numerically integrated with time to find the total beam charge in micro-Coulombs.

3.5 RADIATION DOSE MEASUREMENT

Dosimeters were placed in various locations to document the radiation field during the experiment. This will help us in future planning of camera locations and shielding effectiveness as well as a reference for the neutronics calculations. We placed both high radiation (HR) and low dose radiation dosimeters (LD). The locations are shown in Figure 44 and a photo of the shield walls is shown in Figure 45. The total doses were low and the total doses for HR dosimeters, except for one case, were below their lower threshold for accuracy. We see that placing the camera around the corner in the hallway lowered the total dose by a factor of 10. Neither doses would damage the sensors, but the risk is that the instantaneous radiation crashes the non-radhard camera. The radhard camera, shielded behind a steel block, had a higher dose but was not affected. Its closer proximity gave a higher quality image versus the non-radhard camera and therefore was the preferred measurement.

HR Dosimeter	Dose (Gy)	Location
1-2	~2	Halfway T and RHC
3-4	~2	HR Cam
5-6	16	Target 1st shelf
7-8	~2	First Hallway
9-10	~6	Target 2nd shelf
11-12	<< 10	Dig Camera
13-14	<< 10	Reference
Note: HR Dosimeters not accurate below 10 Gy		

LD Dosimeter	Dose (Rad)	Location
333467,908907	0	Reference
909492,319950	20	HR Cam
300702,910641	.43	Dig Camera
300086,910066	5.8	Last shield wall
333186,906887	0.4	Near alignment head

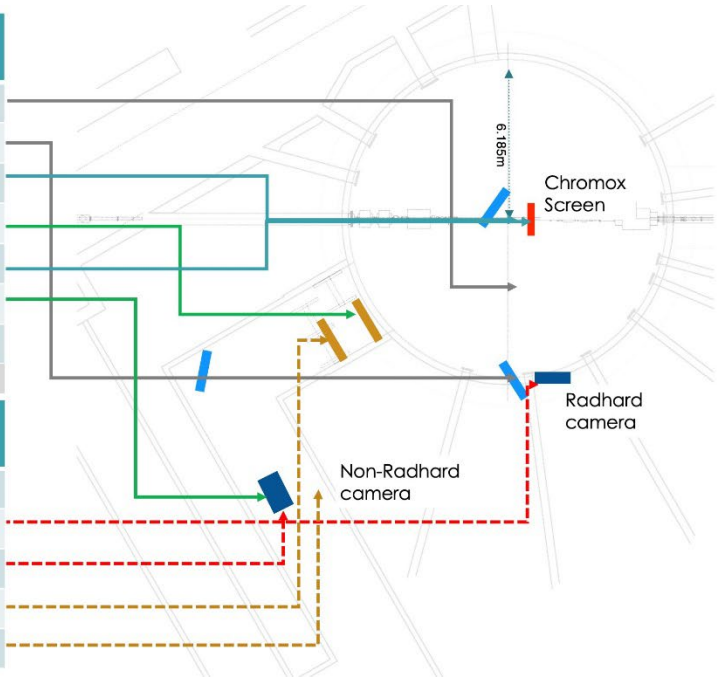

Figure 44: Location of dosimeters.

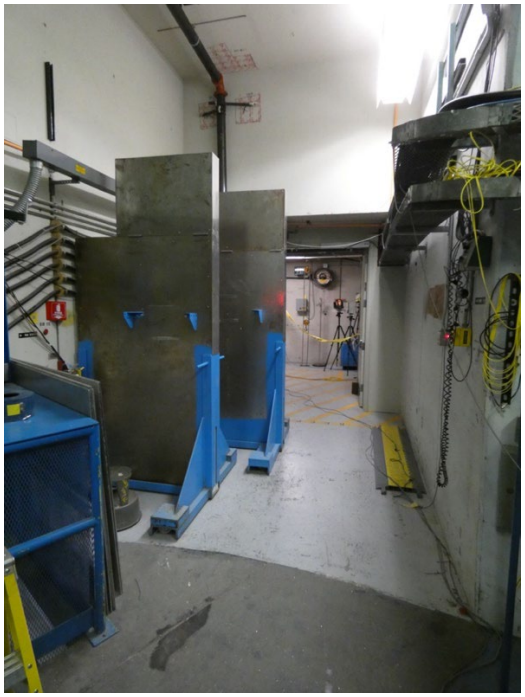

Figure 45: Location of shield walls.

3.5.1 Notes on readout of dosimeters

The dosimeters were processed with the 1% transmission factor neutral density filters in place. Please note that we did see some photon signal on the "reference" HBG dosimeter to the tune of about 70 mrem.

We use the operational quantity, Hp(10), so our neutron correction factors are based on the fluence to personal dose equivalent coefficients in ICRP 74. Based on the historical Bonner sphere measurements made in establishing our correction factors, for D_2O moderated Cf-252, the effective quality factor would be on the order of 9.5. The dosimeters readouts are listed in Table 2.

Table 2. Dosimeter report

Group File 42210111				
Location	Dosimeter	Hp(0.07) (rem)	Hp(3) (rem)	Hp(10,gamma) (rem)
Reference	333467	0.07	0.07	0.07
HR Cam	319950	16.71	13.27	11.50
Dig camera	300702	0.37	0.31	0.28
Last shield wall	300086	4.34	4.34	4.11
Near alignment head	333186	0.26	0.25	0.22

Group File 42210112		
Location	Dosimeter	Hp(10,neutron) (D2O-Cf rem)
Reference	908907	0.00
HR Cam	909492	91.42
Dig camera	910641	1.59
Last shield wall	910066	16.38
Near alignment head	906887	1.72

4. SIMULATION METHOD

4.1 OVERVIEW

As will be seen in the results, the LANSCE proton beam experienced large variations in charge and shape that were markedly different from the pre-experiment Gaussian predictions. To account for the beam variations, a custom proton source was created for each experimental beam pulse. The measured beam charge and beam image for each shot were combined to create a pixelated array of protons. Thus, a custom source was matched for each beam shot and then used for structural dynamics simulations.

4.2 NEUTRONICS

4.2.1 Radiation Transport Source Definition

The radhard camera image and the toroid beam current measurement can be combined to produce an array of protons that were delivered to each block for its beam pulse. The procedure is to first divide the integrated beam charge by the atomic unit of charge to obtain the total number of protons in the beam pulse, N_p. The goal is to scale the radhard camera image into an array of protons per pixel,

$$N_p = \iint I \, dx \, dy \approx \Delta x \, \Delta y \sum I_{pix}$$

where I is the current density (protons/cm^2). The current density, I, is related to pixel brightness level, L, via a conversion factor, S, such that

$$I_{pix} = L_{pix} * S$$

The conversion factor for each beam pulse can thus be determined,

$$S = \frac{N_p}{\Delta x \Delta y \sum L_{pix}}$$

where Δx and Δy are the pixel width and height and $\sum L_{pix}$ is the sum of the beam pulse array (e.g. the sum of all brightness levels in Figure 42). Figure 46 shows an example of a beam shot after conversion to protons per pixel.

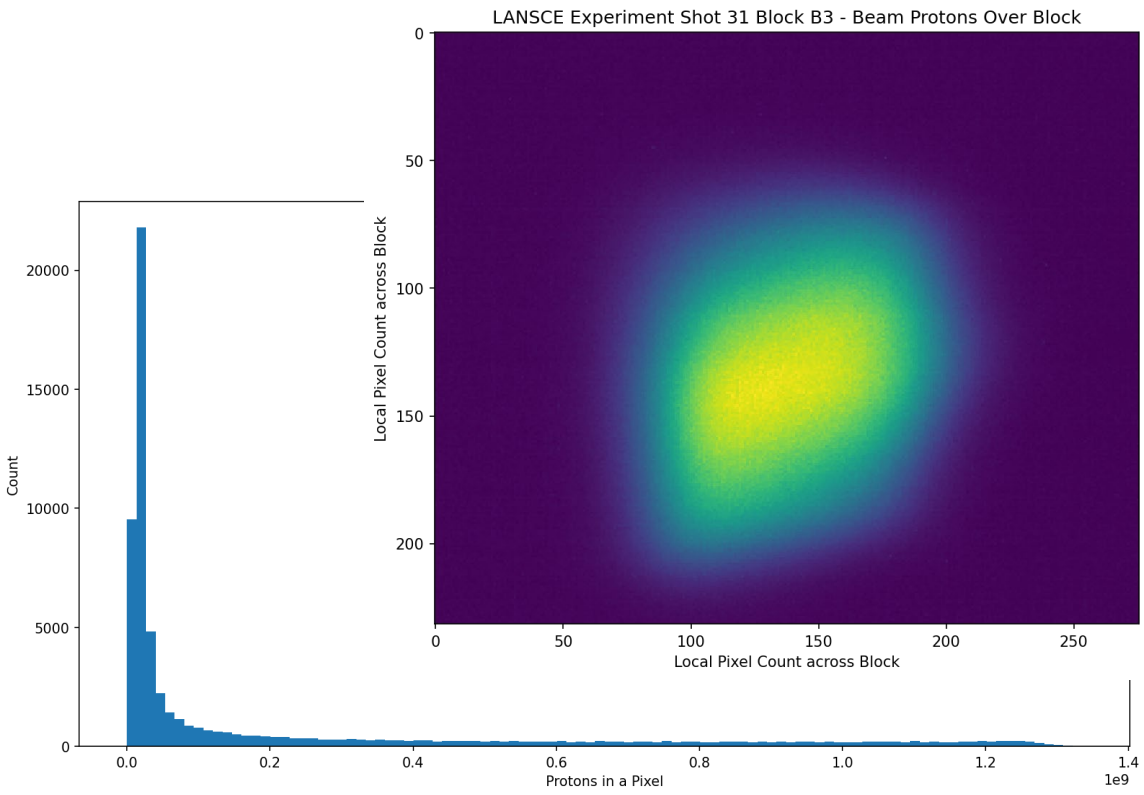

Figure 46: Example proton array for Shot#31 on block B3. The numerical array consists of proton counts. When viewed as an image, the intensity of each pixel indicates the number of protons crossing that area of space. The sum of the intensities of every pixel (i.e. the sum of the array) then yields the total number of protons delivered in the pulse. A histogram of the data is also shown.

Before serving as an input into a neutronics analysis, the proton array must be converted from the metrology coordinate system to the CAD coordinate system (CS). As shown in Figure 47, the CAD CS origin is at the front center of Block 2 and the x-axis corresponds to the beam axis. In the metrology CS, the z-axis corresponds to the beam axis, and the center of Block 2 is at $(x, y) = (0.002", -0.013")$. By inspection, the coordinate transformation is then

$$Y_{CAD} = Y_{MET} + 0.03302\ cm$$

$$Z_{CAD} = 0.00508\ cm - X_{MET}$$

where units are in centimeters, "CAD" refers to the CAD CS, and "MET" refers to the metrology CS. Figure 48 shows an example proton array after conversion into the CAD coordinate system.

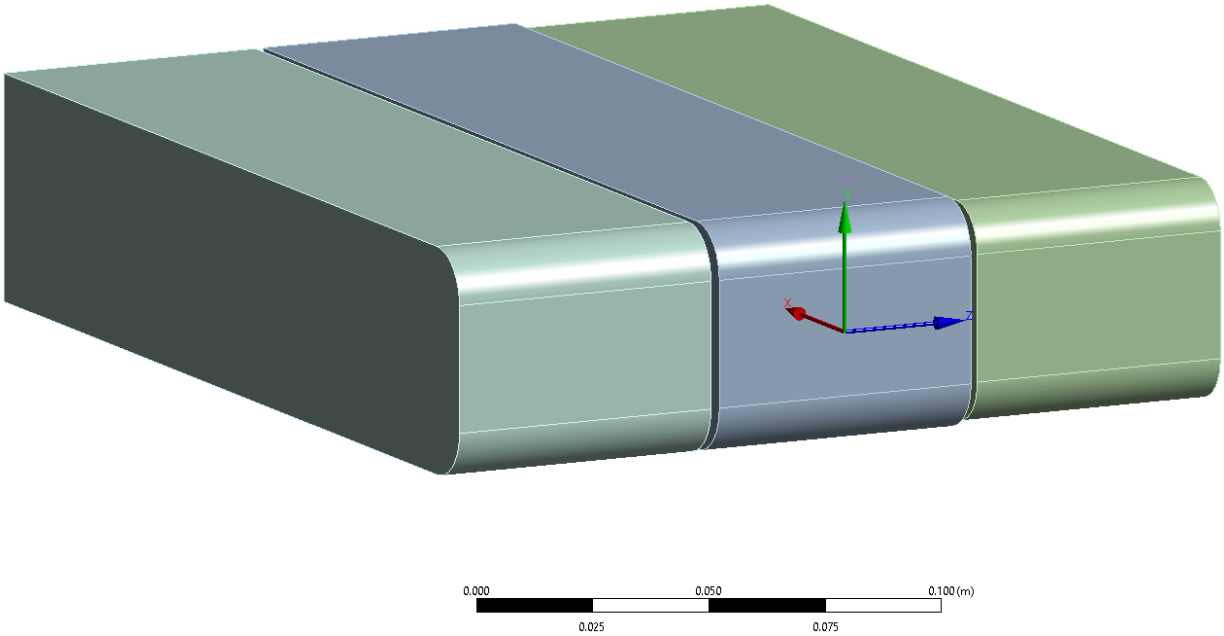

Figure 47: CAD model of target blocks showing coordinate system origin at the front center of block 2. All 3 tungsten blocks are aligned. Thus, the clad blocks are situated 1 mm proud of the bare tungsten block.

The two-dimensional proton probability density array, now defined in the CAD coordinate system, is then used to create an MCNP6-compatible source definition to serve as input for neutronics simulations. Each unique beam shot has an associated unique MCNP6 source definition. A shortened example of one of the MCNP6 source definitions created in this work is provided in Figure 39. All source definitions used follow a common template. In this template, source particles are sampled from a mono-directional, mono-energetic, planar distribution as a function of probability assigned by the proton probability density array obtained using the radhard camera. Once the appropriate array element has been sampled, the exact Y_{CAD} and Z_{CAD} positions are then sampled uniformly from the appropriate range(s) associated with that array element. The sampling plane is located at $X_{CAD} = -10\ cm$. Incident protons are given an energy of 800 MeV and an initial direction, $+X_{CAD}$, perpendicular to the source plane. The weight of each source proton is defined as N_p to normalize the distribution of sampled protons to the total number of protons delivered in the physical shot.

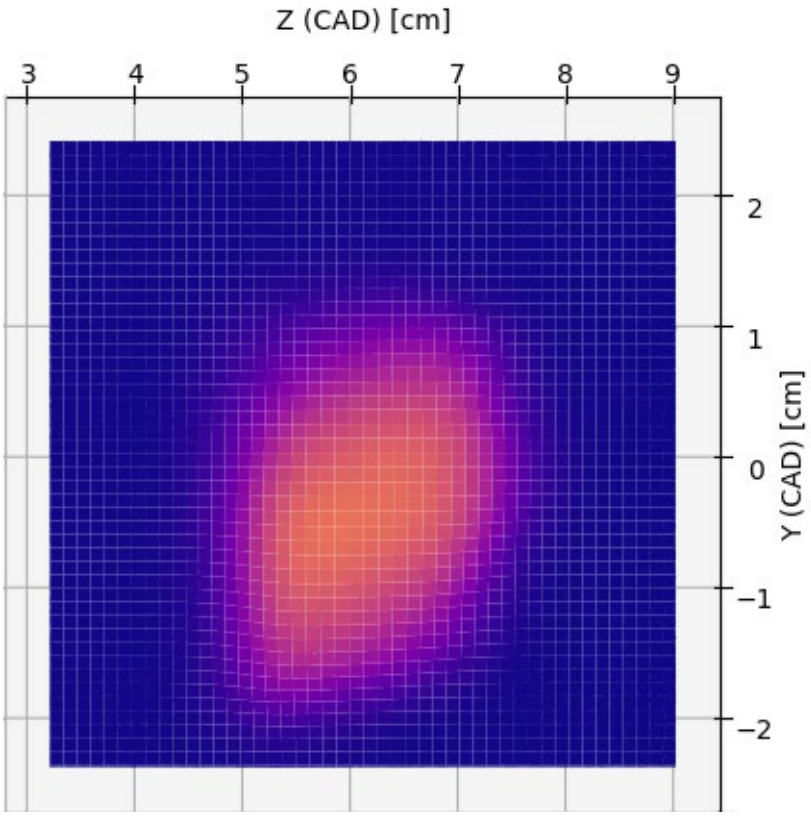

Figure 48: Example showing Shot#31 on block B3 after conversion to protons per pixel and conversion to the CAD coordinate system.

```
c - - - Begin Source Definition - - -
c
c This is a source definition template for the Second Target Station experiment
c models for the LANSCE beam line.
c
c Written by Wouter de Wet (dewetwc@ornl.gov) on 9/12/2022.
c
c The source is described as a planar mono-energetic histogram of protons
c that are born on the z-y plane moving in the +x direction.
c
c - - - - - - - - - - - - - - - - - - - - - - - - - - - - - - - - - - - - -
c | All protons are born at x = -10.0 cm
c |
c | Number of bins in z direction, n_z = 285
c | Number of bins in y direction, n_y = 241
c |
c | Minimum z value, min_z =        -9.2541660540 [cm]
c | Minimum y value, min_y =        -2.4682730741 [cm]
c |
c | Maximum z value, max_z =        -3.2201152895 [cm]
c | Maximum y value, max_y =         2.5230554534 [cm]
c |
c | Z bin width, dz =         0.0211721079 [cm]
c | Y bin width, dy =         0.0207109068 [cm]
c |
c | Center of middle target block located at z = 0.0 [cm], y = 0.0 [cm]
c |
c | Source Strength:      1.578262126e+13 [protons/pulse]
c - - - - - - - - - - - - - - - - - - - - - - - - - - - - - - - - - - - - -
sdef     pos=d001
         z=fpos d002  y=fpos d003  x=-10.0
         vec=1 0 0  dir=1
         par=h  erg=800.0  wgt=1.578262126e+13
c
c Distribution for sampling which position element from histogram.
si001 L
              -10.0     2.5127000    -9.2435800
              .
              . <data pattern>
              .
              -10.0    -2.4579176    -3.2307013
sp001
              1.0423767e-06
              .
              . <data pattern>
              .
              4.1091876e-07
c
c
c Distribution for linking selected pos to z-position distribution.
ds002 S
                      4
                     .
                     . <repeat 4 to 288 n_y times>
                     .
                     288
c
c Distribution for linking selected pos to y-position distribution.
ds003 S
                     289
                     .
                     . <repeat 289 n_z times then increment n_y times>
                     .
                     529
c
c
c Distributions 004 through <004+n_z> correspond to z-direction binning structures.
si004           -9.2541661  -9.2329939
sp004            0.000E+00   1.000E+00
.
. <data pattern>
.
si529           -2.4682731   -2.4475622
sp529            0.000E+00    1.000E+00
c
c - - - End Source Definition - - -
```

Figure 49: Example MCNP6 source definition input deck for one pulse.

4.2.2 Transport Methodology and Simulation Results

For each shot, a radiation transport analysis is performed using MCNP6.2® [23]. Tracked particles include protons, neutrons, photons, pions (positive, negative, and neutral), deuterons, tritons, helions, alpha particles, muons (positive and negative), kaons (positive, negative, long and short neutral). Material definitions for tungsten (19.3 g/cc), tantalum (16.6 g/cc), niobium (8.6 g/cc), and air (1.007 g/cc), have been taken from the STS material database. Cross-sections are used from ENDF7 [24]. If no cross-sections are available, event generator models are used for elastic and nuclear interactions. Energy deposition is tallied in the elemental edits of the unstructured mesh. The total energy deposition is calculated as the sum of the contribution of protons, neutrons, gammas, positive pions, deuterons, tritons, helions and alphas. The integrated mesh tally results correspond well (within 2%) with the results of the +F6 tallies that consider all particle contributions. More details can be found in the pre-experiment report [25], in which the same methodology is followed.

Figure 50 shows the unstructured mesh, generated with Attila4MC [26], that has been used for the neutronics calculations. The maximum edge length of the tetrahedral mesh elements is set to 2 mm in the first ≈7 cm of each block, and 5 mm in the rest of the geometry. This ensures sufficient resolution in the energy deposition profile at the location with the highest deposition, without the need for an excessive number of mesh elements. Each calculation is run with 5e7 particles, which takes ≈1 hour on 384 nodes (half of the Saturn cluster).

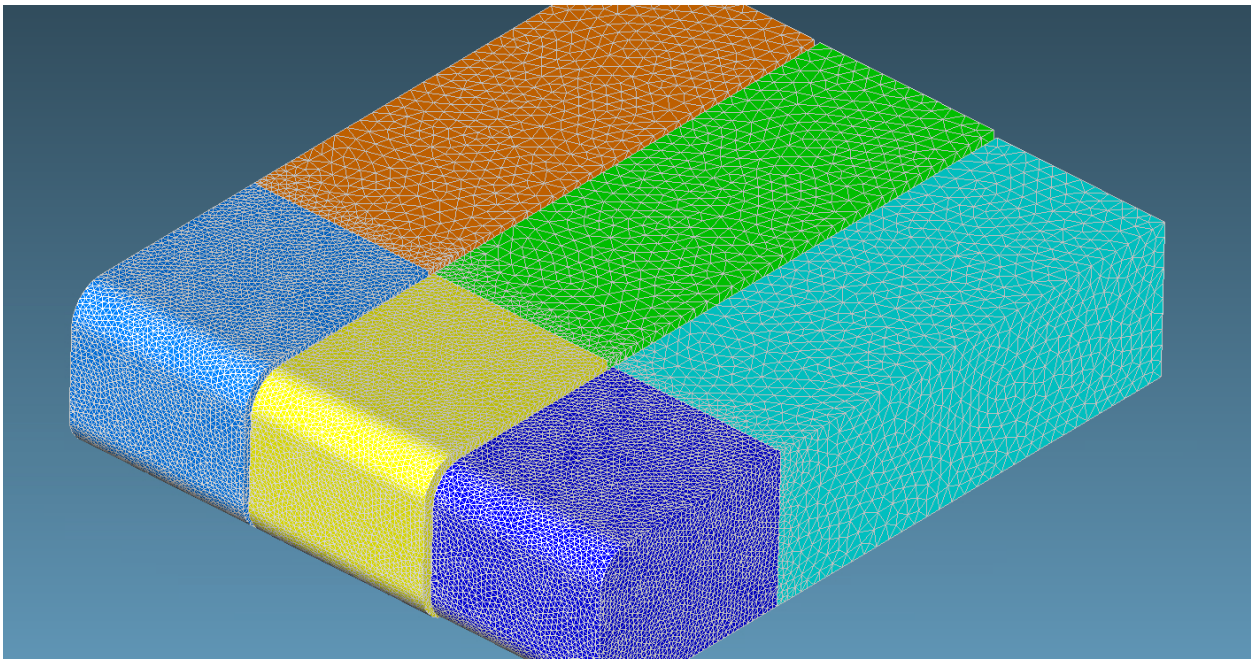

Figure 50: Unstructured mesh for neutronics calculations, generated using Attila4MC.

4.3 STRUCTURAL DYNAMICS

All scripts for the structural dynamics analysis are attached to this report in a folder named *Structural_Analysis_Scripts*.

4.3.1 Geometry

For beam shots on individual blocks, the structural dynamics simulation domain corresponds to that single block. Three separate solid model files were created from the CAD model shown in Figure 47 by deleting the other 2 blocks and saving as a ACIS ".sat" file. Figure 51 shows an example for block B1.

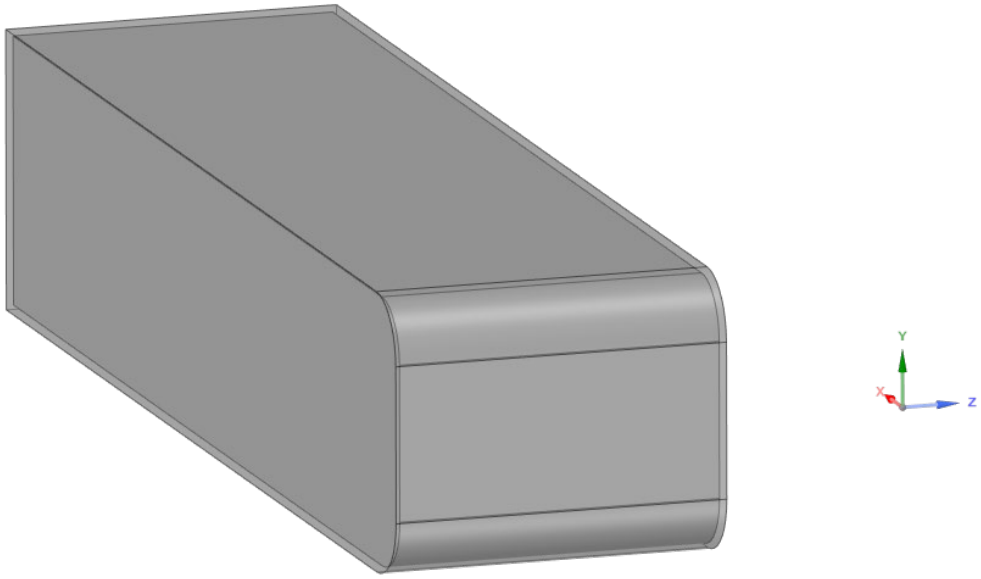

Figure 51: CAD geometry for Block B1 as used for structural dynamics simulations. The Nb cladding is shown as translucent. The global CS is also maintained as shown.

4.3.2 Discretization

The first step of the analysis creates a discretization of the target block geometry using CUBIT version 15.7 on the OZ3 linux cluster at SNS. A script file automates the mesh creation using the following steps:

- Imports CAD file in ACIS format
- Slices CAD solids using "webcuts" tools to help partition the volumes for meshing
- Imprints and merges the geometries to create a continuous mesh and to create a mesh with duplicate nodes between the block and any cladding
- Meshes the target block with hexahedral elements (Abaqus C3D8R equivalent) using a 1 [mm] nominal seed size
- Refines the cladding mesh to create 3 elements in the through-thickness direction
- Meshes the outermost surfaces with 4 node shell elements that share nodes with the hex elements
- Creates named selections

- Exports the final mesh in Exodus II format

Figure 52 shows the mesh used for Block 1. Table 3 lists the named selections that are exported with the mesh to be used for analysis. The purpose for the shell elements is to enable output of strains at the strain sensor locations. Without the shell elements, element strain outputs would only be available at the single element integration point at the centroid of each element. With the shell elements (defined with a nominal 0.1 [μm] thickness), the strains are effectively extrapolated to the surface.

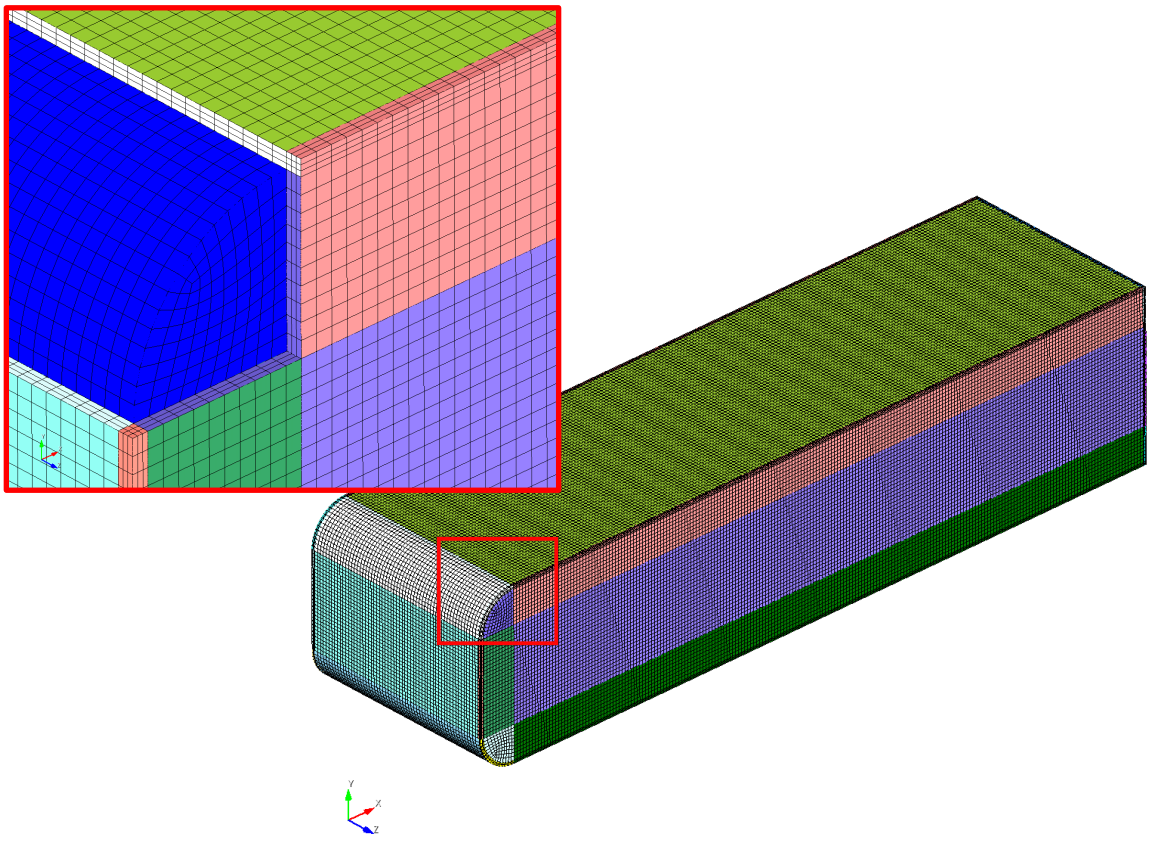

Figure 52: Discretization of Block 1 for structural analysis in CUBIT software. The figure inset removes a portion of the cladding to show the interior mesh. The coloring corresponds to volume slicing that enables good quality, automatic hexahedral element generation.

Table 3: Named selections used in discretization of Block 1 for structural analysis. The block and cladding have duplicate nodes at their interfaces. The cladding and cladding surface have shared nodes at their interfaces. There are 777,856 total elements and 859,355 total nodes.

Named Selection	Type	Count
BLOCK_INT	HEX8	612,016
CLAD	HEX8	165,840
CLAD_SURF	SHELL4	58,868
NS.BLOCK	Node	638,203
NS.CLAD	Node	221,152

4.3.3 Neutronics Heating Interpolation

Once the mesh is created for analysis, the neutronics heating data must be interpolated onto the mesh. This is performed with a custom Python script. The module constructs the neutronics heating point cloud as a tetrahedral mesh using the Delaunay triangularization method found in the pyTetGen module. Each node of the target block mesh is then located within a tetrahedron and is thus surrounded by 4 neutronic heating values. These are weighted by area using Barycentric interpolation. Any nodes external to the triangularization (due to coordinate rounding, for instance) are then extrapolated using a distance weighting of the 3 nearest neutronics heating neighbors via the scikit-learn module.

Neutronics provides a file for each part of the domain shown in Figure 47 using the following naming convention:

- *energy_deposition.mcnp_Nb1.txt* → Niobium cladding on block 1
- *energy_deposition.mcnp_Ta2.txt* → Tantalum cladding on block 2
- *energy_deposition.mcnp_W1.txt* → Tungsten block 1
- *energy_deposition.mcnp_W2.txt* → Tungsten block 2
- *energy_deposition.mcnp_W3.txt* → Tungsten block 3

Each file contains 6 columns of tabulated data consisting of:

- X-coordinate [cm]
- Y-coordinate [cm]
- Z-coordinate [cm]
- Energy Deposition [J/cm^3/pulse]
- RelativeError []
- Volume [cm^3]

The energy deposition is converted into a pulse temperature rise using the thermal capacitance ($\rho \cdot c_p$) of the metals and assuming that no appreciable thermal diffusion takes place in the timeframe of interest. Figure 53 shows an example pulse temperature rise for a beam pulse on a block.

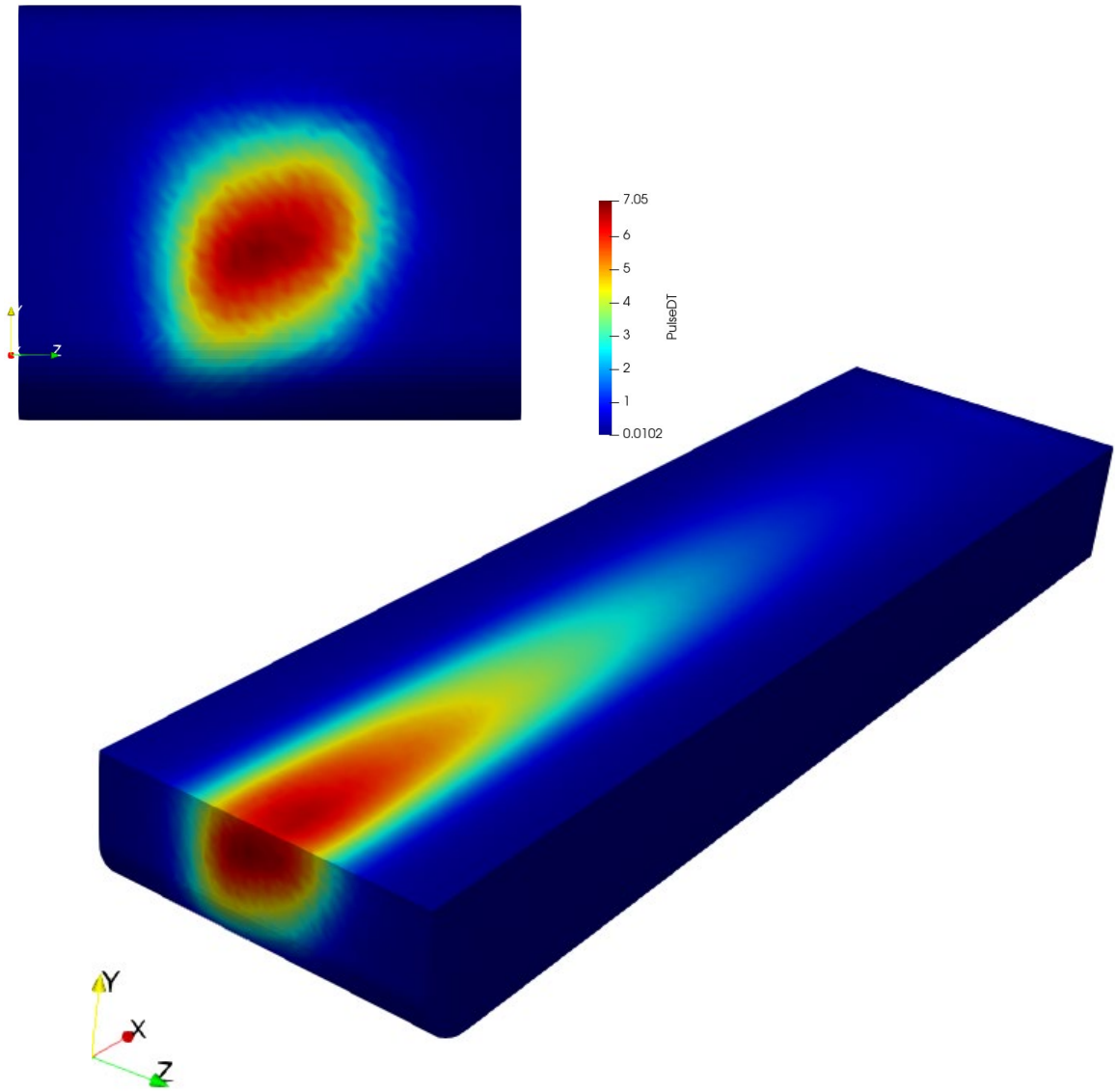

Figure 53: Example pulse temperature rise for Shot#31 on block B3. The field "PulseDT" is the instantaneous temperature rise [deg-C] determined from neutronics energy deposition and the thermal capacitance of the metal.

The assumption of negligible thermal diffusion can be verified by performing a transient heat conduction simulation using the energy deposition field directly. This was done for a pre-experiment Gaussian beam input. The energy deposition was applied over 600 [ns], and the simulation was run for a total of 30 [ms]. Figure 54 shows both the final temperature field and the difference between the final temperature field and the temperature field just after energy deposition. The final temperature field has an approximately 5 [°C] difference. The maximum difference caused by thermal diffusion is approximately 0.3 [°C] or 6%. Furthermore, the peak strains occur just after the beam pulse, when even less thermal diffusion has occurred.

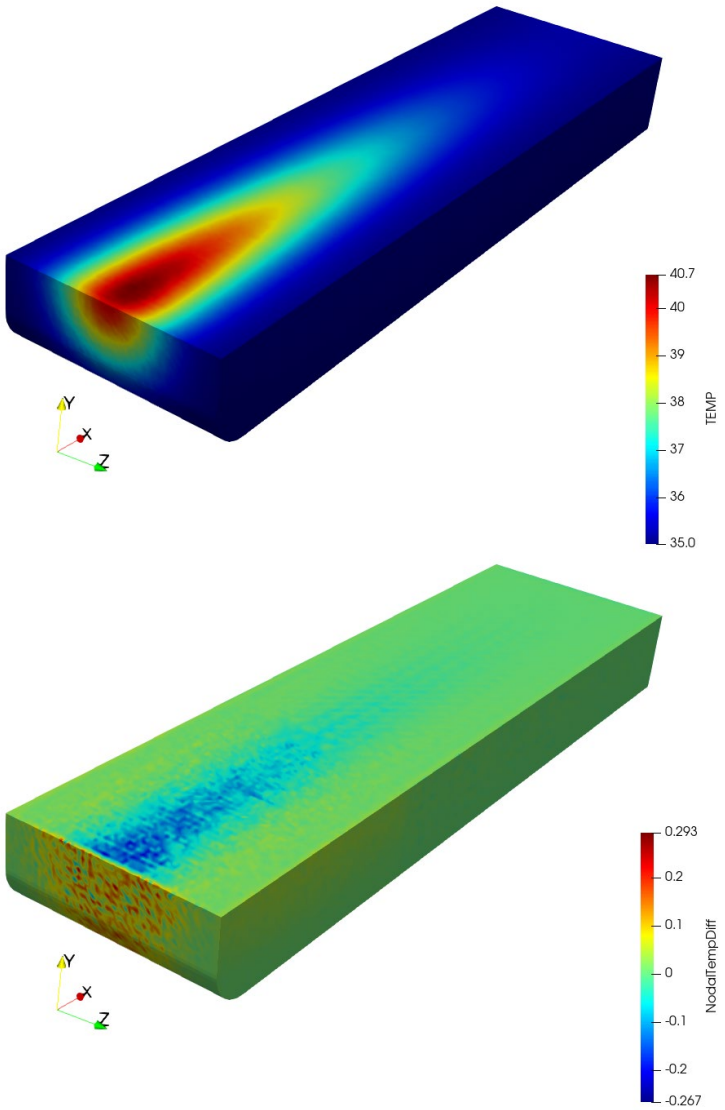

Figure 54: Verification of negligible thermal diffusion assumption. A 30 [ms] transient conduction simulation was performed using a pre-experiment Gaussian beam. The top image shows the final temperature field [°C]. The bottom image shows the temperature difference between final and just after energy deposition.

4.3.4 Structural Analysis

The automated target block analysis next performs a structural simulation using Sierra Presto. The domain is the single tungsten block with any associated cladding. Table 5, Table 6, and Table 7 list the relevant material properties and models. No boundary conditions are present. The only loads are applied as temperature fields. A Python script takes the neutronics pulse temperature rise fields and places them in the correct time order for the structural analysis as listed in Table 4.

Table 4: Temperature field loads defined for Sierra structural dynamics simulations.

Time [ms]	Event	B1 Temperature Field [°C]	B2 Temperature Field [°C]	B3 Temperature Field [°C]
0.0	HIP Lock-In	369	450	30
0.007	HIP Cooldown	30	30	30
0.01	Operational Warmup	30	30	30
0.0100003	Beam Pulse	30+PulseDT	30+PulseDT	30+PulseDT
0.035	Pulse Response	30+PulseDT	30+PulseDT	30+PulseDT

Table 5: Tungsten material properties.

Property	Value	Units
Density	19,250	kg/m^3
Coefficient of Thermal Expansion	4.5	με/°C
Constitutive Model	Elastic	–
Young's Modulus	398	GPa
Poisson's Ratio	0.28	–

Table 6: Tantalum material properties. Plastic deformation functions come from Johnson-Cook modeling as reported by Chen & Gray (1996).

Property	Value	Units
Density	16,600	kg/m^3
Coefficient of Thermal Expansion	6.3	με/°C
Constitutive Model	ThermoElastic-Plastic	–

Property	Value	Units
Young's Modulus	188	GPa
Poisson's Ratio	0.35	–
Hardening	Kinematic	–
Yield Stress	$204.0 * \left[1 - \left(\frac{T - 25.0}{2976.85 - 25.0}\right)^{0.4}\right]$	MPa
Hardening Function	$C * (340.0 + 750.0 * EQPS^{0.7})$	MPa

Table 7: Niobium material properties.

Property	Value	Units
Density	8,600	kg/m^3
Coefficient of Thermal Expansion	7.1	με/°C
Constitutive Model	Bilinear Elastic-Plastic	–
Young's Modulus	103	GPa
Poisson's Ratio	0.38	–
Hardening	Kinematic	–
Yield Stress	172.0	MPa
Hardening Modulus	1.0	GPa

There are 4 steps to the structural analysis. First, a quasistatic step is defined to simulate the HIP cooldown process by which the cladding locks with the target and plastically deforms. The tantalum lock-in temperature comes from published experiments and analyses by ISIS. As a first order approximation, the niobium lock-in temperature is scaled from the tantalum value according to the melting points of the two materials. The bare tungsten block has no cladding, and thus there is no elevated lock-in temperature. Second, a quasistatic step is defined to simulate warm-up to operational temperatures. For the LANSCE experiment, the pulse repetition rate and power levels are low enough to keep each block at room temperature. The time duration of both quasistatic analysis steps was determined through trial and error to

minimize kinetic energy effects. A more detailed document on the development of Sierra simulations for target analysis is documented elsewhere [27].

The third step is the beam pulse event. This is an explicit step that applies the beam pulse temperature rise in a linear ramp-up over 300 [ns]. Fourth and final, the target block is allowed to dynamically respond over 25 [ms] as the elastic stress waves propagate, reflect, and interfere throughout the domain.

4.3.5 Solution Output & Postprocessing

The strain gage placements are defined in the target block manufacturing drawings [S07030100-M8U-8800-A003-R00, S07030100-M8U-8800-A004-R01, S07030100-M8U-8800-A005-R00] and must be transformed into the CAD coordinate system (see Figure 47). The effective gage length of each sensor is 4 [mm]. The Sierra input file for each block simulation requests strain output at 5 locations along the strain gage, spaced 1 [mm] apart, as listed in Table 8. Sierra then locates the surface shell element that contains that geometric coordinate and outputs the strain at the corresponding shell element integration point. The 5 strain results are then averaged together at each timestep to arrive at an equivalent strain gage output for comparison with experiment.

Table 8: Coordinates for strain output in Sierra structural dynamic simulations. The coordinates are in the CAD coordinate system. There are 5 outputs for each sensor, spread along the 4 [mm] gage length. Sierra reports the strain at the nearest shell element integration point. These 5 outputs are then averaged together for comparisons against the strain sensor measurements.

Sensor Name	X-Coordinate(s)	Y-Coordinate(s)	Z-Coordinate(s)
StrainB1A	-1	-2, -1, 0, 1, 2	-62.315
StrainB1B	29	25	-60.315, -61.315, -62.315, -63.315, -64.315
StrainB1C	72	25	-60.315, -61.315, -62.315, -63.315, -64.315
StrainB1D	65, 66, 67, 68, 69	0	-32.155
StrainB1E	46	-2, -1, 0, 1, 2	-92.465
StrainB2F	-1	-2, -1, 0, 1, 2	0
StrainB2G	29	25	-2, -1, 0, 1, 2
StrainB2H	72	25	-2, -1, 0, 1, 2
StrainB2I	65, 66, 67, 68, 69	0	30.155
StrainB2J	46	-2, -1, 0, 1, 2	-30.155
StrainB3K	0	-2, -1, 0, 1, 2	61.305
StrainB3L	29	24	59.305, 60.305, 61.305, 62.305, 63.305
StrainB3M	72	24	59.305, 60.305, 61.305, 62.305, 63.305

Sensor Name	X-Coordinate(s)	Y-Coordinate(s)	Z-Coordinate(s)
StrainB3N	65, 66, 67, 68, 69	0	90.465
StrainB3O	46	-2, -1, 0, 1, 2	32.165

5. RESULTS

5.1 PRE-EXPERIMENT STRUCTURAL DYNAMIC SIMULATIONS

Figure 56 shows the pre-experiment, Gaussian, beam pulse predictions after conversion to an instantaneous temperature rise and interpolation onto the structural dynamics mesh. The peak instantaneous temperature rise is approximately 5.6 [°C]. This then induces thermal expansion, causing a compressive stress in the core of each block that generates elastic stress waves that propagate and reflect throughout the blocks.

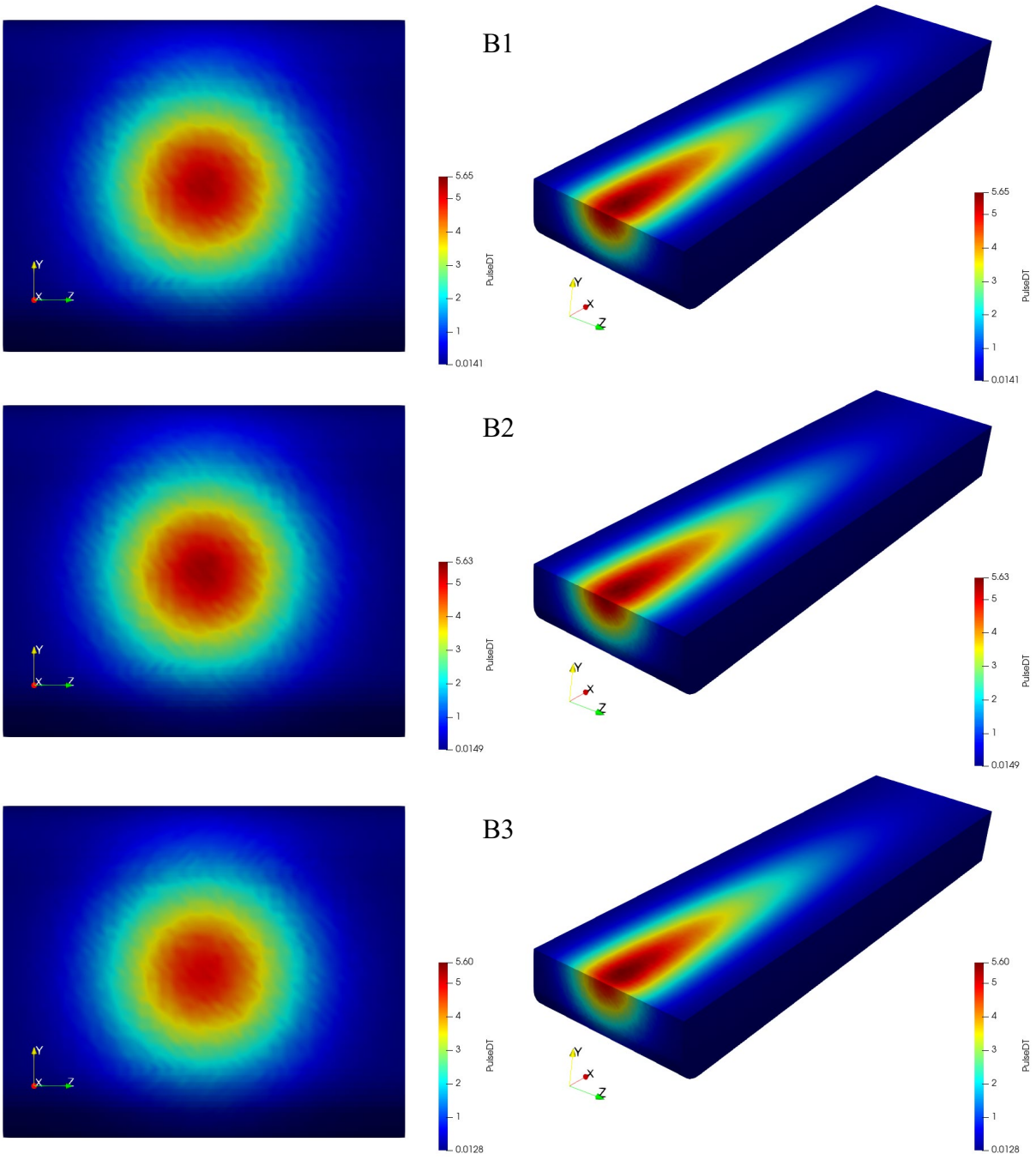

Figure 56: Pre-experiment predictions for instantaneous pulse temperature rise [°C] on each target block.

Figure 57 and Figure 58 show the results of a convergence study for both the spatial mesh size and timestep output. (Note that the solution timestep is automatically calculated for the stability of the explicit simulation.) For each strain sensor location, the maximum and minimum strain output was recorded, and the change relative to the finest discretization result was tracked. A nominal mesh size of 1 [mm] and time step output period of 0.6 [µs] was chosen as it results in less than 5% relative error for most sensors. The two biggest exceptions are the minimum strain

output for sensors B3_M and B3_N. With this mesh size, each simulation takes 5 [hours] on the OZ3 cluster using 12 compute nodes in the fast queue. It is felt that this is an acceptable trade-off.

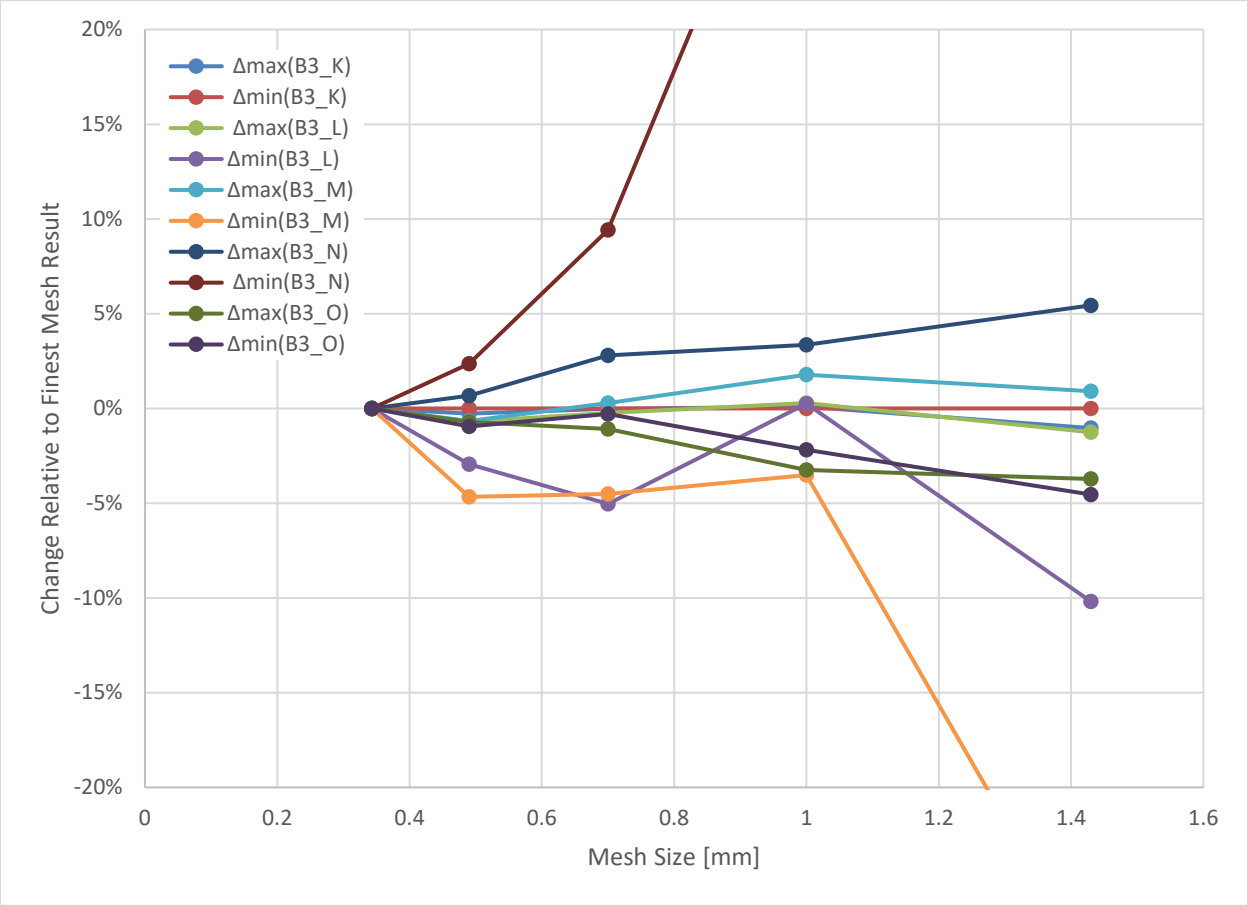

Figure 57: Mesh discretization convergence study. LANSCE pre-experiment Block B3.

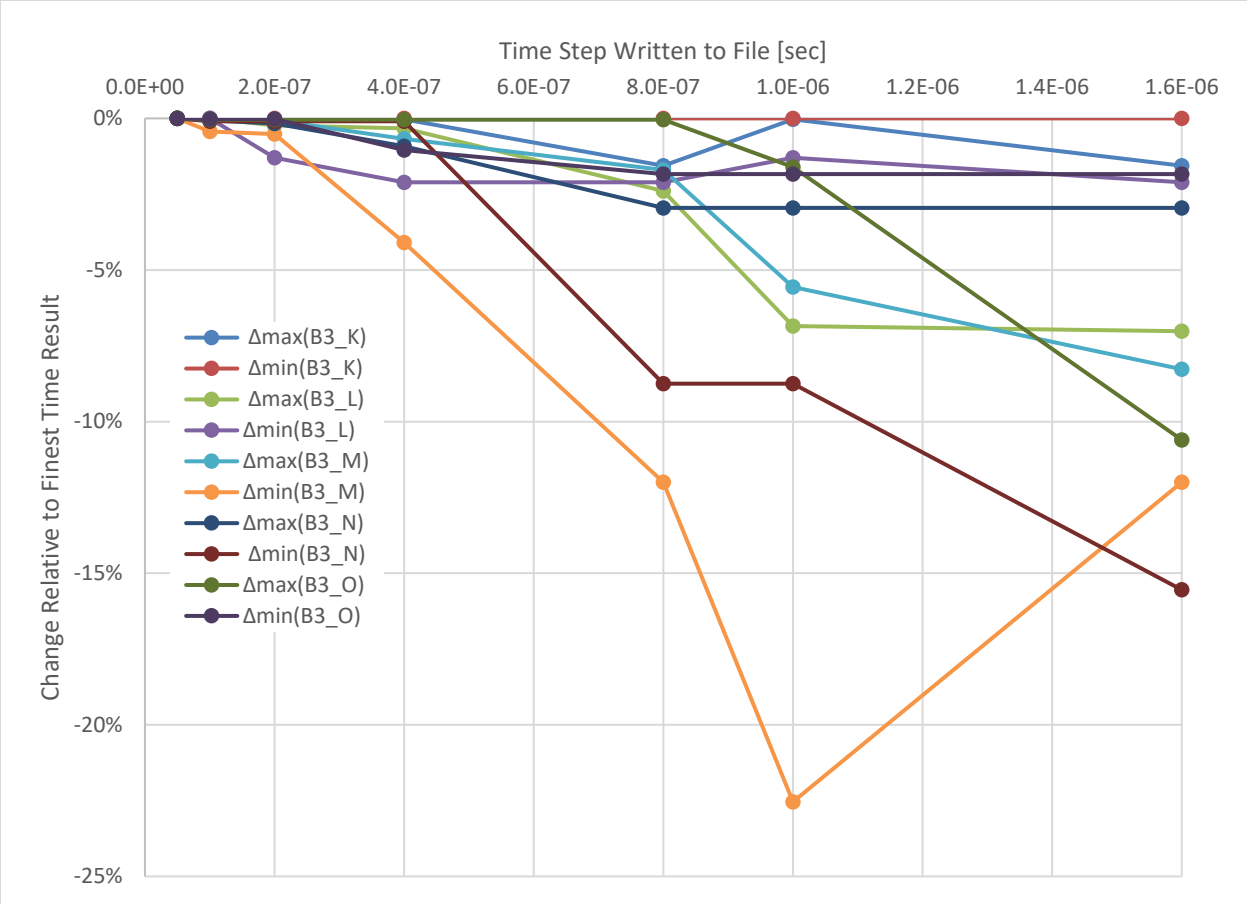

Figure 58: Timestep output convergence study. LANSCE pre-experiment Block B3.

The strain responses between blocks can be compared directly for the pre-experiment since each block receives an identical beam pulse. Figure 59 shows the strain response for each of the 15 strain sensors over the full 25 [ms] simulation duration. At this level, the strain responses between blocks look similar. There is obvious damping over the course of the simulation. Like Abaqus, Sierra applies a default amount of element damping (linear_bulk_viscosity=0.06; quadratic_bulk_viscosity=1.20) to achieve numerical stability (see p. 363 in [28]). Figure 60 compares the frequency content of sensors C, H, and M between the 3 blocks. It is interesting to note that the presence of cladding does not appear to change the frequency content but does shift it slightly. Also, the frequency content of the strain response occurs at frequencies below 200 [kHz]. Figure 62, Figure 63, and Figure 64 show comparisons between blocks in the time domain at the beginning of the pulses.

Figure 61 compares the running average strain response of each sensor. Block B2 has the highest average strain for each sensor followed by block B1 and then block B3. This is reasonable since B3 is the bare tungsten block and thus has the smallest total volume and smallest total energy deposition. Block B2 has the additional tantalum cladding and thus, additional energy deposition. Block B1 has the additional niobium cladding which is lower in density than tantalum and is thus expected to have less relative energy deposition. The only

sensors that do not follow this trend are B3-N and B1-D. Figure 64 compares the early time response of these sensors and does not show any anomalous features. This strain sensor does experience the smallest magnitude strain response, however, which might indicate the limit of numerical errors.

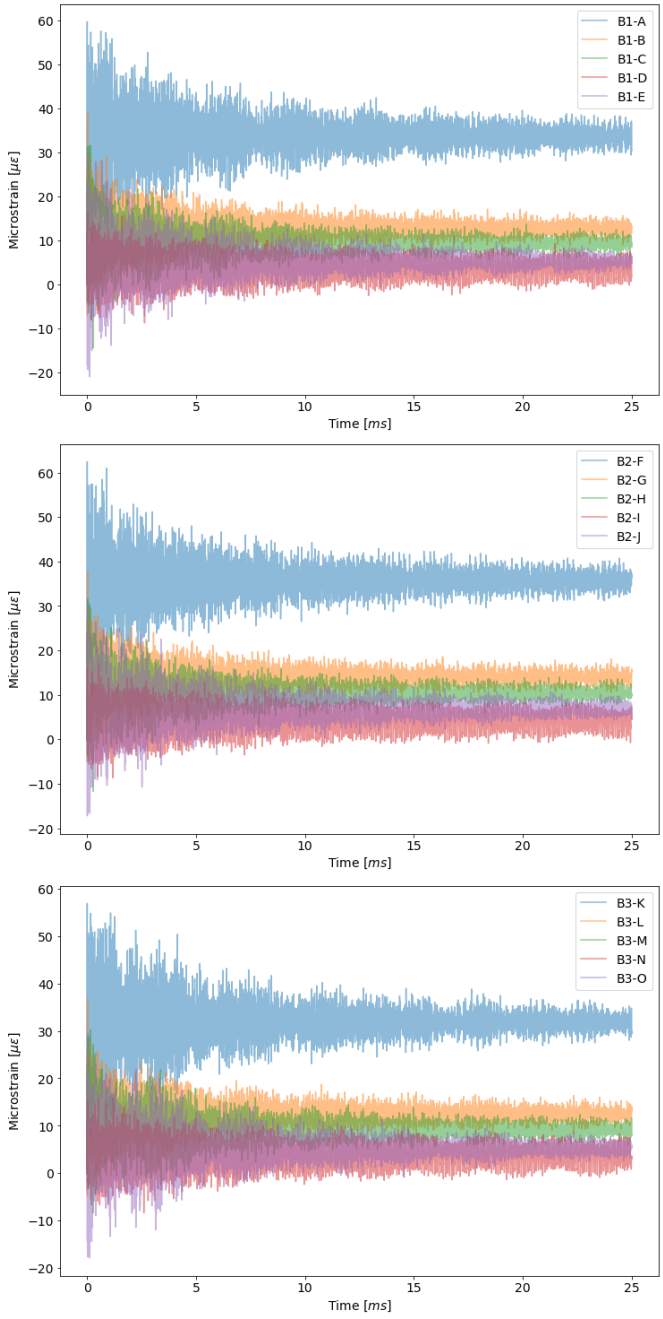

Figure 59: Pre-experiment strain sensor predictions for equal beam pulses on each block.

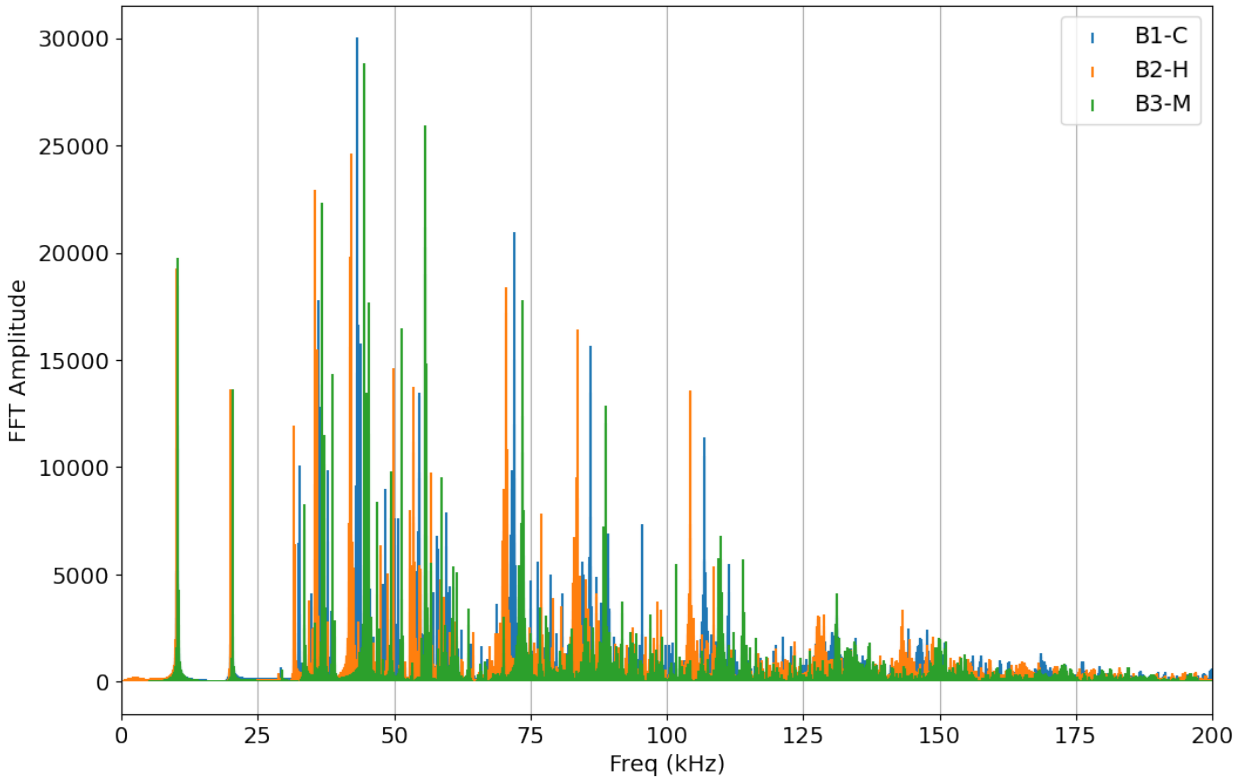

Figure 60: Pre-experiment strain sensor predictions for equal beam pulses on each block. Frequency content comparisons between sensors C, H, and M. All 3 blocks have the same frequency response, however, the presence of cladding causes a shift in frequency peaks. Signal content is below 200 [kHz].

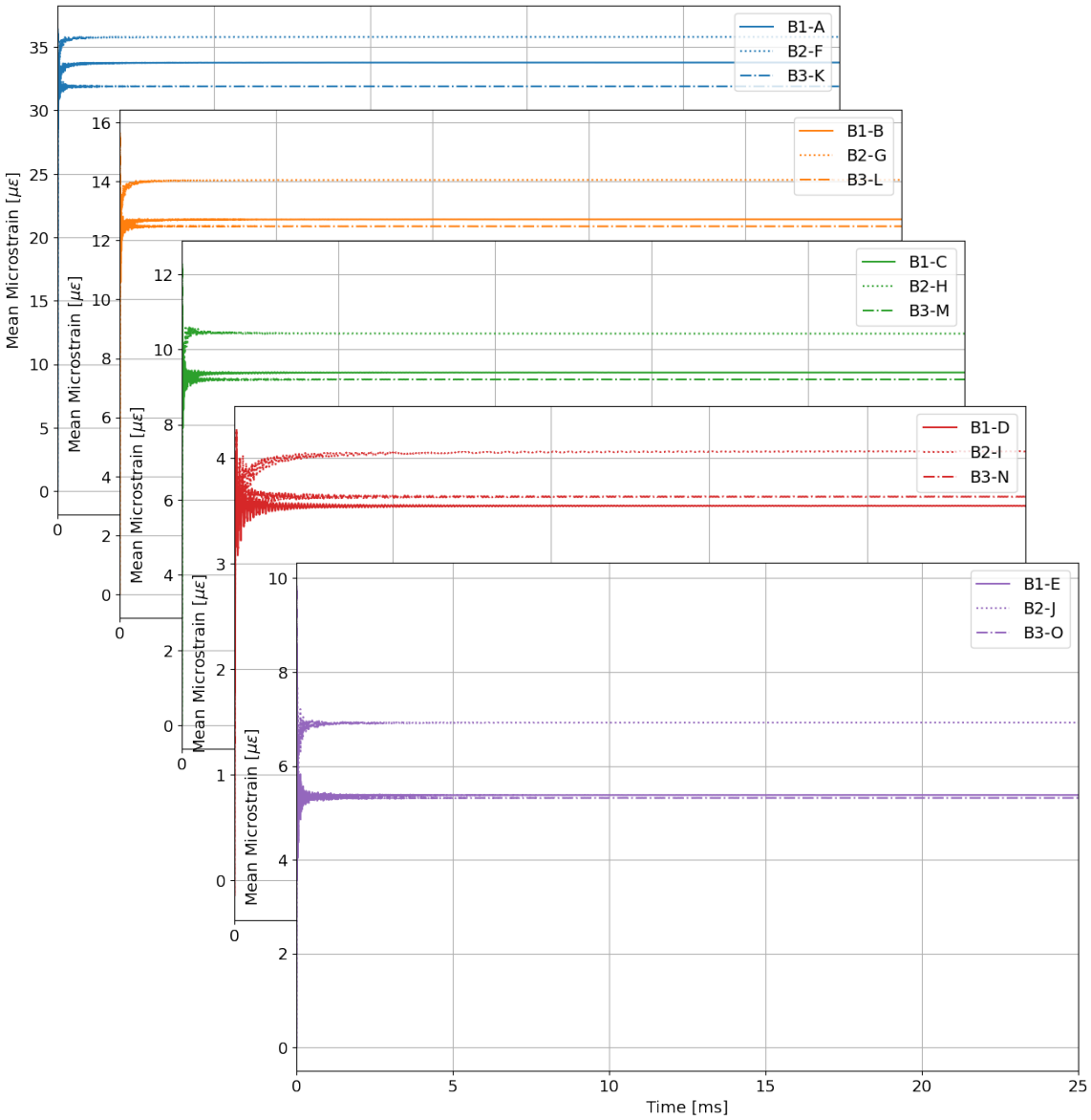

Figure 61: Pre-experiment strain sensor predictions for equal beam pulses on each block. Running average comparisons between all sensors across the 3 blocks. Block 2 experiences the highest strains corresponding with energy deposition in the additional tantalum cladding.

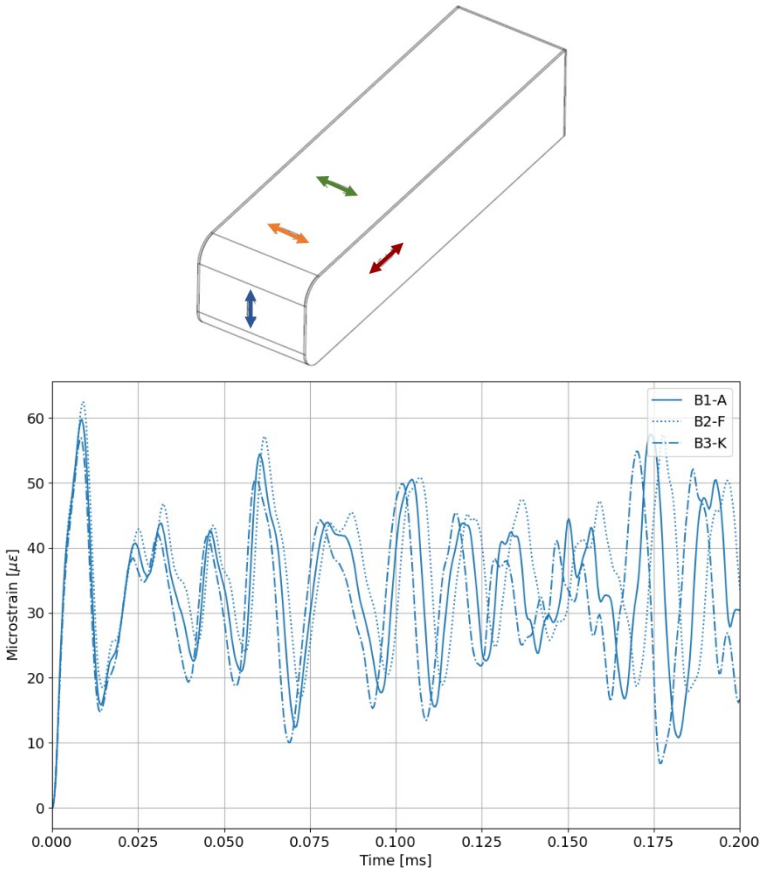

Figure 62: Pre-experiment strain sensor predictions at beam center location for equal beam pulses on each block.

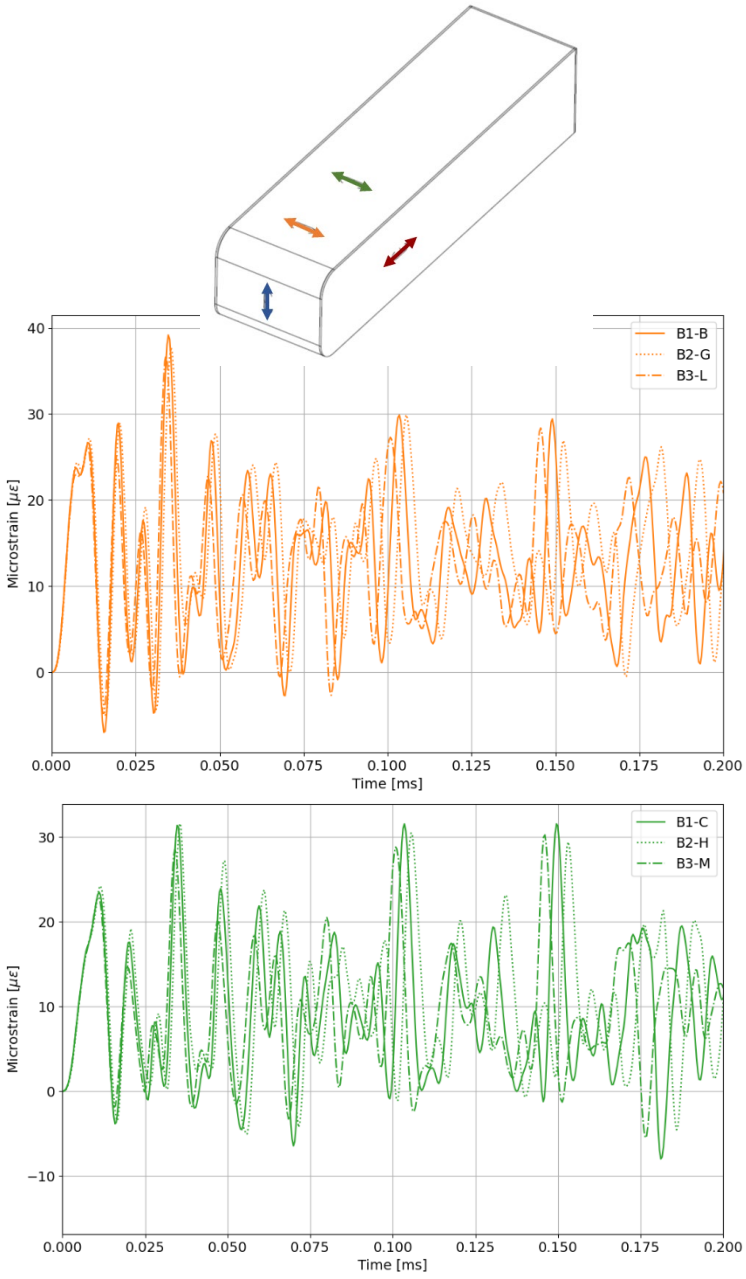

Figure 63: Pre-experiment strain sensor predictions along the top surface for equal beam pulses on each block.

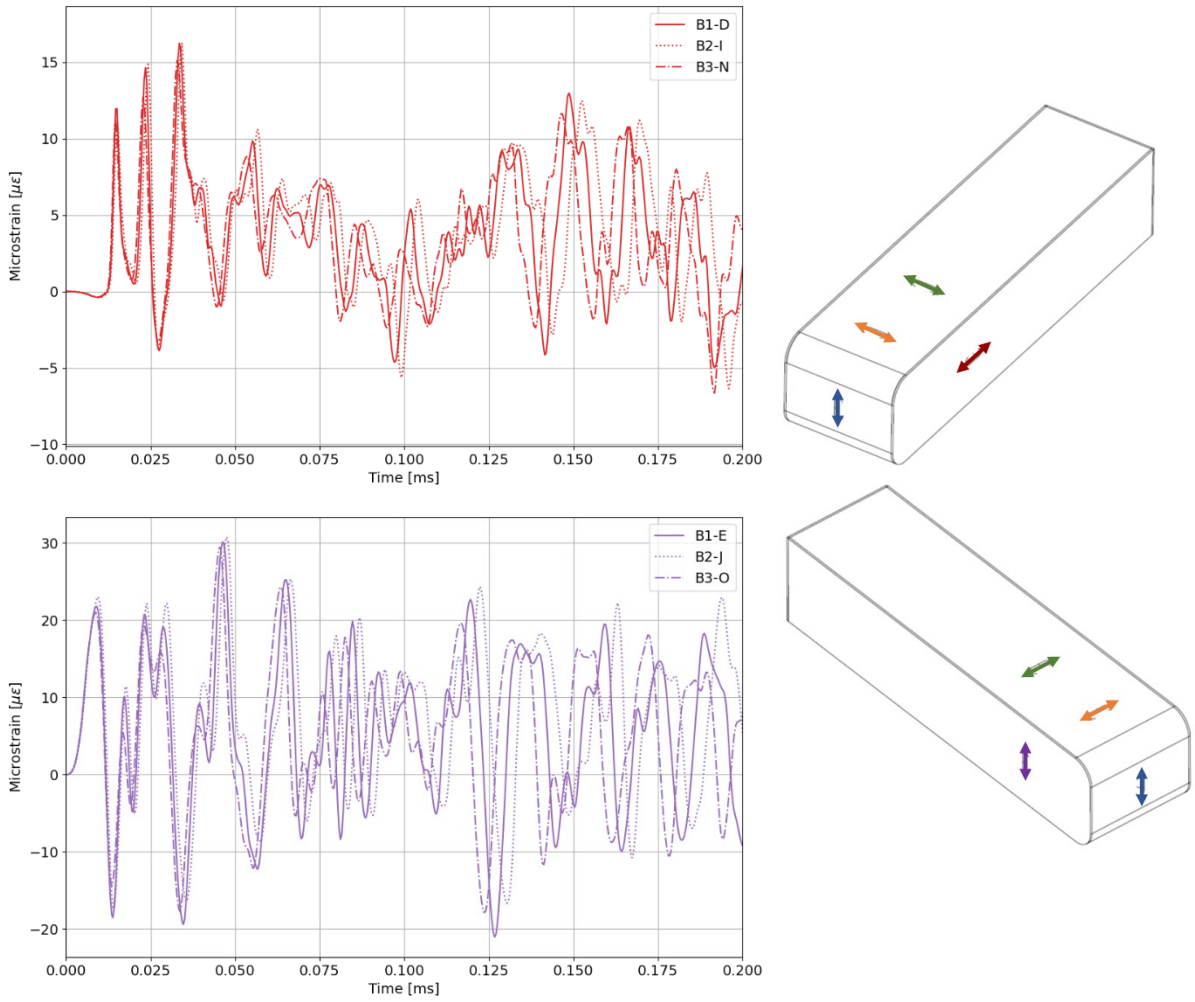

Figure 64: Pre-experiment strain sensor predictions along side surfaces for equal beam pulses on each block.

5.2 BEAM CURRENT, POSITION, AND INTENSITY RESULTS

5.2.1 Summary Results

The LANSCE accelerator and proton storage ring experienced operational difficulties that affected beam power, shape, and location. In informal conversations, the ORNL team learned that the control room normally would have 20 days commissioning time for the accelerator and proton storage ring. In this case, they had 2 days due to scheduling constraints. In addition, it had been 2 years since this kind of beam extraction to the blue room had last occurred. As a result, much of the pre-experiment plan had to be revised (see "MASTER_LOG.pdf"), and the ORNL team took the best beam conditions that could be provided. Figure 65 summarizes the beam shots that occurred in their time series. Figure 66 and Figure 67 compare the beam charge and peak intensity of these beam shots. The first set of beam pulses occurred between roughly 1-3am Eastern on August 27. About 46 shots were recorded with roughly equal placement on the centers of blocks B1, B2, and B3. A 12 hour break then occurred while the control room

attempted to adjust the beam for higher charge. Results showed marginal improvement. After receiving another ~45 beam shots, the ORNL team measured a series of beam shots with placement between the target blocks. Data collection ended shortly after 6pm Eastern, and LANSCE was unable to re-establish beam.

Figure 68, Figure 69, and Figure 70 show normalized images of the beam shots recorded for each block. The variability in charge, shape, and placement is evident.

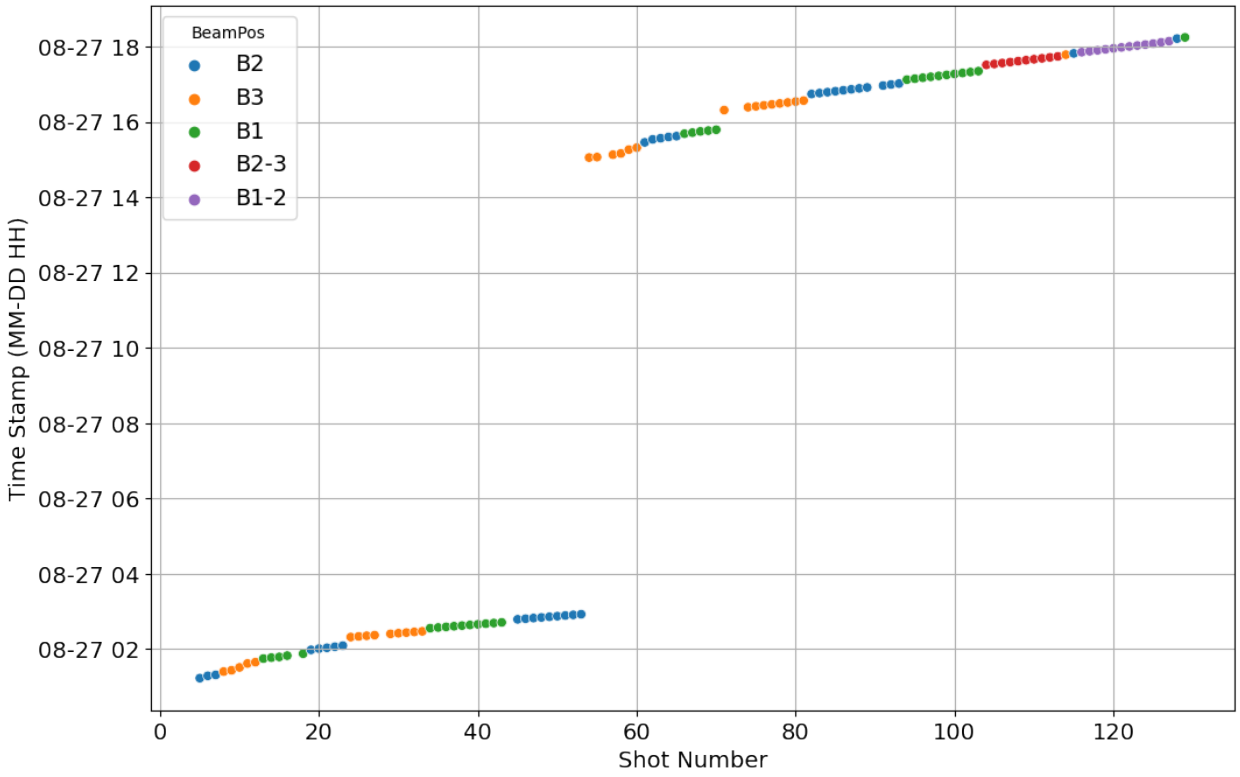

Figure 65: LANSCE experiment beam shot time series.

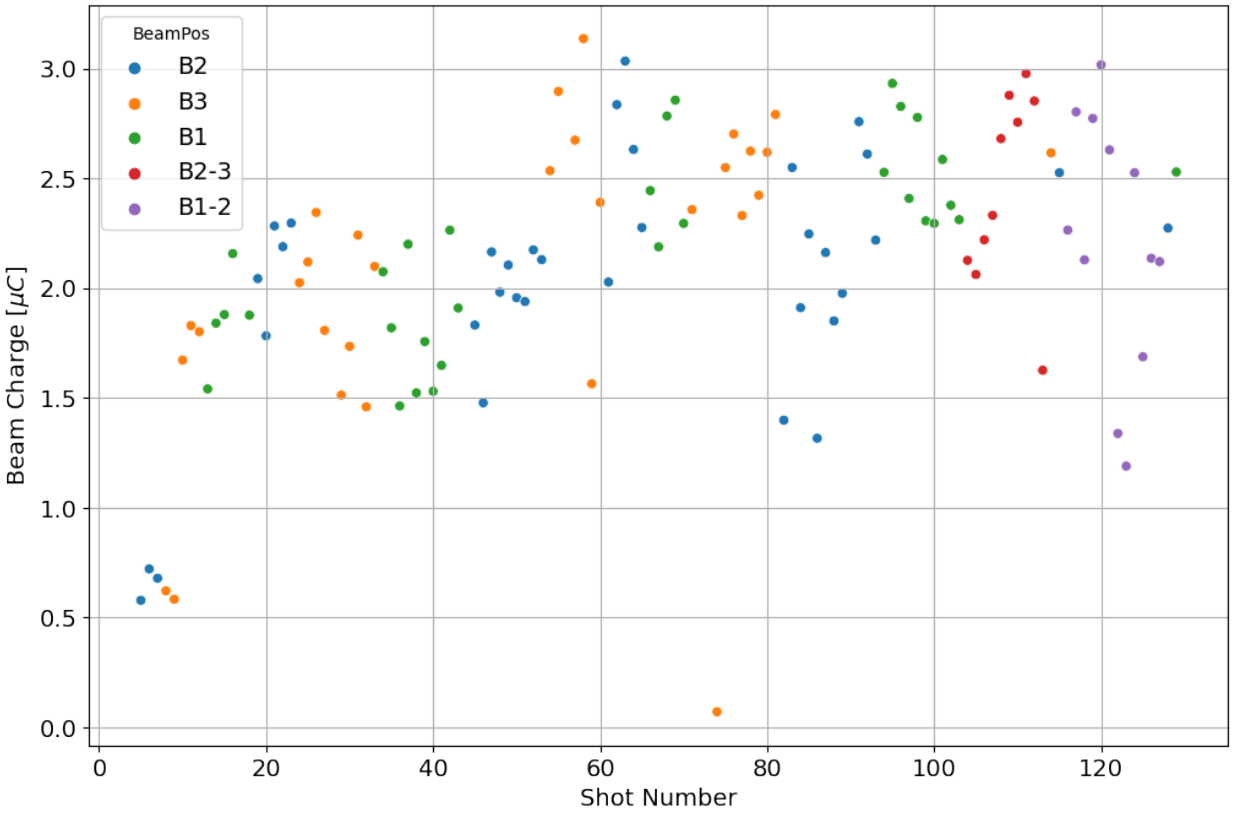

Figure 66: LANSCE experiment beam charge variation.

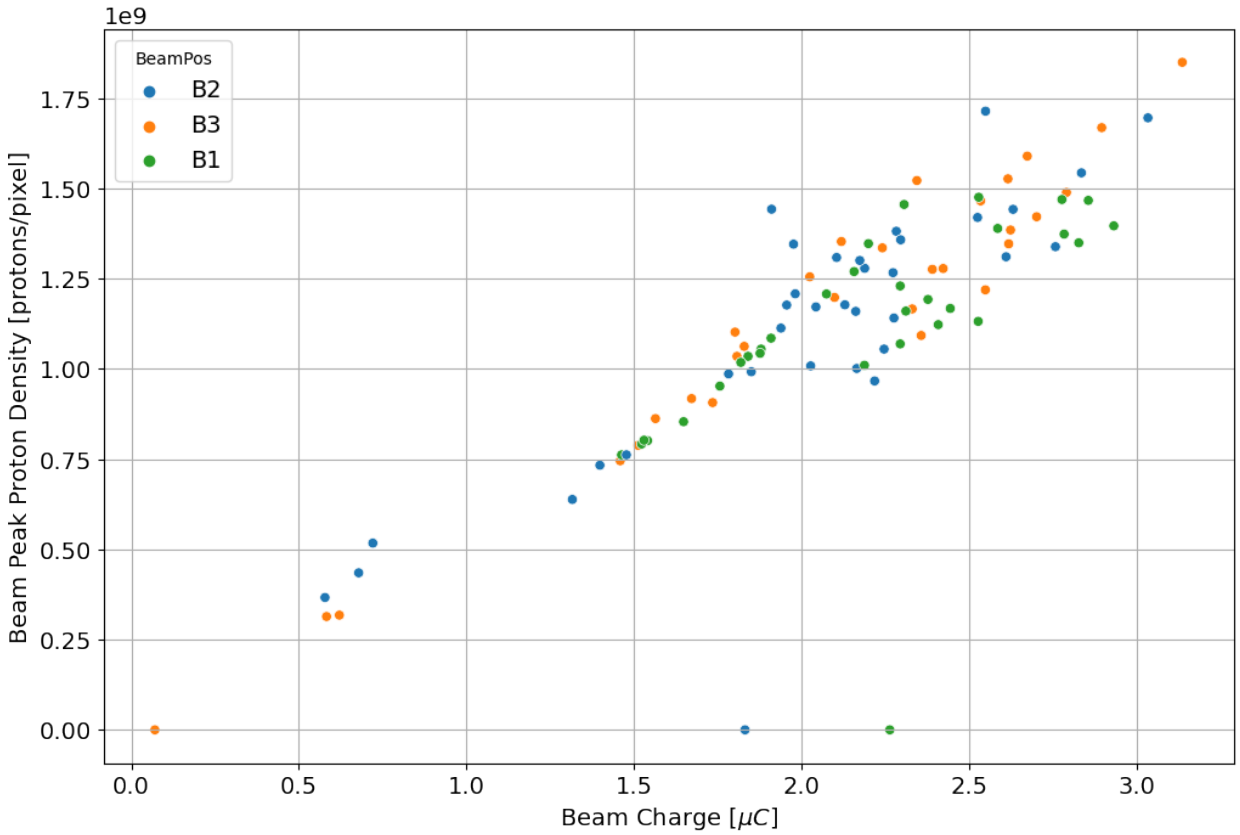

Figure 67: LANSCE experiment beam peak proton density variation with beam charge showing increased scatter above 2 [μC] beam charge. (The 3 data points with zero peak density were shots for which no radhard camera image was available.)

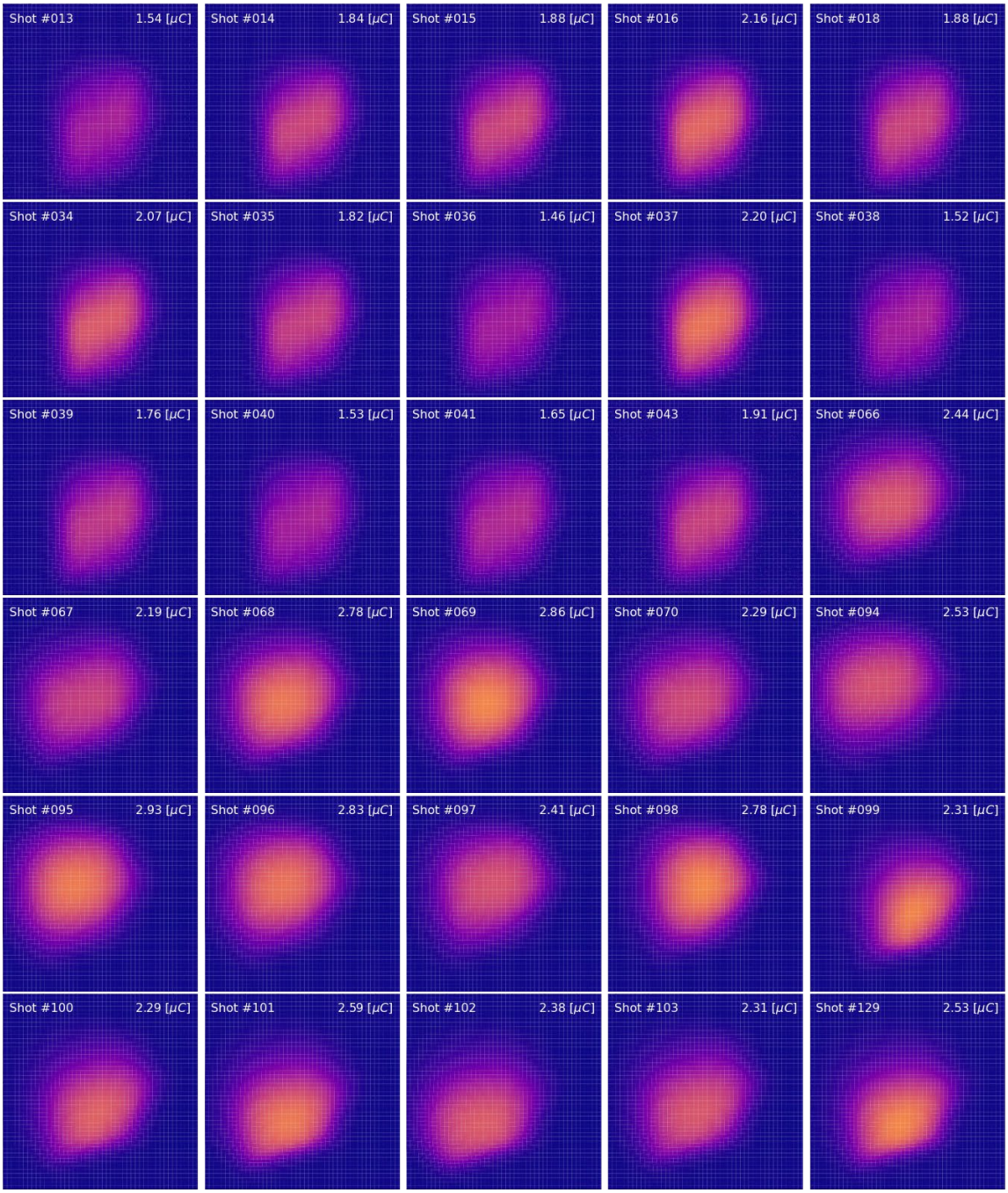

Figure 68: LANSCE experiment beam shot images for block B1. The image aspect ratios are not to scale. Color intensity has been normalized to scale with proton density.

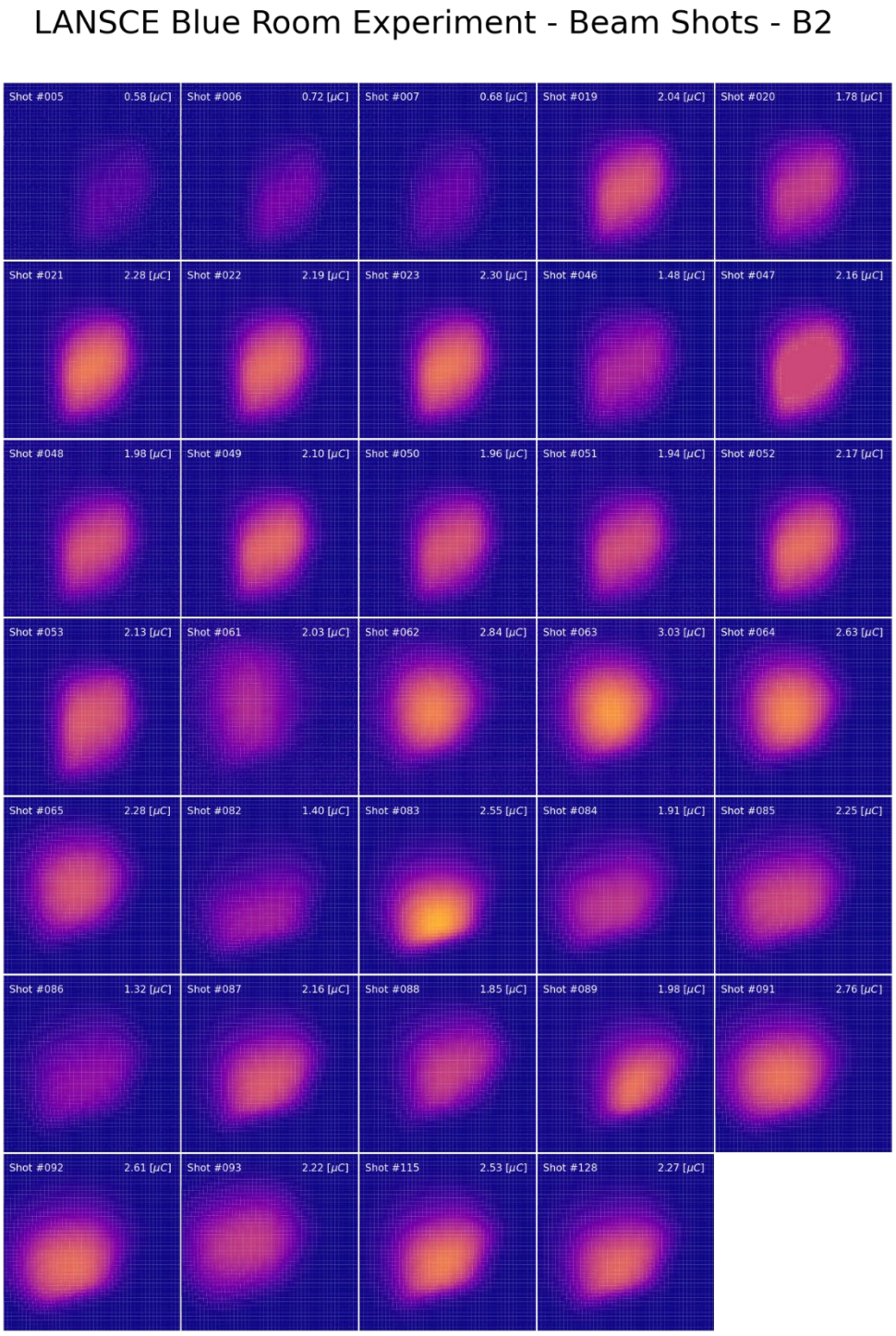

Figure 69: LANSCE experiment beam shot images for block B2. The image aspect ratios are not to scale. Color intensity has been normalized to scale with proton density.

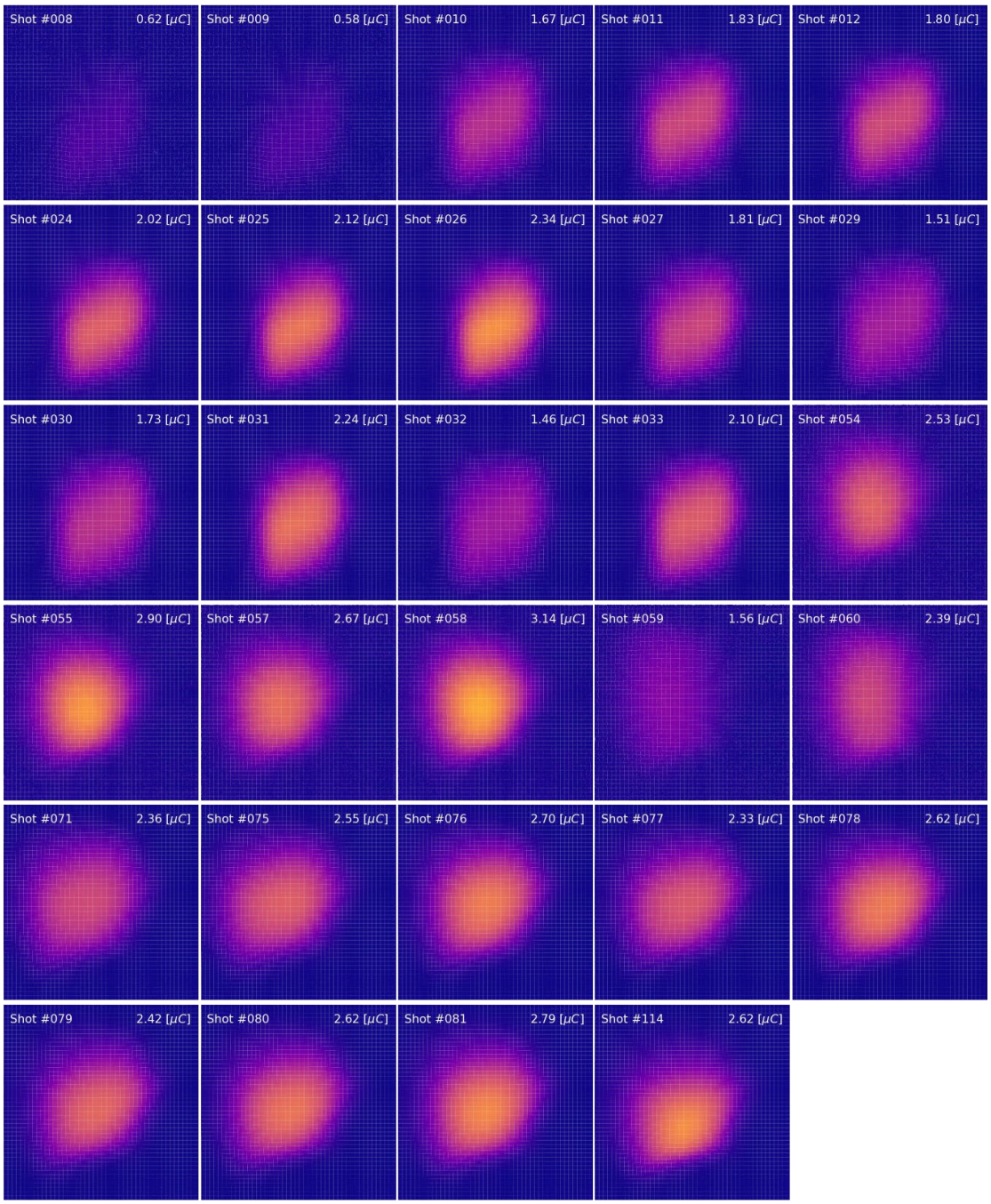

Figure 70: LANSCE experiment beam shot images for block B3. The image aspect ratios are not to scale. Color intensity has been normalized to scale with proton density.

5.3 COMPARISON OF STRAIN MEASUREMENTS AND SIMULATION PREDICTIONS

5.3.1 Centered Beam Pulses

5.3.1.1 Error Plots and Error Quantification

Figure 72 compares the experimental strain measurements against the finite element analysis (FEA) predictions. Three rows of plots are provided for centered beam pulses on B1, B2, and B3. For each block, three comparison plots are provided based on peak strain, mean strain, and peak strain amplitude (using the ASTM rainflow algorithm). The sensor locations and directions are color-coded as shown in Figure 71, and the size of each data marker is proportional to the beam charge of the shot.

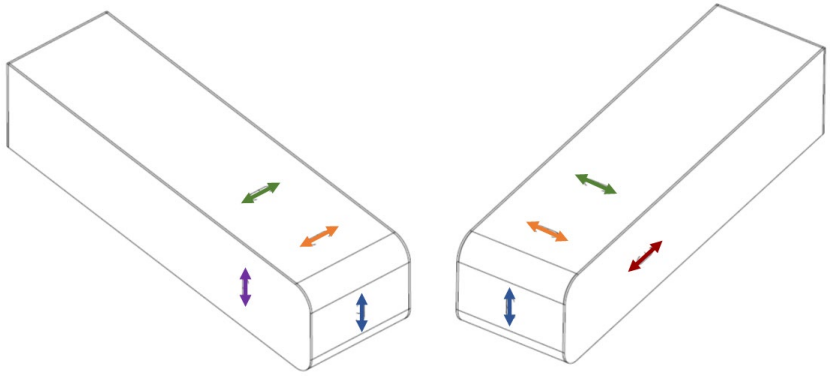

Figure 71: Color-coding for strain sensor location and direction.

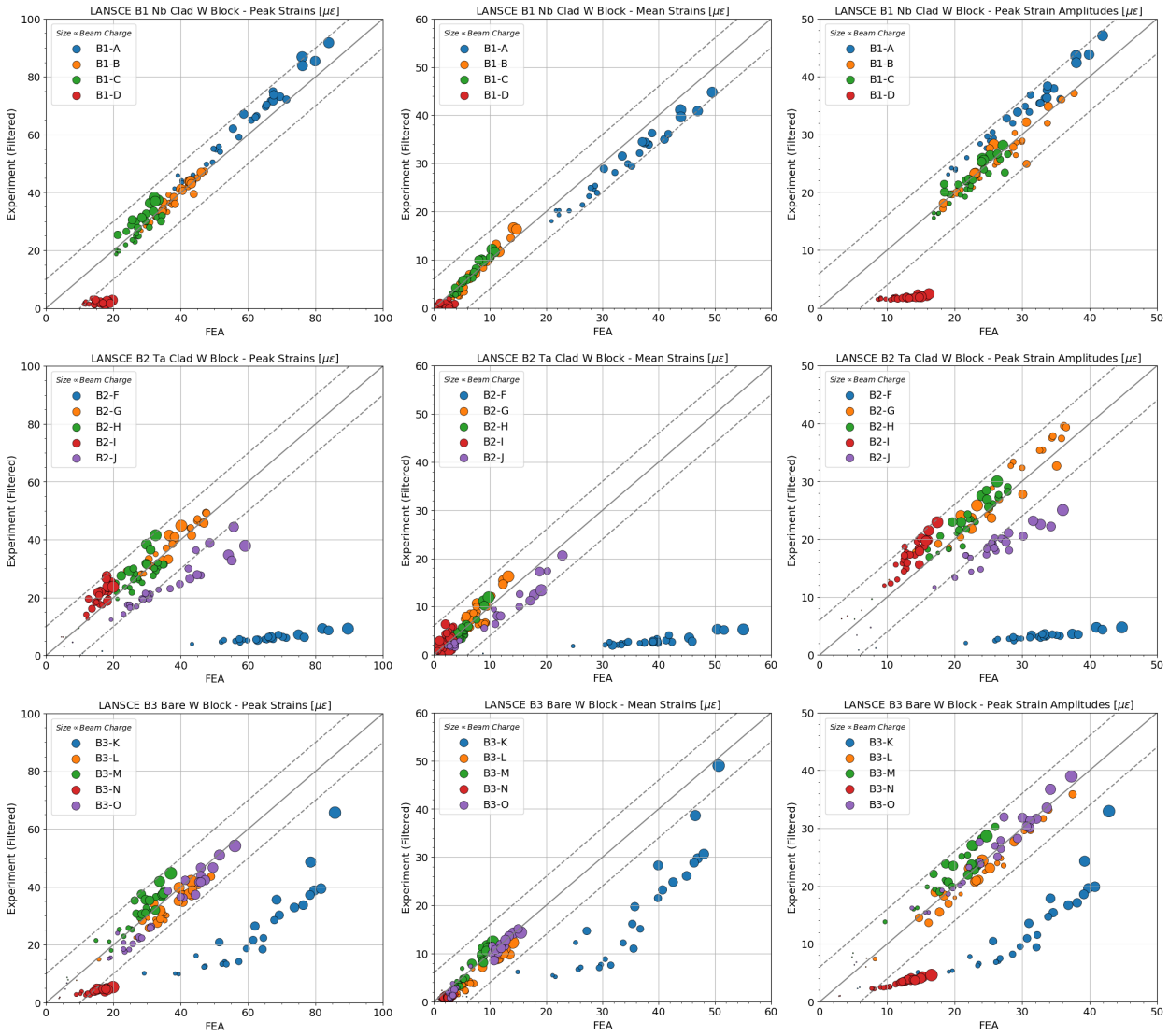

Figure 72: Comparisons between experimental strain measurements and FEA simulation predictions. Plots are provided for beam pulses centered on each block and for peak strains, mean strains, and peak strain amplitudes. Sensors are color-coded and marker size is proportional to beam charge.

In general, excellent agreement occurs with data scatter falling within a constant ±10 [με] for peak strains and ±6 [με] for mean strains and strain amplitudes. The error does not appear to be proportional to strain magnitude or beam charge. For the largest beam charge pulses (~ 3 [μC]), the relative error then approaches ±10%. The STS target is expected to receive pulses with beam charges near 36 [μC]. If these trends extrapolate, then relative errors in strain predictions would be closer to ±1%.

5.3.1.2 Broken Sensors and Sensor Debonding

Table 9 lists the strain sensors that were broken or debonded. Sensor B1-E was clearly broken in the fiber optic cable, and the measurement channel recorded noise. The other 5 sensors are suspected of being partially debonded by various amounts. These sensors are included in Figure 72 but have significantly lower experimental strain values compared to the simulation

predictions. They also, interestingly, continue to show a linear trend with beam charge. The SNS Mercury Target 30 previously attempted to place several unbonded sensors to explore temperature effects. Instead, the epoxy wicked down the sensor and caused partial bonding to occur. Figure 73 shows photographs of sensors AB, AC, and AD with epoxy partially along the sensor head. Figure 74 compares strain measurements against simulations. It appears that partial bonding still allows the sensor to measure the strain signal but at a reduced magnitude. The same effect is suspected to have occurred for sensors B1-D, B2-F, B2-J, B3-K, and B3-N in the LANSCE blue room experiment. PIE activities will be planned for confirmation.

Table 9: Strain sensors suspected of being broken or debonded.

Strain Sensor	Broken ?	Debonded ?
B1-D		X
B1-E	X	
B2-F		X
B2-J		X
B3-K		X
B3-N		X

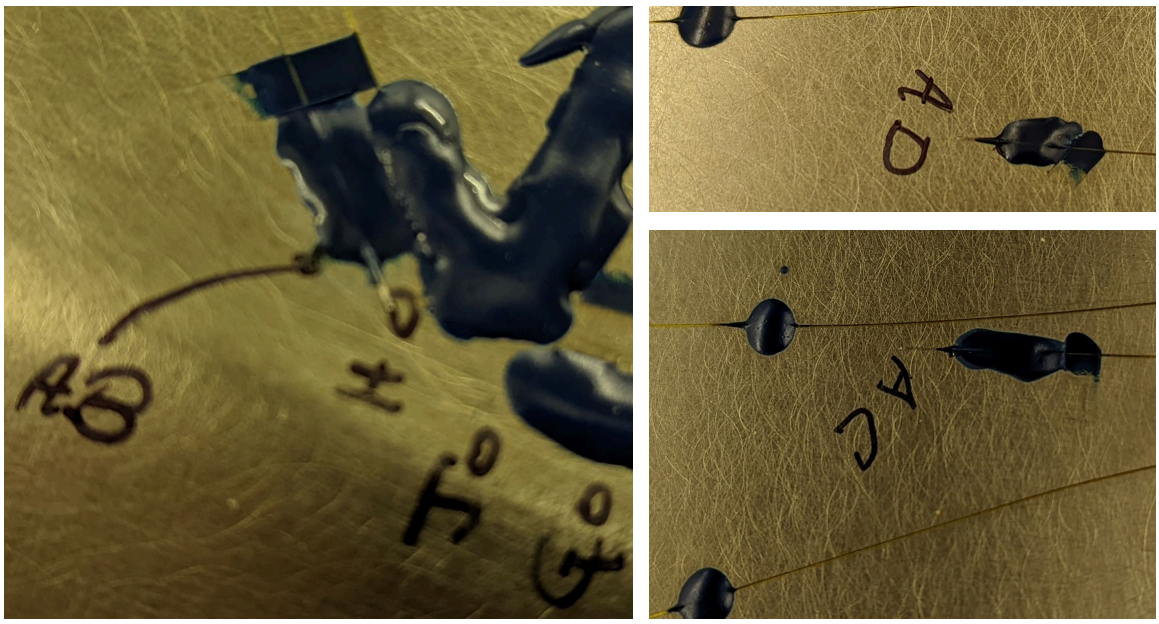

Figure 73: Photographs of SNS Mercury Target 30 strain sensors AB, AC, and AD showing partial sensor bonding due to capillary action causing the epoxy to wick along the sensor head.

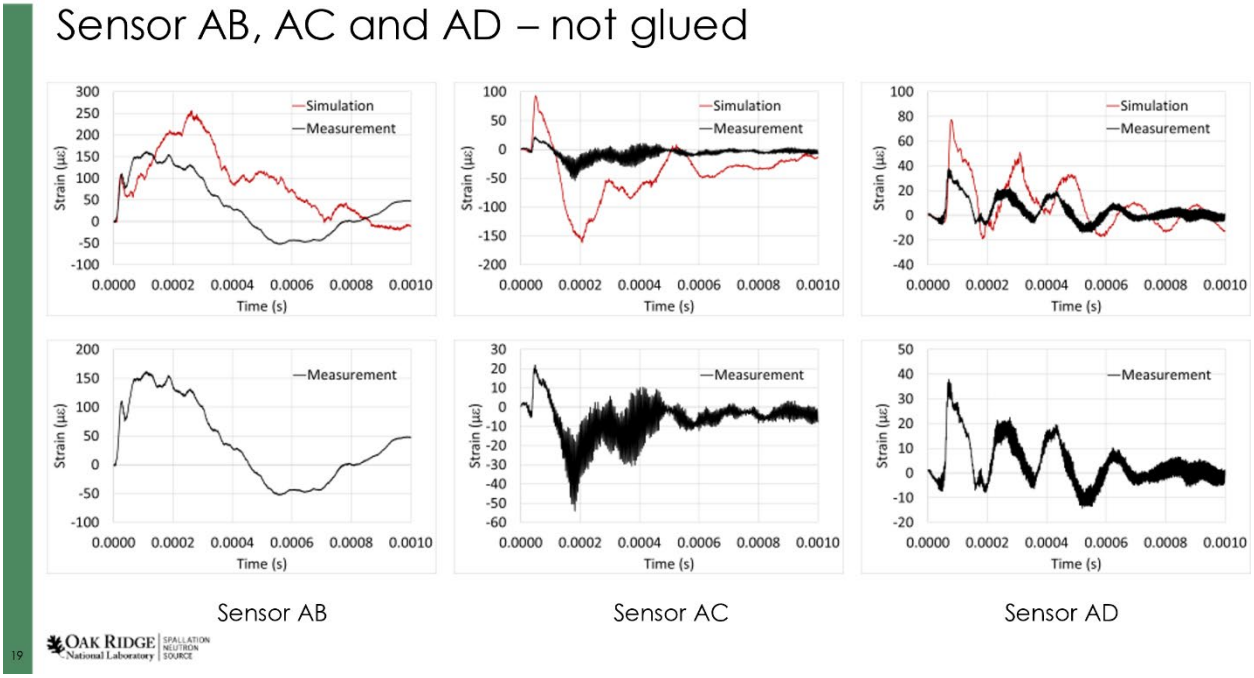

Figure 74: SNS Mercury Target 30 comparisons of partially bonded strain sensors against FEA simulations. The partially bonded sensors appear to measure the strain signal but at a reduced amplitude. CREDIT: Jiang Hao.

5.3.1.3 Microwave Instabilities and Errors

Beam shots #54-65 were found to be the sources of the largest disagreements between experiment and simulation. These shots correspond to the initial beam pulses after the 12 hour break for beam tuning beginning in the afternoon on August 27, 2022. Figure 65 shows that beam shots began on target B3 followed by B2 and then B1.

In informal conversations, LANSCE personnel mentioned microwave instabilities (harmonics of ~2.8MHz with 70 MHz as most intense harmonic) as a possible longitudinal source of the jagged edges in the beam current signal. The toroid measurements showed the abnormal beam behavior was worse at the beginning and then gradually improved. Figure 75 and Figure 76 compare one of these abnormal beam shots with a similar "normal" beam shot toward the end of the experiment. Figure 77 is a reproduction of Figure 72 using only shots #54-70. The beam pulses with the most suspected microwave instabilities correlate with the greatest underpredictions in simulations. In addition, these pulses correlate with the clear nonlinearity seen with the suspectedly debonded B3-K sensor. The beam current monitor's sampling rate was only 100MS/s so a 70 MHz signal would be recorded as an alias frequency ~30 MHz. However, the toroid also has a limited bandwidth of 30 MHz and attenuates the 70 MHz harmonic. It is thus unlikely for the microwave instability to clearly show up in the frequency spectrum, but we do see an increase in power at the higher frequencies, see Figure 76. We do not expect the jagged edges to affect the charge estimate as this is calculated by integrating over the beam pulse.

We also notice a noisier transverse profile in the image. The difference in noise in the image is, at least in part, due to a different exposure setting for the camera as shown by the lower pixel intensity counts. However, this should not affect the width calculation nor throw off the simulation. We notice a slightly different center position of the beam for these beam shots but, again, this is accounted for in the simulation.

Investigations are still ongoing to explain these particular beam pulses. Nevertheless, these pulses still fall within the previously defined error bands.

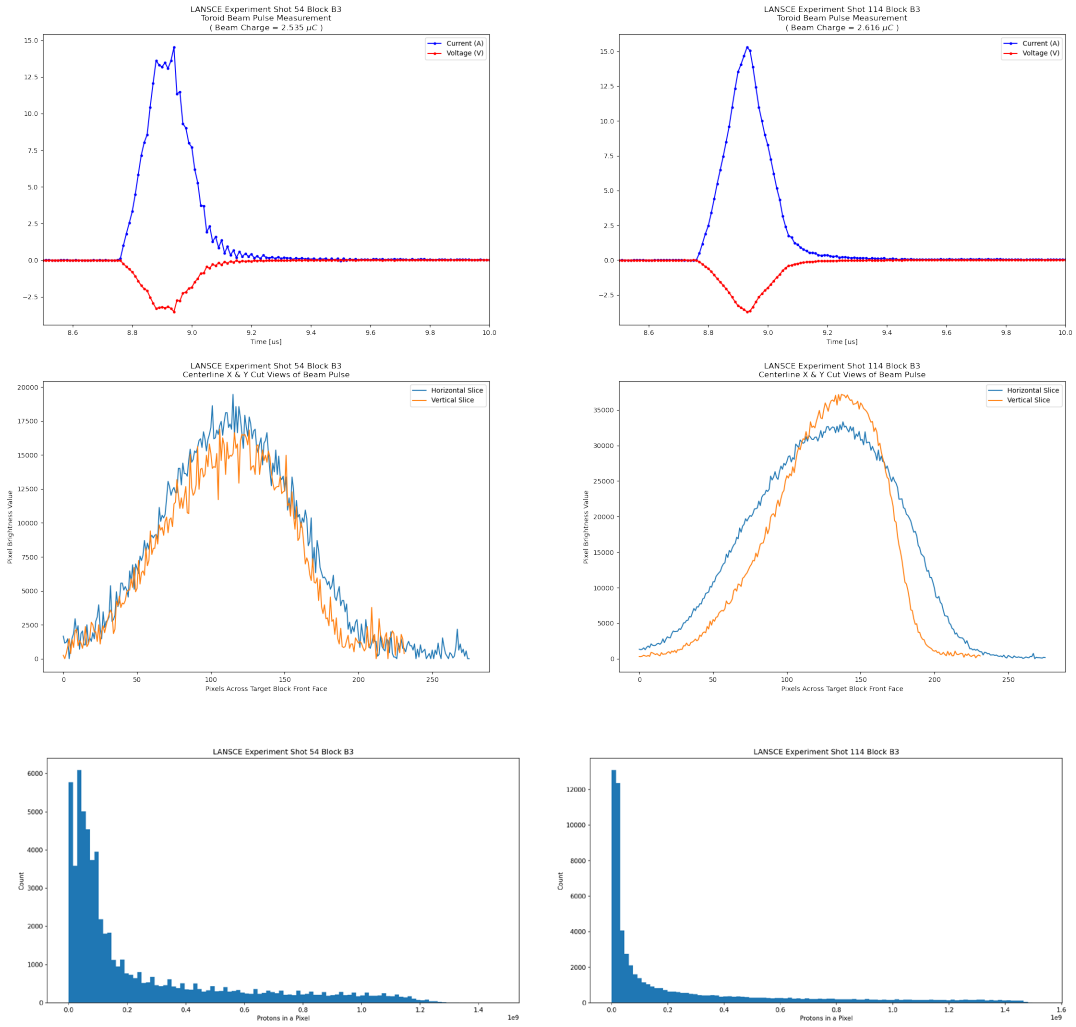

Figure 75: Comparisons between suspected abnormal (shot #54 block B3) and normal (shot #114 block B3) beam pulses of similar total charge.

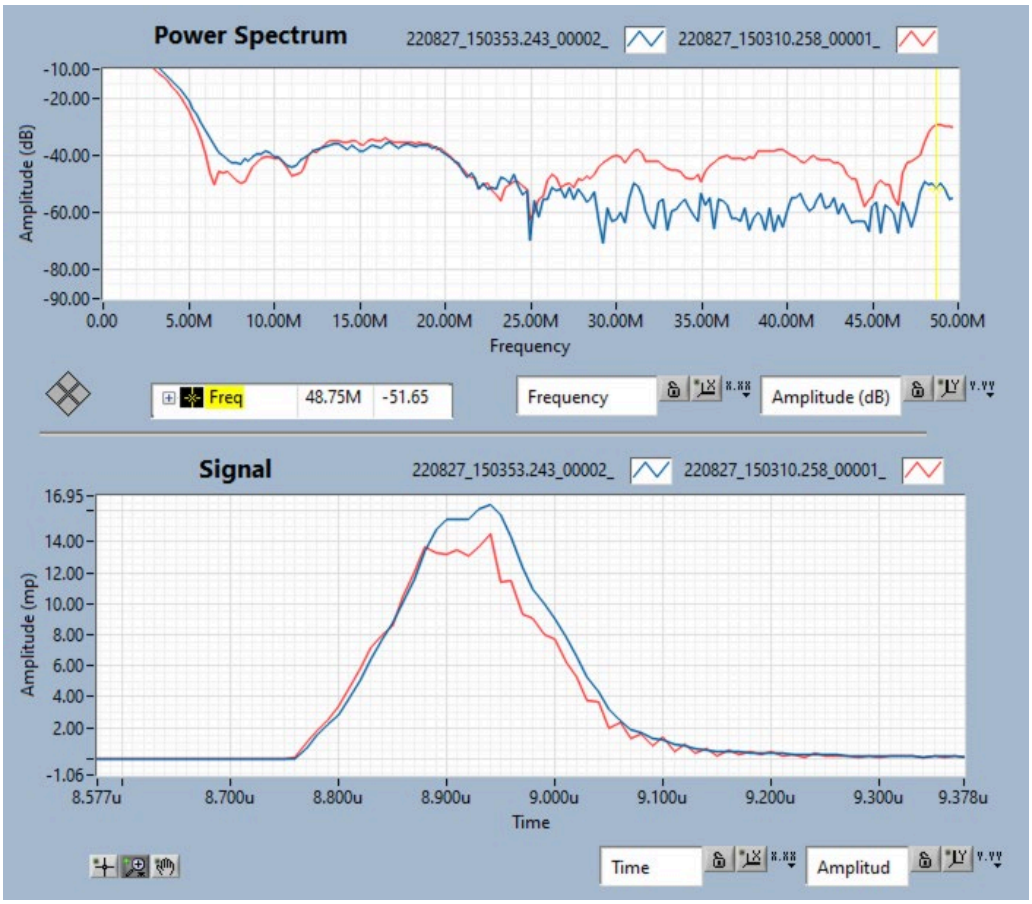

Figure 76: Toroid beam current measurements between abnormal and "normal" beam pulses. The abnormal pulse shows more higher frequencies and a flatter peak.

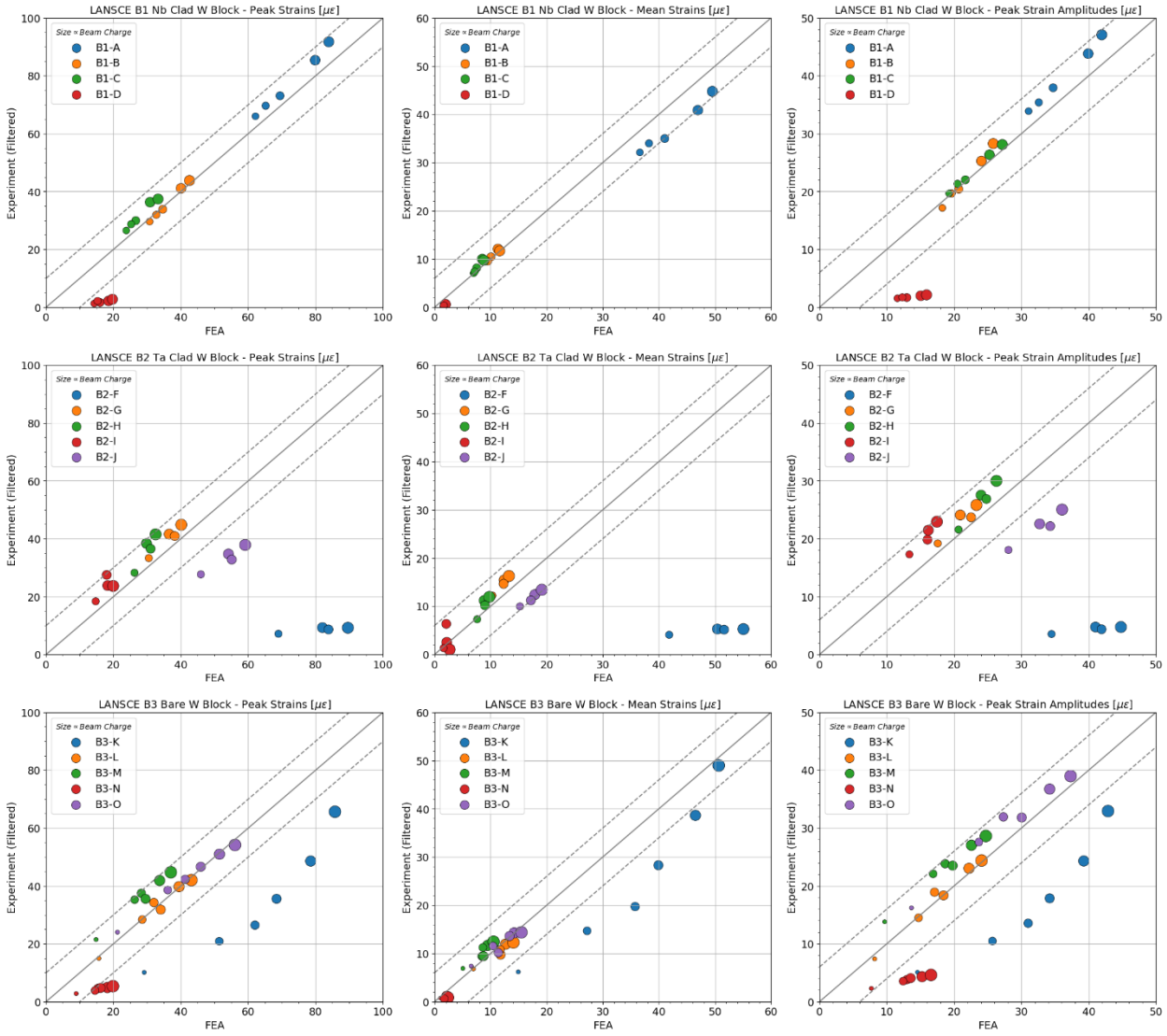

Figure 77: Comparisons between experimental strain measurements and FEA simulations for beam shots #54-70 which have suspected microwave instabilities.

5.3.1.4 Time of Peak Strain Occurrence

The time at which peak strain occurs is another useful diagnostic tool to compare the experimental measurement and simulations predictions. As previously shown in pre-experiment simulations, the FEA simulations include a small amount of default numerical damping. The time of peak strain occurrence always occurs at the beginning of the beam pulse. In contrast, Figure 78 shows significant scatter in the time of peak strain occurrence for strain measurements (including the 200 [kHz] low-pass filter). Sensors D, E, F, J, K, and N have already been identified as having connection or bonding issues. Aside from these, sensors A, B, C, H, and I experience discrepancies in peak strain occurrence.

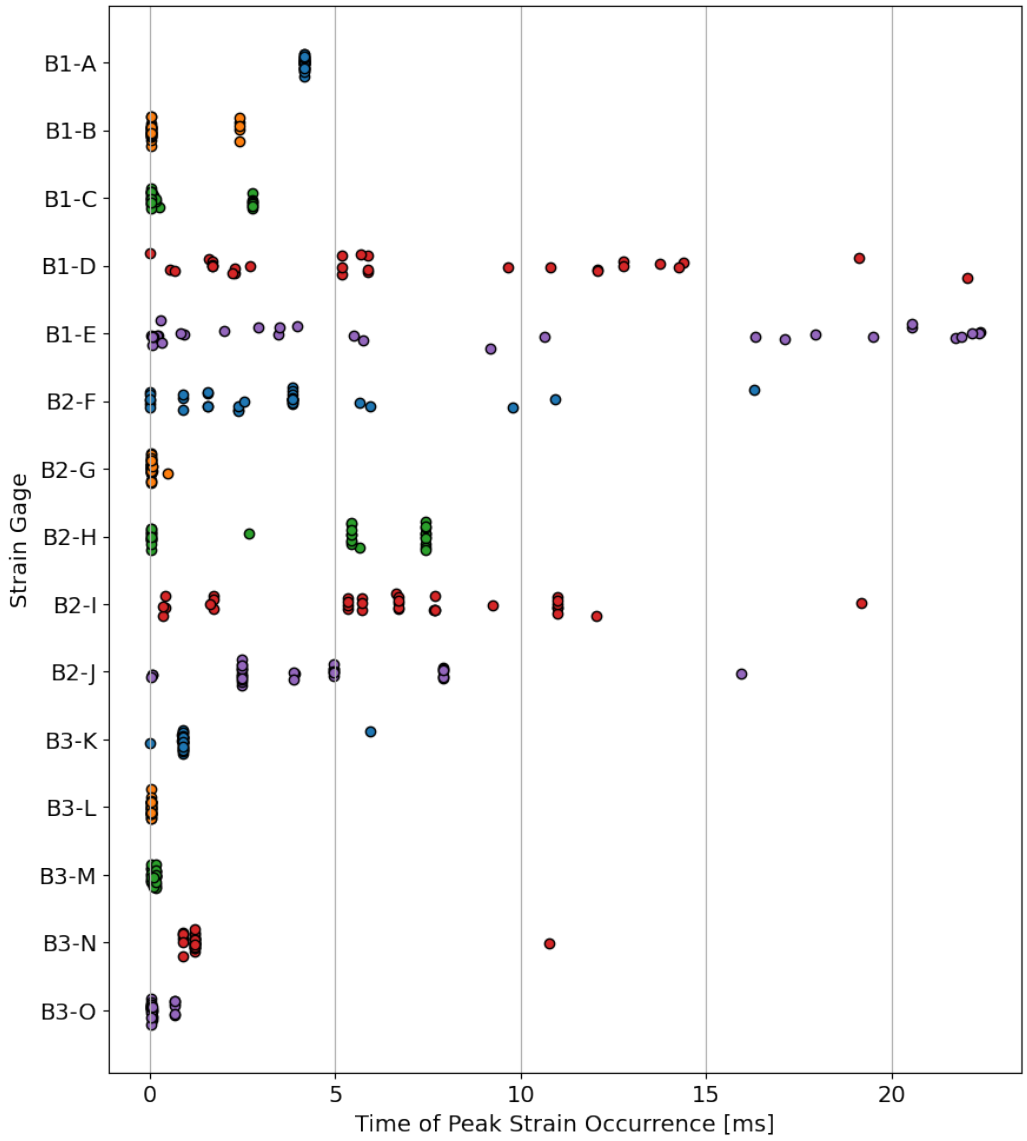

Figure 78: Time of peak strain occurrence for experimental measurements (and after application of a 200 [kHz] low-pass filter). Each data marker represents a beam pulse. The vertical scatter is random and only for the purpose of distinguishing beam shots.

Sensors H and I appear to have a (relatively) large noise level around 400-500 Hz with amplitude ±1 to ±2 [με]. It is possible that this noise, combined with the signal, causes the later and more random shifts in peak strain occurrence. Figure 79 and Figure 80 show examples.

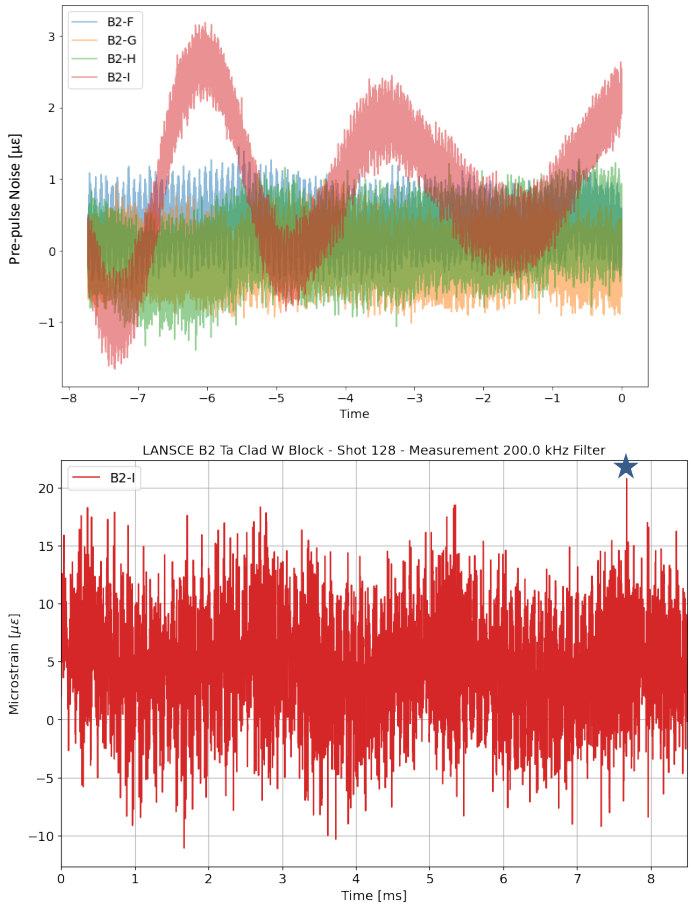

Figure 79: Comparison of pre-pulse noise with post-pulse strain response for sensor B2-I. The noise level on this channel could be high enough to cause the late occurrence in peak strain.

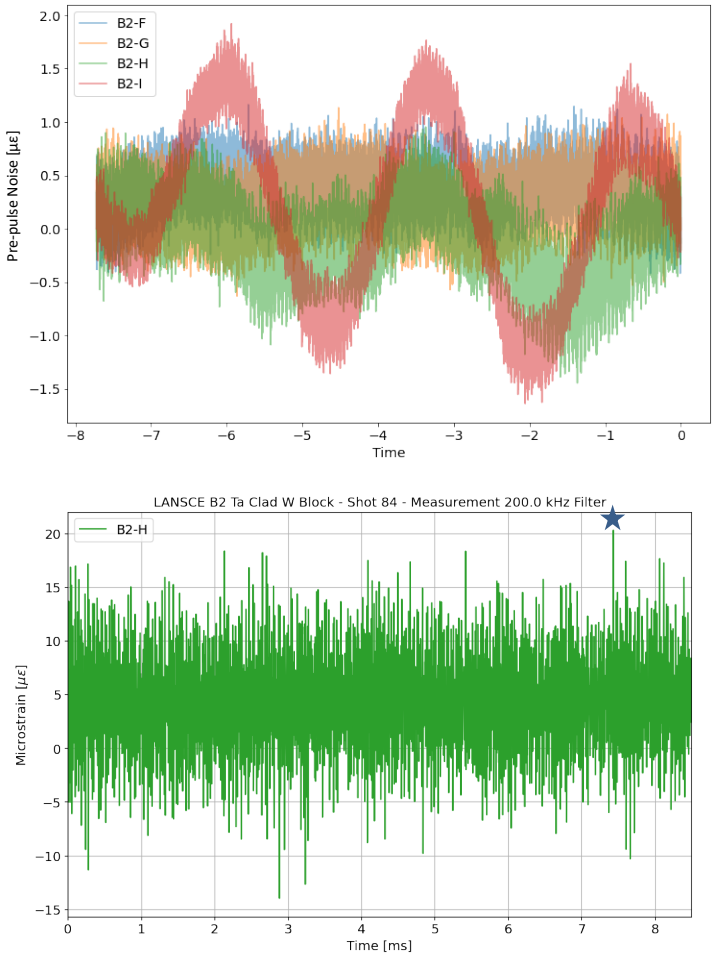

Figure 80: Comparison of pre-pulse noise with post-pulse strain response for sensor B2-H. The noise level on this channel could be high enough to cause the late occurrence in peak strain.

Strain sensors A, B, and C on block B1 experience peak strains at later times. Table 10 lists the times at which peak strain occurs for these sensors and Figure 81 shows strain responses for an example beam pulse. Interestingly, sensor A experiences a clear and repeatable peak strain at 4.17 [ms] for every single pulse. At this point, no explanation is available.

Table 10: Time at which peak strain occurs for sensors A, B, and C on block B1.

	Peak Strain Time [ms]		
Shot Number	*B1-A*	*B1-B*	*B1-C*
13	*4.16791*	*0.0339*	*0.0343*
14	*4.16811*	*0.0339*	*0.0343*
15	*4.16811*	*0.0338*	*0.0342*
16	*4.16841*	*0.034*	*0.0344*
18	*4.16811*	*0.0337*	*0.0341*
34	*4.16851*	*0.0341*	*0.0345*
35	*4.16811*	*0.0336*	*0.034*
36	*4.16811*	*0.0336*	*0.1014*
37	*4.16881*	*0.0341*	*0.0344*
38	*4.16831*	*0.0335*	*0.0338*
39	*4.16851*	*0.0337*	*0.034*
40	*4.16871*	*0.0338*	*0.1016*
41	*4.16871*	*0.0338*	*0.0341*
43	*4.16911*	*0.0339*	*0.0343*
66	*4.16951*	*0.0359*	*2.75341*
67	*4.16981*	*0.0361*	*2.75381*
68	*4.17051*	*0.0363*	*2.75421*
69	*4.17031*	*0.036*	*2.75401*
70	*4.17021*	*0.0359*	*2.75381*
94	*4.17111*	*2.39901*	*2.75501*
95	*4.17141*	*2.39921*	*2.75511*
96	*4.17141*	*2.39901*	*2.75501*
97	*4.17121*	*2.39881*	*0.269801*
98	*4.17151*	*2.39891*	*0.1495*
99	*4.16991*	*0.0351*	*0.1478*
100	*4.17011*	*0.035*	*0.0352*
101	*4.17001*	*0.0351*	*0.0353*
102	*4.16921*	*0.0345*	*0.0347*
103	*4.17031*	*0.0351*	*0.0352*
129	*4.16991*	*0.0344*	*0.0346*

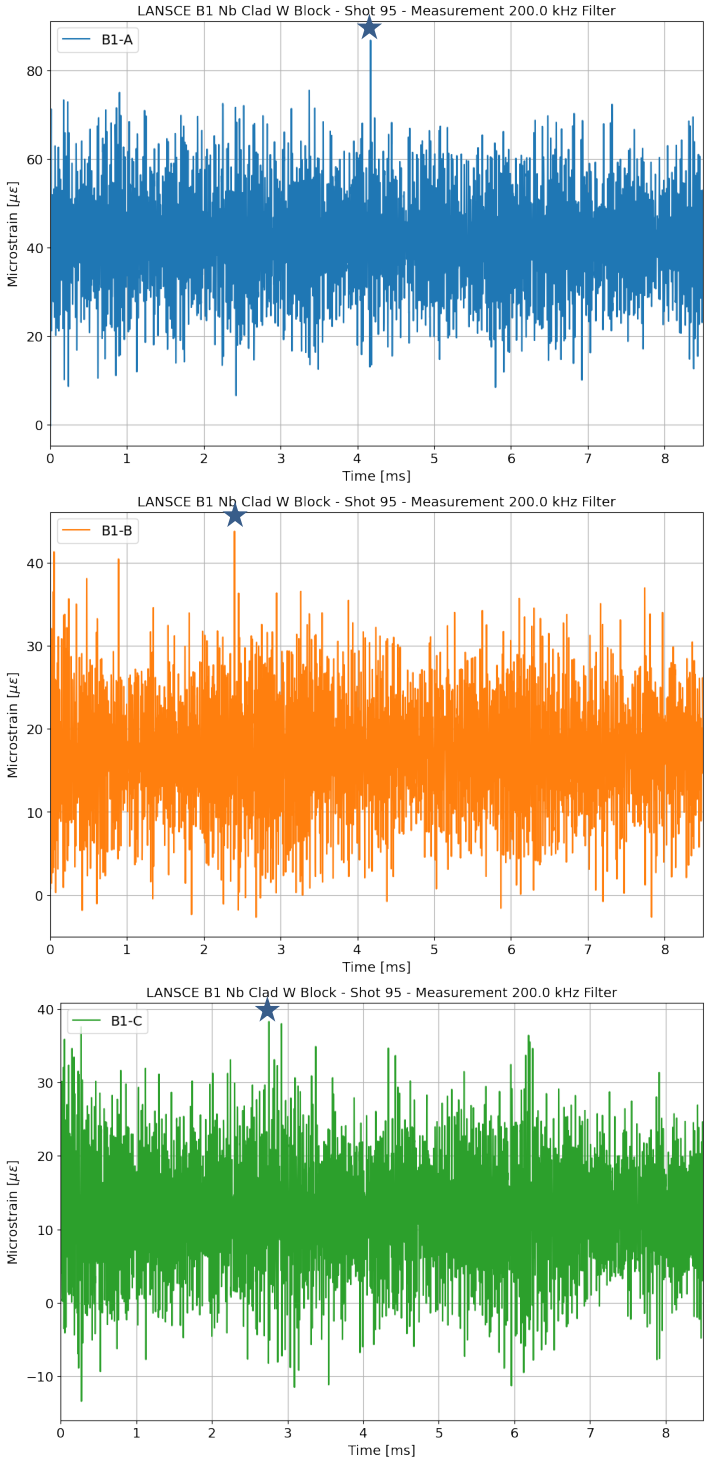

Figure 81: Strain waveforms for Shot #95 on block B1 showing late peak strain events. This is intermittent for sensors B and C but occurs clearly and consistently for sensor A.

5.3.2 Between Sample Beam Pulses Only

Toward the end of the experiment, the ORNL team made the decision to aim beam shots between blocks 1 and 2 (B1-2) and then between blocks 2 and 3 (B2-3). These may be analyzed in the future.

5.3.3 Phase and Damping

To explore the effects of phase and damping, sensors B1-B, B2-G, and B3-L are compared since they are consistently "good" across all 3 blocks. Figure 82, Figure 83, and Figure 84 compare these sensors against simulations. Observing the total time response, it is evident that the simulation underpredicts damping for sensor B3-L and overpredicts damping for sensors B1-B and B2-G. This is counterintuitive as it would suggest that more numerical damping is needed for the material in block B3 but that less is needed for the material in block B1 and B2. PIE activities should also confirm the cladding interface has been maintained.

A closer examination of the phase response for the bare tungsten block (B3) can also reveal information about material properties. The wave speed is proportional to the square root of the elastic modulus over density. At 0.4 [ms] the simulation clearly lags the experimental measurement. The complex nature of the frequency response makes it difficult to pinpoint the phase shift, but it appears to be in the range of 1.5 to 10 [μs]. If the elastic waves have propagated the same distance, then

$$\frac{L}{t} = \sqrt{\frac{E_{exp}}{\rho}};\ \frac{L}{t+\Delta t} = \sqrt{\frac{E_{fea}}{\rho}}$$

Assuming the density is constant yields a ratio for the elastic modulus according to the phase shift

$$\left(\frac{t}{t+\Delta t}\right)^2 = \frac{E_{fea}}{E_{exp}}$$

For a time duration of 0.4 [ms] and a phase shift of 1.5 to 10 [μs], the simulation modulus would be 1 to 5% below that of the material used in the experiment.

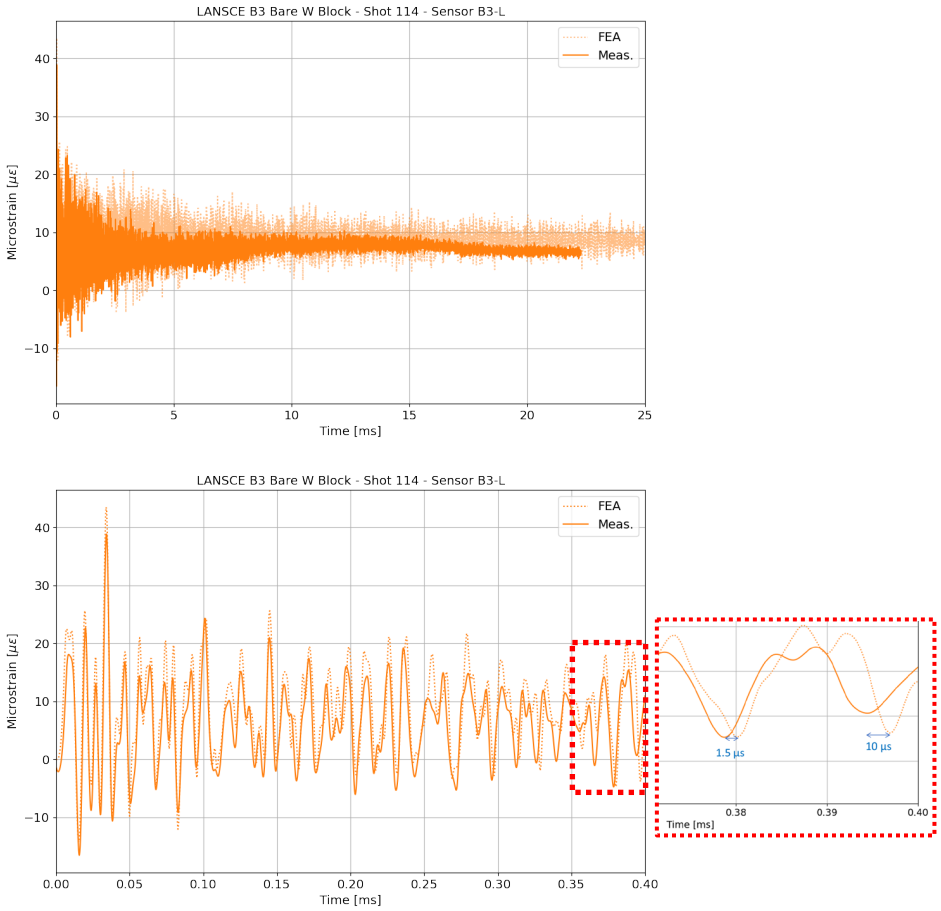

Figure 82: Block 3 phase and damping example.

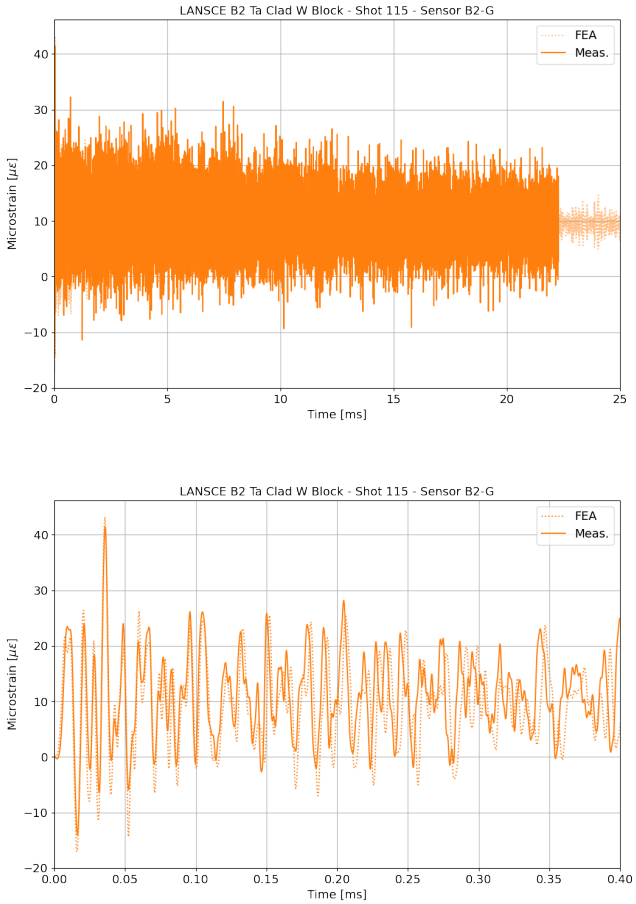

Figure 83: Block 2 phase and damping example.

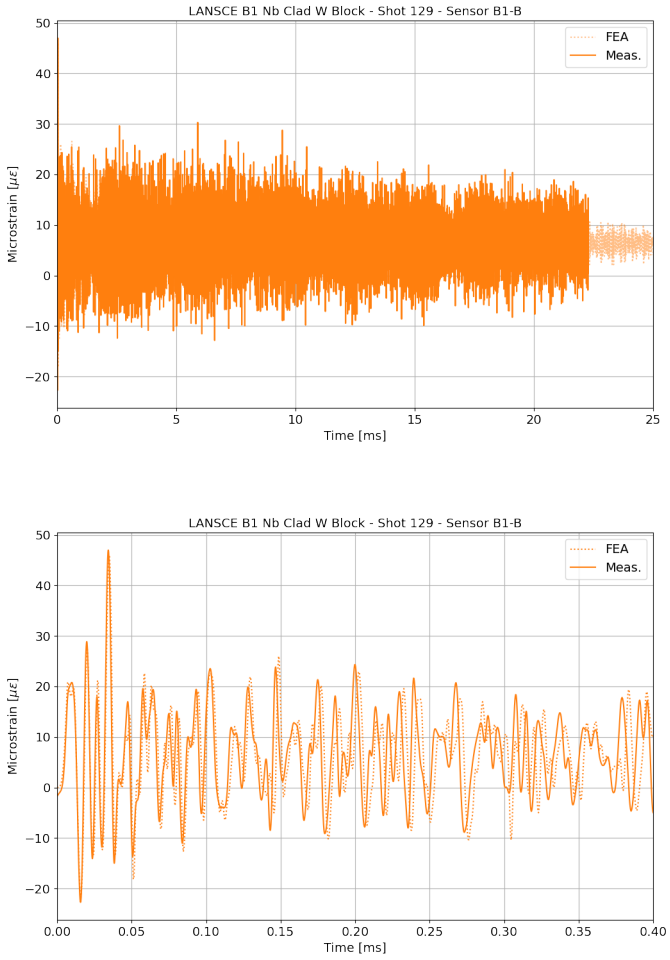

Figure 84: Block 1 phase and damping example.

6. DISCUSSION AND CONCLUSIONS

The strain response of the target block to thermal shock was measured at the LANSCE WNR Target 2 (blue room) facility on the outer surface of the blocks. Three target block samples were successfully manufactured and tested at the blue room: one Nb-clad tungsten, one Ta-clad tungsten, and one bare tungsten. Five strain sensors were installed on each target block at locations determined through simulation to contain peak strains on the four surfaces measured: front (facing beam), top, and sides. The fiber-optic strain measurement system designed by SNS was used to collect approximately 130 pulses of strain history data. Of the 15 total strain sensors, one was broken during experiment setup (B1-E) and five (B1-D, B2-F, B2-J, B3-K, B3-N) have suspected epoxy bond quality issues that affect the magnitude (but not the phase) of the strain waveform. These sensors also show a linear trend with beam charge, which is the expected response that has been documented in internal reporting by SNS. The remaining nine sensors provided the data for the relative error comparison with simulation predictions discussed below.

The experiment and the supporting simulations satisfied the following primary research goals for the STS target:

- Validation of analysis predictions of the dynamic strain response in STS test target blocks subject to high-energy pulsed proton beam impacts
- An assessment of the damping of the strain response between pulse impacts
- An assessment of the effect of cladding on the dynamic strain response

Each of these is discussed in more detail in following sections.

6.1 VALIDATION OF ANALYSIS PREDICTIONS

Pre-experiment simulations were used to determine that a nominal FEA mesh size of 1 mm and a time step output period of 0.6 μs was sufficient to achieve less than 5% relative (to the finest mesh) error for most sensor locations (ref. Figure 57). The error is balanced with computational time for each simulation, which is ~5 hours for the 1 mm mesh size.

The LANSCE accelerator and proton storage ring experienced operational difficulties before and during the experiment that resulted in wide variations in beam charge, shape, and location (ref. Figure 66 - Figure 70). A peak beam charge of ~5 μC was expected and planned for, however, only 3-3.1 μC was achieved for a few pulses and the mean was much lower at 2.14 μC with a standard deviation of 0.57 μC. Despite the limited and widely varying beam charge, the team was able to quantify the agreement between measured and predicted strains.

In general, excellent agreement occurs with data scatter falling within a constant ±10 [με] for peak strains and ±6 [με] for mean strains and strain amplitudes. The error does not appear to be proportional to strain magnitude or beam charge. This is critically important to be able to extrapolate the error to larger beam charges and strain magnitudes that are expected with the STS production target. For the largest beam charge pulses (~ 3 [μC]), the relative error approaches ±10% (ref. Figure 72). The STS target is expected to receive pulses with beam charges near 36 [μC]. If these trends extrapolate, then relative errors in strain predictions would be closer to ±1%.

A 1% increase in strain corresponds to a 1% increase in stress and a <1% (1-1/1.01) reduction in the factor of safety (FOS) for fatigue life predictions in the tungsten (according to the modified Goodman equation). For FOS values greater than 1, this reduction is an acceptable and nearly negligible amount. If the error was as much as 10% and the FOS reduced by ~9% (1-1/1.1) this would still be an acceptable amount for an FOS that is greater than or equal to 1.1. The FOS = 1.3 for the tungsten in the current “lasagna” target design, which has considerable margin to this error, i.e., FOS = (1.3/1.1) = 1.18.

6.2 DAMPING OF THE STRAIN RESPONSE

In general, damping (manifested as a reduction of strain amplitude over time) was under-predicted on the bare tungsten target block and over-predicted on the clad target blocks. The

artificial numerical damping introduced by the FEA software can affect this result, however, the differences were larger than expected. An observation from survey and alignment was that "the cladding process resulted in edges that were not square" (ref. section 3.2). Furthermore, the blocks were separated by 2 mm diameter pins placed in between the blocks and taped to the inside facing surfaces (to prevent contact from horizontal sliding motion over repeated beam pulses). This resulted in the blocks having more than the minimum 3-2-1 contact points for constraining rigid body motion.

It was difficult to photograph but could be visually observed that the bottom of block B2 (Ta-clad W) was not resting flat on the three vertical supports on the bottom surface. It is likely that block B1 (Nb-clad W) also was not supported as intended and this led to the reduced structural damping from contact with the fixture. This may explain the over-prediction of damping on the clad-target blocks. The bare tungsten block (B3) had flat surfaces and square edges that allowed for proper contact with the fixture constraints. This may explain the under-prediction of damping for this block because the fixture constraints were not included in the simulation predictions.

Regardless of the cause for the over/under-prediction of the damping, the critically important factor is that it did not seem to affect the ability to capture the peak strain amplitude and mean strain that control the fatigue life predictions. Figure 78 shows that there was significant variation in the time at which the peak strain occurred for different sensors, and this could be related to the variation in structural damping from the fixture constraints. However, there are confounding effects because the most widely varying peak strain times seem to occur for the sensors identified to have a bonding quality problem (B1-D, B2-F, B2-J, B3-K, B3-N). Of the remaining sensors, the variation is significantly less, although it does still occur later than predicted for sensors B1-A, B1-B, B1-C, B2-H, and B2-I. Interestingly, these are all sensors from the clad target blocks, which supports the hypothesis that the lack of or indefinable contact with the fixture may have led to less damping than expected and affects the time of peak strain occurrence.

6.3 EFFECT OF CLADDING ON THE STRAIN RESPONSE

The accuracy of the strain predictions described above was consistent across the bare tungsten, Ta-clad and Nb-clad target blocks, demonstrating that the FEA was as accurate for the two-material target block as it was for the pure tungsten target block. The FEA assumes a perfect bond between the cladding and the tungsten, which is modeled via a continuous mesh (shared nodes) across the material interface boundary. The manufacturing of the clad target blocks is intended to create a diffusion bond between the tantalum or niobium and tungsten. As mentioned in Section 2, the ultrasonic inspection cannot detect a difference between a tight mechanical bond with a small (on the order of 10 μm) gap and a true diffusion bond. The fact that the comparison of measured and predicted strains are quite close indicates that the cladding is tightly bound to the tungsten. Post-irradiation examination (PIE) of the bonding through sectioning and microscopic evaluation could support or refute this. PIE could also investigate

whether there is a good cladding bond beneath the sensors with suspected poor epoxy bond quality—confirming the latter is the reason for low strain magnitude responses in those sensors.

7. FUTURE WORK

The following is a list of recommendations for future work, if needed:

- Analyze laser doppler vibrometer (LDV) data:
    - An LDV was used to measure the displacement (vibration) response normal to the outer side surface of the bare tungsten block (near strain sensor B3-N). This was meant to be complementary to the strain sensor data, however, the age of the measurement system and the team's lack of experience with it led to difficulties with data sampling at a high enough rate to capture the very high frequency response of the solid target blocks. Historically, the system had been used with stainless steel vessels containing liquid mercury where the main frequency response is significantly lower than these solid target blocks. Therefore, it was decided that this data may prove to be of minimal use and was given a lower priority to analyze.
- Analyze pulses between blocks:
    - Early in the target design it was considered to receive pulses asynchronously with the target wheel rotation to more uniformly spread the effects of radiation induced damage in the materials. Therefore, the pulse plan originally called for receiving pulses between the target block samples, however, this was eliminated from the plan prior to the experiment. The design team had decided that the production target will receive pulses on the center of the target blocks and in sync with the target wheel rotation. As mentioned previously, due to the wide variation in beam charge and issues with the accelerator at LANSCE, the original pulse plan was discarded. Seeking alternatives to vary the load on the strain sensors more widely, the experiment team decided to receive beam pulses centered between the target blocks. To date, these have not been analyzed because they were considered much lower priority, and the pulses on block centers were sufficient for the validation of the FEA.
- PIE (post-irradiation examination):
    - To confirm the suspicion of poor-quality epoxy bonding of some of the sensors, it is proposed to photograph and measure the location and area of all the sensor epoxy, followed by a shear test to measure the force required to remove the epoxy from the surface of the target blocks. The sheared area of the epoxy would then be measured, and a calculated shear stress required to remove the epoxy could be compared between the "good" and "bad" sensor bonds.
    - Sectioning of the blocks at the strain sensor locations could confirm the cladding bond quality and compare between the "good" and "bad" sensor locations. In combination with the epoxy shear test above, this would likely provide the insight necessary to confirm or refute the hypothesis that the poor-quality epoxy bonding was the sole cause for the low magnitude strain response at some of the sensors.
- Sensitivity studies for vertical sensor placement: sensors that were broken during installation and re-installed may have been vertically shifted from original positions—enough to cause a portion of the error in the comparisons.

REFERENCES

[1] W.F. Sommer, S.A. Maloy, M.R. Louthan, G.J. Willcutt, P.D. Ferguson, M.R. James, Performance of a Clad Tungsten Rod Spallation Neutron Source Target, Nuclear Technology, 151 (2017) 303-313.
[2] A.T. Nelson, J.A. O'Toole, R.A. Valicenti, S.A. Maloy, Fabrication of a tantalum-clad tungsten target for LANSCE, Journal of Nuclear Materials, 431 (2012) 172-184.
[3] D. Wilcox, P. Loveridge, T. Davenne, L. Jones, D. Jenkins, Stress levels and failure modes of tantalum-clad tungsten targets at ISIS, Journal of Nuclear Materials, 506 (2018) 76-82.
[4] J. Busom Descarrega, M. Calviani, T. Hutsch, E. López Sola, A.T. Pérez Fontenla, A. Perillo Marcone, S. Sgobba, T. Weißgärber, Application of hot isostatic pressing (HIP) technology to diffusion bond refractory metals for proton beam targets and absorbers at CERN, Material Design & Processing Communications, 2 (2019).
[5] E. Lopez Sola, M. Calviani, P. Avigni, M. Battistin, J. Busom Descarrega, J. Canhoto Espadanal, M.A. Fraser, S. Gilardoni, B. Goddard, D. Grenier, R. Jacobsson, K. Kershaw, M. Lamont, A. Perillo-Marcone, M. Pandey, B. Riffaud, S. Sgobba, V. Vlachoudis, L. Zuccalli, Design of a high power production target for the beam dump facility at CERN, Physical Review Accelerators and Beams, 22 (2019).
[6] E. Lopez Sola, M. Calviani, O. Aberle, C. Ahdida, P. Avigni, M. Battistin, L. Bianchi, S. Burger, J. Busom Descarrega, J. Canhoto Espadanal, E. Cano-Pleite, M. Casolino, M.A. Fraser, S. Gilardoni, S. Girod, J.L. Grenard, D. Grenier, M. Guinchard, C. Hessler, R. Jacobsson, M. Lamont, A. Ortega Rolo, M. Pandey, A. Perillo-Marcone, B. Riffaud, V. Vlachoudis, L. Zuccalli, Beam impact tests of a prototype target for the beam dump facility at CERN: Experimental setup and preliminary analysis of the online results, Physical Review Accelerators and Beams, 22 (2019).
[7] A. Dey, L. Jones, Strategies to improve ISIS TS2 target life, Journal of Nuclear Materials, 506 (2018) 63-70.
[8] W. Blokland, Y. Liu, B. Riemer, M. Wendel, D. Winder, Strain and temperature measurements from the SNS mercury target vessel during high intensity beam pulses, 8th Int. Particle Accelerator Conf.(IPAC'17), Copenhagen, Denmark, 14â 19 May, 2017, JACOW, Geneva, Switzerland, 2017, pp. 1230-1233.
[9] Y. Liu, W. Blokland, C. Long, S. Murray III, B. Riemer, R. Sangrey, M. Wendel, D. Winder, Strain measurement in the recent SNS mercury target with gas injection, Journal of Physics: Conference Series, 2018.
[10] Y. Liu, C.D. Long, B. Qi, D.E. Winder, M.W. Wendel, Fast Dynamic Strain Measurement in the Spallation Mercury Target Using Fiber-Optic Sensors, Optical Sensors, Optical Society of America, 2019, pp. STh3A. 4.
[11] B. Qi, D.E. Winder, Y. Liu, Quadrature phase-shifted optical demodulator for low-coherence fiber-optic Fabry-Perot interferometric sensors, Opt Express, 27 (2019) 7319-7329.
[12] M. Guinchard, A. Bertarelli, A. Catinaccio, L. Bianchi, O. Capatina, P. Ferracin, M. Cabon, Mechanical Strain Measurements Based on Fiber Bragg Grating Down to Cryogenic Temperature-R&D Study and Applications, 9th International Particle Accelerator Conference, 2018, pp. 2572-2574.
[13] K. Ammigan, S. Bidhar, P. Hurh, R. Zwaska, M. Butcher, M. Calviani, M. Guinchard, R. Losito, V. Kuksenko, S. Roberts, A. Atherton, G. Burton, O. Caretta, T. Davenne, C. Densham, M. Fitton, P. Loveridge, J. O'Dell, Thermal shock experiment of beryllium exposed to intense high energy proton beam pulses, Physical Review Accelerators and Beams, 22 (2019).
[14] M. Teshigawara, T. Wakui, T. Naoe, H. Kogawa, F. Maekawa, M. Futakawa, K. Kikuchi, Development of JSNS target vessel diagnosis system using laser Doppler method, Journal of Nuclear Materials, 398 (2010) 238-243.
[15] T. Wan, T. Naoe, M. Futakawa, In-situ structural integrity evaluation for high-power pulsed spallation neutron source – Effects of cavitation damage on structural vibration, Journal of Nuclear Materials, 468 (2016) 321-330.

[16] B.W. Riemer, M.W. Wendel, D.K. Felde, Cavitation damage experiments for mercury spallation targets at the LANSCE – WNR in 2008, Journal of Nuclear Materials, 398 (2010) 207-219.
[17] B.W. Riemer, J.R. Haines, J.D. Hunn, D.C. Lousteau, T.J. McManamy, C.C. Tsai, SNS target tests at the LANSCE-WNR in 2001 – Part I, Journal of Nuclear Materials, 318 (2003) 92-101.
[18] J.D. Hunn, B.W. Riemer, C.C. Tsai, SNS target tests at the LANSCE-WNR in 2001 – Part II, Journal of Nuclear Materials, 318 (2003) 102-108.
[19] Y. Liu, B. Qi, D.E. Winder, Faraday Michelson Interferometers for Signal Demodulation of Fiber-Optic Sensors, Journal of Lightwave Technology, 39 (2021) 2552-2558.
[20] Y. Liu, D.E. Winder, B. Qi, C.D. Long, W. Lu, Upgraded Fiber-Optic Sensor System for Dynamic Strain Measurement in Spallation Neutron Source, IEEE Sensors Journal, 21 (2021) 26772-26784.
[21] P. Janiszewski, Rainflow, 2021, pp. https://pypi.org/project/rainflow/.
[22] ASTM E1049-85(Reapproved 2017), Standard Practices for Cycle Counting in Fatigue Analysis, ASTM International, West Conshohocken, PA, 2017.
[23] C. Werner, e. al, MCNP User's Manual, Code Version 6.2, Los Alamos National Laboratory, 2017.
[24] M. Chadwick, e. al, ENDF/B-VII.1 Nuclear Data for Science and Technology: Cross Sections, Covariances, Fission Product Yields and Decay Data, 2011.
[25] K. Ghoos, I. Remec, Neutronics Analysis in Preparation of the Blue Room Experiment, Oak Ridge National Laboratory, 2022.
[26] Attila4MC 10.2 Overview of Core Functions, Silver Fir Software, Inc., Gig Harbor, WA, 2020.
[27] J.B. Tipton, Sierra/SolidMechanics for Target Pulse Analysis, S03010000-TRT10000-R00, 2021.
[28] F.N. Beckwith, K.N. Belcourt, G.J. de Frias, J. Koester, K.L. Manktelow, M.T. Merewether, S.T. Miller, M.D. Mosby, J.A. Plews, V.L. Porter, T.R. Shelton, J.D. Thomas, B.C. Treweek, M.R. Tupek, M.G. Veilleux, E.B. Wagman, Sierra/SolidMechanics 4.56 User's Guide, United States, 2020, pp. Medium: ED; Size: 958 p.

APPENDIX A. RECOMMENDATIONS AND LESSONS LEARNED

- Target Imaging System (TIS) recommendations:
    - Place the screen very close to the targets and use simple markers for the calibration.
    - Deposit the screen on targets, like the SNS water shroud; this requires a bonding layer that depends on the material (e.g., Zn for SS).
- TIS: If we use two screens instead of one: 1 fixed in front of the targets and 1 to the side for during beam setup by LANSCE then the pneumatic cylinder is not needed, and everything could be moved with the translation stage.
- TIS: COTS Panasonic camera (~$2k) was extremely useful as a general observation camera. This camera was mounted high in the room and outside of the plane of the beam.
- TIS: Better quality zoom lens for the non-rad hard camera as the optical quality and focusing not good enough or bring camera closer. The zoom lens for the rad-hard camera was good.
- Preparation: Accelerator physics discussions to determine what is possible, versus what has been done before. Discussions with operators should be included as well.
- Survey and Alignment (S&A): Use more robust tripods for heavier objects like S&A mirror.
- Fixture: Try to move sample to beam rather than the other way around; requires a minimum of 2D movement, if not 3D plus rotations.
- Fixture: Need a minimum of 2-axis positioning (H and V), but a hexapod would be ideal.
- Fixture: Better not to split up the design between labs, rather build everything from the "floor up" and transport there.
- Software: Further simplify software to enable more people to use the data-acquisition system. Must expose to the user at least the following parameters:
    - Timing of TIS and BCM
    - Exposure and gain of camera (vendor of radhard camera must fix GigE interface)
    - Autosave settings so changes in settings can be compared with data
    - Calibration of BCM
- Strain Sensors: Is there a gravity effect on sensor installation?
    - One observation from data analysis to date is that we seem to have more indications of poor sensor bonding (low strain magnitude, but good phase and linear with charge) on front/side face sensors than the top sensors.
- Strain Sensors: Consider using a different glue, e.g. optical glue, given that there is a much lower total radiation dose compared to the First Target and to get an optimized bonding of the sensors to the samples:
    - Test the new glue on the back of the mercury target to see if it survives.
- Strain Sensors: Optical processors 4 & 5 were having issues when we got back, we suspect shipping damage.
- Strain Sensors: The fiber routing's initial strain relief was insufficient:
    - More clearance on lifting bracket would have helped
    - More fiber braid protection: there was too much bare fiber
- Installation: Consider Walkie-talkies for better communication and a Wi-Fi router with a local network (if allowed).

- Installation: Diagnostics/Electrical technician (Syd) was extremely helpful for troubleshooting and solving issues with electronic/electromechanical equipment:
    - Translation stage
    - Beam stop control
    - MPS
- Installation: Too busy in the blue room during camera alignment time
    - Better scheduling of time for this part to keep others out of the way
    - Consider simplifying S&A tasks or even provide fixture alignment documentation before shipment (similar to first target imaging calibration procedure)
- Installation: Combined cable bundle was helpful for routing
    - An outside jacket would have been useful, but we did not have capability to do it at SNS
- LANSCE: More difficulty in steering beam vertically than horizontally (LANSCE dependent)
- LANSCE: Non-gaussian beam shape is assumed due to horizontal and vertical tunes in the PSR.
- LANSCE: Timing triggers
    - Was not extraction pulse, not synchronized with beam on target. It was timed with LINAC pulse, so every time they changed the length, we had to retime beam current monitor and imaging.
- LANSCE: Investigate performing experiments like this at SNS—ideal location is extraction dump.
- Additional observations from data analysis:
    - Sensor B2-I: We always use the third channel to normalize the signal, but for sensor B2-I the normalization was failing due to saturated attenuation. This may affect some aspect of accuracy, such as the fine structure of the first few pulses. When the pulse hits the target, radiation induced attenuation (RIA) occurs in the fiber for a few microseconds. This can reduce the reflection by a factor of 2 and the strain calculation algorithm doesn't know if it is gap or intensity change. Therefore, the third channel compensates for intensity change, but the third channel was always saturated for sensor B2-I.
    - Sensors B3-O and B3-N: Analysis revealed that the cables for these sensors must have been mislabeled or accidentally switched at the data acquisition cabinet.
    - The pulse on the Nb clad block showed significant RIA in the fibers on blocks 2 and 3, but when the beam hit the bare W block, we saw minimal RIA on blocks 1 and 2. This is likely due to the self-shielding capability of the different density materials near the surface of each block.
    - SNS applies strain sensors only to stainless steel (low neutronic interaction); the iron of the steel is closest in density to the Nb cladding. SNS also only applies sensors on a horizontal surface so that gravity does not have a significant effect on the flow and wetting of the epoxy on the surface like it can for a vertical surface. For the LANSCE test blocks, the epoxy was applied on both horizontal and vertical surfaces for efficiency. The sensor installation time is approximately 24 hours, and this would have been ~5 times longer if the block surfaces were required to be oriented horizontally (perpendicular to gravity) for all sensor installations.

APPENDIX B. ADDITIONAL DOCUMENTATION AND DATA LOCATIONS

- STS SharePoint site – general project folder:
  - 3_IN-BEAM_TARGET_BLOCK_PERFORMANCE (https://ornl.sharepoint.com/:f:/r/sites/sts/targetsystems/Shared%20Documents/S.03.02%20Target%20Assembly/999_R%26D/3_IN-BEAM_TARGET_BLOCK_PERFORMANCE?csf=1&web=1&e=LWiRhc)

- Teams Site:
  - https://teams.microsoft.com/l/team/19%3a3a5af49dcf9a4c73982b72524b7cfa06%40thread.tacv2/conversations?groupId=e2afc036-0a0e-4ee5-ba64-4f5995e0e2ad&tenantId=db3dbd43-4c4b-4544-9f8a-0553f9f5f25e

- Data Analysis:
  - https://ornl.sharepoint.com/:f:/r/sites/sts/targetsystems/Shared%20Documents/S.03.02%20Target%20Assembly/99_SANDBOX/TIPTON/9_R%26D/EXP%20-%20LANSCE%20IN-BEAM%20TEST?csf=1&web=1&e=RdCNET

APPENDIX C. DRAWINGS

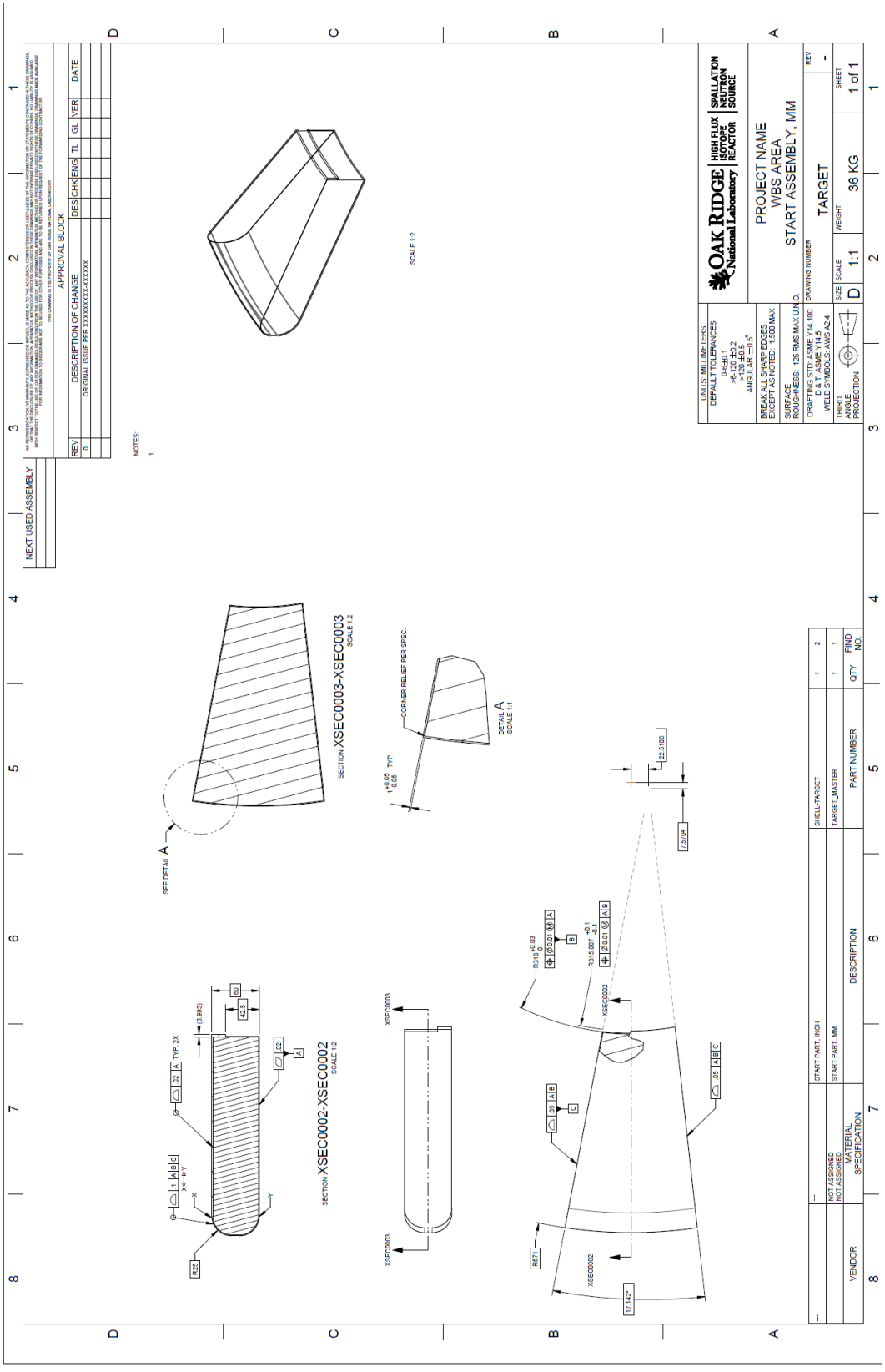

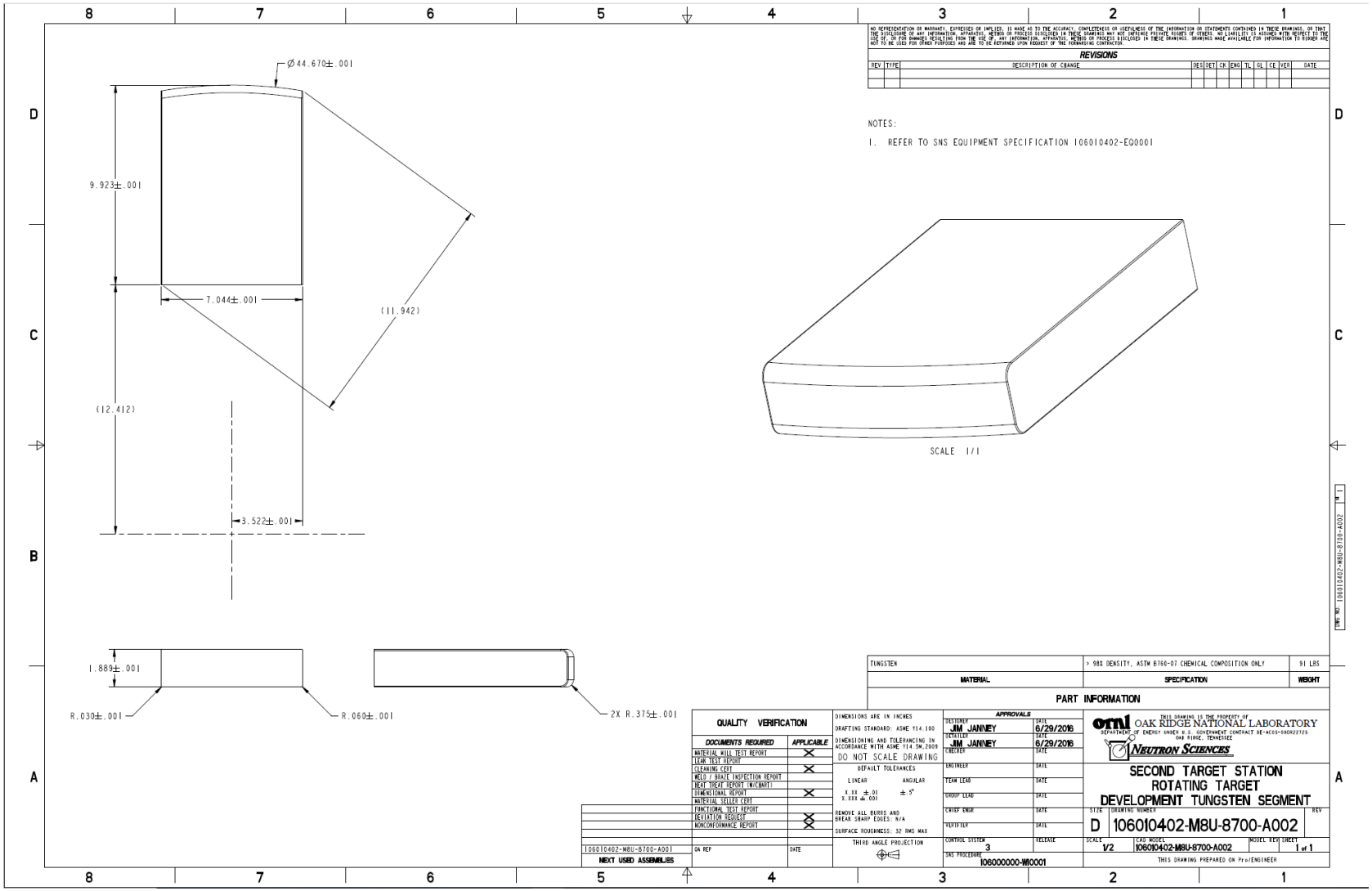

NO REPRESENTATION OR WARRANTY, EXPRESSED OR IMPLIED, IS MADE AS TO THE ACCURACY, COMPLETENESS OR USEFULNESS OF THE INFORMATION OR STATEMENTS CONTAINED IN THESE DRAWINGS, OR THAT THE DISCLOSURE OF ANY INFORMATION, APPARATUS, METHOD OR PROCESS DISCLOSED IN THESE DRAWINGS MAY NOT INFRINGE PRIVATE RIGHTS OF OTHERS. NO LIABILITY IS ASSUMED WITH RESPECT TO THE USE OF, OR FOR DAMAGES RESULTING FROM THE USE OF, ANY INFORMATION, APPARATUS, METHOD OR PROCESS DISCLOSED IN THESE DRAWINGS. DRAWINGS MADE AVAILABLE FOR INFORMATION TO BIDDER ARE NOT TO BE USED FOR OTHER PURPOSES AND ARE TO BE RETURNED UPON REQUEST OF THE AWARDING CONTRACTOR.

REVISIONS

REV	TYPE	DESCRIPTION OF CHANGE	DES	DET	CK	ENG	TL	GL	CE	VER	DATE

NOTES:

1. REFER TO SNS EQUIPMENT SPECIFICATION 106010402-E00001

MATERIAL	SPECIFICATION	WEIGHT
TUNGSTEN	> 98% DENSITY, ASTM B760-07 CHEMICAL COMPOSITION ONLY	91 LBS

PART INFORMATION

QUALITY VERIFICATION	
DOCUMENTS REQUIRED	APPLICABLE
MATERIAL MILL TEST REPORT	X
LEAK TEST REPORT	
CLEANING CERT	X
WELD / BRAZE INSPECTION REPORT	
HEAT TREAT REPORT (W/CHART)	
DIMENSIONAL REPORT	X
MATERIAL SELLER CERT	
FUNCTIONAL TEST REPORT	
DEVIATION REQUEST	X
NONCONFORMANCE REPORT	X
106010402-M8U-8700-A001	QA REP / DATE

NEXT USED ASSEMBLIES

DIMENSIONS ARE IN INCHES
DRAFTING STANDARD: ASME Y14.100
DIMENSIONING AND TOLERANCING IN ACCORDANCE WITH ASME Y14.5M,2009
DO NOT SCALE DRAWING
DEFAULT TOLERANCES
LINEAR: X.XX ±.01, X.XXX ±.001 — ANGULAR: ±.5°
REMOVE ALL BURRS AND BREAK SHARP EDGES: N/A
SURFACE ROUGHNESS: 32 RMS MAX
THIRD ANGLE PROJECTION

APPROVALS		
DESIGNER	JIM JANNEY	DATE 6/29/2016
DETAILED	JIM JANNEY	DATE 6/29/2016
CHECKER		DATE
ENGINEER		DATE
TEAM LEAD		DATE
GROUP LEAD		DATE
CHIEF ENGR		DATE
VERIFIER		DATE
CONTROL SYSTEM	3	RELEASE
SNS PROCEDURE	106000000-M10001	

NEUTRON SCIENCES

SECOND TARGET STATION
ROTATING TARGET
DEVELOPMENT TUNGSTEN SEGMENT

SIZE	DRAWING NUMBER	REV
D	106010402-M8U-8700-A002	

SCALE	CAD MODEL	MODEL REV	SHEET
1/2	106010402-M8U-8700-A002		1 of 1

THIS DRAWING PREPARED ON Pro/ENGINEER

DWG NO 106010402-M8U-8700-A002 REV 1

PEARSON™ CURRENT MONITOR MODEL 8586

Sensitivity	1.0 Volt/Ampere ±1%
Output resistance	50 Ohm
Maximum peak current	500 Amperes
Maximum rms current	20 Amperes
Droop rate	2 %/microsecond
Useable rise time	12 nanoseconds
Current time product	0.01 Ampere-second
Low frequency 3dB cut-off	3.2 kHz (approximate)
High frequency 3dB cut-off	30 MHz (approximate)
Output connector	Isolated ground BNC
Shielding	Double
Operating temperature	0 to 65 °C

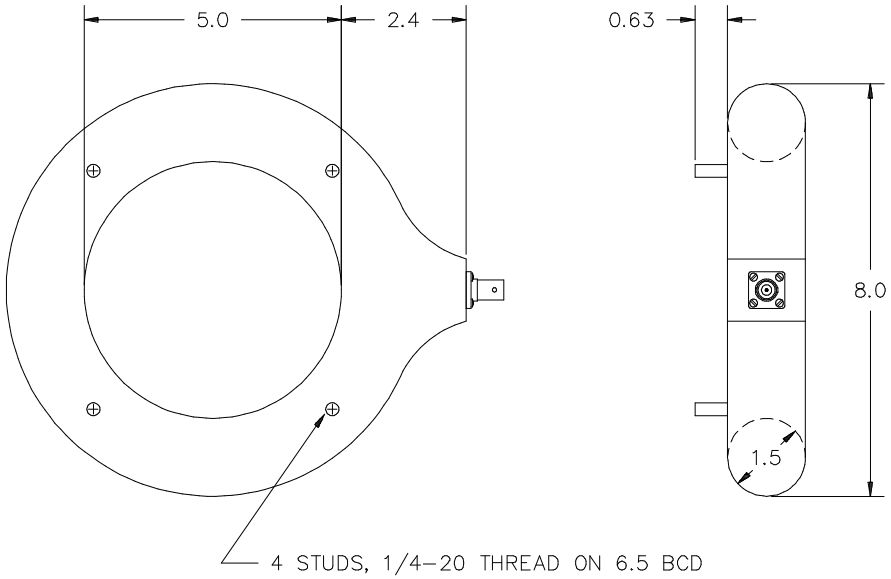

Pearson Electronics, Inc. • 4009 Transport Street • Palo Alto, CA 94303
Telephone 650-494-6444 • FAX 650-494-6716 • www.pearsonelectronics.com

	A					B				
	Goal A					Goal B				
	short	Long	shorter	short	Long	short	Long	short	Long	
Orbit Altitude, range	10	10	10	10	10	21	21	21	21	m
Swath-x	250	250	250	250	250	250	250	250	250	mm
Range Resolve Dist	0.4	0.4	0.6	0.6	0.6	0.7	0.7	1.0	1.0	mm
Range Sample Dist	0.6	0.3	0.7	0.6	0.3	0.6	0.2	0.6	0.2	mm
EPD	4.8	4.8	2.9	2.9	2.9	4.9	4.9	3.6	3.6	cm
F#	2.1	4.2	2.8	3.5	7.0	4.1	10.3	5.6	14.0	
EFL	100	200	80	100	200	200	500	200	500	mm
mag	100	50	125	100	50	105	42	105	42	
FOVx	3.4	1.7	4.3	3.4	1.7	2.0	0.8	2.0	0.8	degree
Pixel Pitch	5.5	5.5	5.5	5.5	5.5	5.8	5.8	5.8	5.8	um
Format-x	1088	1088	1088	1088	1088	1216	1216	1216	1216	pixels
Format max Diam	8	8	8	8	8	10	10	10	10	mm
Center Wavelength	0.7	0.7	0.7	0.7	0.7	0.7	0.7	0.7	0.7	um

Selections, parameter and performance comparisons

Notes:

- Range resolved distances are calculated by the conservative diffraction criterion 2.44 Lambda/D *range.

Customer Design / Selection Inputs:

Zoom A

- ~100mm-200mm zoom
- 1mm target resolution, short efl at 10m.
- As large an aperture as feasible for all zoom extremes for image contrast

Zoom B

- ~200mm-500mm min zoom range
- 1mm target resolution, short efl at 21m
- As large an aperture as feasible for all zoom extremes for image contrast